

ESR and ENDOR Investigations of
 Cr^{3+} Impurities in α , β and γ alums

by

Alexander G. Danilov

Submitted in partial fulfillment
of the requirements for the degree of
Doctor of Philosophy

Department of Physics,
Faculty of Pure and Applied Science
The University of Ottawa,
Ottawa, Canada.

1971

STATEMENT OF ORIGINALITY

The following is a list of work done in the course of this study and which, to the best of the author's knowledge, was not previously undertaken.

- 1) Electron spin resonance study of γ -type alum
- 2) Electron spin resonance study of a crystal of unknown structure
- 3) Electron spin resonance study of RbGa and CsGa alums in their hydrated and deuterated forms at both room temperature and 4.2°K.
- 4) First reported electron nuclear double resonance study of alum crystals.
- 5) First reported quadrupolar interaction of Cr(53) in alum crystals
- 6) First reported anisotropic hyperfine interaction in alum crystals
- 7) First reported detection of nuclear Zeeman interaction in alum crystals by the electron nuclear double resonance method.

ABSTRACT

Paramagnetic resonance of chromium impurities in three types of alum crystals was studied. The work can be divided into three main groups

- 1) the study of $^{52}\text{Cr}^{3+}$ ions doped in Rb and Cs gallium alums, including the deuterated forms of these alums, by employing the technique of electron spin resonance (ESR);
- 2) the study of $^{53}\text{Cr}^{3+}$ ions in the same alums by employing the technique of electron-nuclear double resonance (ENDOR);
- 3) ESR study of $^{52}\text{Cr}^{3+}$ ions doped in soda alum, $\text{NaAl}(\text{SO}_4)_2 \cdot 12\text{H}_2\text{O}$, and a crystal of unknown structure termed "pseudo soda alum".

All of the crystals were grown by slow evaporation of saturated solutions of the particular salts. The ESR measurements were made on the even isotope of chromium (Cr(52)), which has a natural abundance of 84%, while the ENDOR measurements were done on the odd isotope of chromium (Cr(53)), which was enriched to 98% in the crystals.

Four differently oriented but otherwise equivalent magnetic complexes of chromium were observed in the alums. The Z axes of the complexes were directed along the $\langle 111 \rangle$ crystal directions. The $^{52}\text{Cr}^{3+}$ fine structure of Rb and Cs alums is described by the following spin Hamiltonian at both room and liquid helium temperature.

$$H = g_{\text{II}} \beta H_z S_z + g_{\perp} \beta (H_x S_x + H_y S_y) + D(S_z^2 - 1/3S(S+1))$$

This Hamiltonian also applies to the soda alum which was studied at room temperature. Relative intensity line measurements at low temperature established the sign of the D parameter to be positive for Rb alum and

negative for the Cs and Na alums. In the pseudo soda alum two differently oriented but otherwise equivalent complexes of $^{52}\text{Cr}^{3+}$ were observed the spectrum is described by the spin Hamiltonian of rhombic symmetry:

$$H = \beta(g_z H_z S_z + g_y H_y S_y + g_x H_x S_x) + D(S_z^2 - 1/3S(S+1)) + E(S_x^2 - S_y^2).$$

The signs of the D and E parameters are negative.

The ENDOR study of $^{53}\text{Cr}^{3+}$ in the Rb and Cs alums at 4.2⁰K revealed a slightly anisotropic hyperfine structure. The quadrupolar interaction of the Cr(53) nucleus and the electric field gradient at the trivalent site in the alums was measured. The quadrupolar interaction in the Cs alums is an order of magnitude stronger than in the Rb alums. The nuclear Zeeman interaction in the alums was found to be isotropic. The measured ENDOR frequencies are described by the spin Hamiltonian of axial symmetry:

$$\begin{aligned} H = & g_{II} \beta S_z H_z + g_{\perp} \beta (S_x H_x + S_y H_y) + D(S_z^2 - 1/3S(S+1)) \\ & + A S_z I_z + B (S_x I_x + S_y I_y) \\ & + Q'(I_z^2 - 1/3 I(I+1)) - g'_{nII} \beta_n H_z I_z - g'_{n\perp} \beta_n (H_x I_x + H_y I_y). \end{aligned}$$

From the measured value of the parameters D and Q' and their absolute signs it was possible to deduce the quadrupole moment of Cr(53). In the Rb alums A>B, D>0 and in the Cs alums A<B, D<0. This reversal in the magnitudes of parameters A and B and the change of sign in the D parameter

has been related to a trigonal extension and trigonal compression of the octahedron of water molecules about the Cr^{3+} ion in the Rb and Cs alums respectively.

ACKNOWLEDGMENTS

The author wishes to thank Dr. A. Manoogian for suggestion of the problem and for guidance during the course of the research. His constant interest and encouragement is greatly appreciated. Thanks are due to Mr. B.W. Chan for his dexterous operation of the spectrometers and to Mr. N. Goodchild and his shop staff for construction of microwave cavities. The author is indebted to Mr. J.F. Rowland of the department of Energy, Mines and Resources, Ottawa, for precession camera X-Ray measurements. Financial assistance in the form of an Ontario Government Graduate Fellowship is gratefully acknowledged.

LIST OF ILLUSTRATIONS

Figure		Page
2.1	One quarter of the unit cell of Rb alum (α -type)	14
2.2	One quarter of the unit cell of Na alum (γ -type)	15
2.3	Stereographic projection onto the (111) plane of the {111} alum faces	19
2.4	Growth habit of pseudo soda alum	21
3.1	Splitting of the $^4F_{3/2}$ state of Cr^{3+} by the cubic and trigonal components of the crystal field.	27
3.2	Populations in a Double Resonance Experiment	55
4.1	X-band superheterodyne ESR spectrometer	61
4.2	X-band ENDOR spectrometer	63
4.3	TE_{014} mode X-band cavity	66
4.4	(a) Important directions and planes in the cubic system, (b) Crystal on sample holder, (c) Crystal directions.	68
4.5	(a) ENDOR X-band cavity, (b) sample holder and ENDOR coil support (c) Magnetic fields at sample	70

	page
5.1 Rb(H ₂ O) alum Z axis at room temperature, magnetic field is along the [111] crystal direction	76
5.2 Angular variation in the (111) plane, Rb(H ₂ O) alum	79
5.3 Angular variation in the (1 $\bar{1}$ 0) plane at room temperature, Rb(H ₂ O) alum.	81
5.4 ESR spectrum at room temperature when the magnetic field is along the [001] crystal direction, Rb(H ₂ O) alum	84
5.5 ESR spectrum at room temperature when the magnetic field is along the [110] direction, Rb(H ₂ O) alum	85
5.6 Energy level diagram of Cr ³⁺ in Rb(H ₂ O) at room temperature	86
5.7 Rb(H ₂ O) alum Z axis at 4.2 ⁰ K, magnetic field is along the [111] axis crystal direction identification at the lines is same as in Figure 5.1	87
5.8 Energy level diagram of Cr ³⁺ in Rb(H ₂ O) at 4.2 ⁰ K.	92
5.9 Soda alum Z axis at room temperature, magnetic field is along [111] crystal direction.	109
5.10 Angular variation in the (111) plane at room temperature, Soda alum.	110
5.11 Energy level diagram of Cr ³⁺ in the Soda alum at room temperature	112
5.12 Pseudo soda alum Z axis at room temperature	115
5.13 Angular variation in the ZY, YX and XZ planes in the pseudo soda alum at room temperature.	116
5.14 Stereographic projection of the crystal and magnetic axes in the pseudo soda alum at room temperature.	117

	page	
5.15	Energy level diagram of Cr^{3+} in the pseudo soda alum at room temperature	120
6.1	ESR spectrum of $^{53}\text{Cr}^{3+}$ ($\Delta M = -3/2 \rightarrow -1/2$) line in the $\text{Rb}(\text{H}_2\text{O})$ alum	122
6.2	ENDOR spectra of $^{53}\text{Cr}^{3+}$ of the $M_S = 3/2$ multiplet in the $\text{Rb}(\text{H}_2\text{O})$ alum at 4.2°K	127
6.3	Labeling scheme for ENDOR spectra	128
6.4	Hyperfine interactions of $^{53}\text{Cr}^{3+}$ in $\text{Rb}(\text{H}_2\text{O})$ alum at 4.2°K in MHz, (a) low field line, (b) high field line, 1.5A is about 78.2 MHz	135
6.5	$^{53}\text{Cr}^{3+}$ Z axis in $\text{Rb}(\text{D}_2\text{O})$ at 4.2°K , magnetic field is along crystal [111] direction.	137
6.6	ENDOR spectra of $^{53}\text{Cr}^{3+}$ of the $M_S = 3/2$ multiplet in the $\text{Rb}(\text{D}_2\text{O})$ alum at 4.2°K . Identification of the lines is same as in Figure 6.2	139
6.7	ENDOR spectra of $^{53}\text{Cr}^{3+}$ of the $M_S = -3/2$ multiplet in the $\text{Rb}(\text{D}_2\text{O})$ alum at 4.2°K . Identification of the lines is same as in Figure 6.2	140
6.8	Observation of nuclear Zeeman effect by the ENDOR technique	147
6.9	$^{53}\text{Cr}^{3+}$ Z axis in $\text{Cs}(\text{H}_2\text{O})$ at 4.2°K , magnetic field is along crystal [111] direction	149
6.10	ENDOR spectra of $^{53}\text{Cr}^{3+}$ of $M_S = -3/2$ set in $\text{Cs}(\text{D}_2\text{O})$ alum at 4.2°K	150

	page
6.11 ENDOR spectra of $^{53}\text{Cr}^{3+}$ of $M_S = 3/2$ set in $\text{Cs}(\text{D}_2\text{O})$ alum at 4.2°K .	151
6.12 Hyperfine interactions of $^{53}\text{Cr}^{3+}$ in $\text{Cs}(\text{D}_2\text{O})$ alum at 4.2°K in MHz, (a) low field line, (b) high field line, 1.5A is about 77.5 MHz.	158

LIST OF TABLES

Table		page
2.1	Mono and trivalent metal combinations which form alum salts.	10
2.2	Characteristics of Ions in Alums	11
3.1	Matrix of the fine structure spin Hamiltonian	39
3.2	Spin Hamiltonian matrix elements including the hyperfine structure for the orientation $H = H_z$.	41
3.3	Spin Hamiltonian matrix elements including the hyperfine structure when the magnetic field is perpendicular to the Z axis.	44
3.4	Transformation of D, E and g amongst the three principle axes.	49
5.1	ESR transition field values and spin Hamiltonian parameters for the $Rb(H_2O)$ alum at room temperature.	78
5.2	Field values for ESR transitions in (111) plane of the $Rb(H_2O)$ alum at room temperature	82
5.3	ESR transition field values and spin Hamiltonian parameters for the $Rb(H_2O)$ alum at $4.2^{\circ}K$.	88
5.4	Field values for ESR transitions in (111) plane of the $Rb(H_2O)$ alum at $4.2^{\circ}K$.	90
5.5	ESR transition field values and spin Hamiltonian parameters for the $Rb(D_2O)$ alum at room temperature	94

	page
5.6	Field values for ESR transitions in (111) plane of the Rb(D ₂ O) alum at room temperature. 95
5.7	ESR transition field values and spin Hamiltonian parameters for the Rb(D ₂ O) alum at 4.2 ⁰ K. 97
5.8	ESR transition field values and spin Hamiltonian parameters for the Cs(H ₂ O) alum at room temperature. 99
5.9	Field values for ESR transitions in (111) plane of the Cs(H ₂ O) alum at room temperature. 100
5.10	ESR transition field values and spin Hamiltonian parameters for the Cs(H ₂ O) alum at 4.2 ⁰ K 102
5.11	Field values for ESR transitions in (111) plane of the Cs(H ₂ O) alum at 4.2 ⁰ K 103
5.12	ESR transition field values and spin Hamiltonian parameters for the Cs(D ₂ O) alum at room temperature 105
5.13	ESR transition field values and spin Hamiltonian parameters for the Cs(D ₂ O) alum at 4.2 ⁰ K. 107
5.14	ESR transition field values and spin Hamiltonian parameters for the soda alum at room temperature 111
5.15	Spin Hamiltonian parameters for the Rb, Cs and Na alums. 114
5.16	ESR transition field values and spin Hamiltonian parameters for the pseudo-soda alum at room temperature. 119
6.1	Magnetic field values for points indicated in the spectrum of Figure 6.1 (b). 124

	Page
6.2	Cr(53) Experimental and calculated ENDOR frequencies in the Rb(H ₂ O) alum on the Z axis and in the perpendicular direction at 4.2 ⁰ K. 132
6.3	Spin Hamiltonian parameters and their absolute signs for the Cr ³⁺ ion in Rb(H ₂ O) alum at 4.2 ⁰ K. 133
6.4	Cr(53) Measured and calculated ENDOR frequencies in the Rb(D ₂ O) alum on Z axis and in the perpendicular direction at 4.2 ⁰ K. 141
6.5	Angular variation of ENDOR frequencies in the high field ESR line of the Rb(D ₂ O) alum in the (111) plane at 4.2 ⁰ K. 143
6.6	Angular variation of the ENDOR frequencies in the low field ESR line of the Rb(D ₂ O) alum in the (111) plane at 4.2 ⁰ K 144
6.7	Spin Hamiltonian parameters and their absolute signs for the Cr ⁺³ ion in Rb(D ₂ O) alum at 4.2 ⁰ K. 145
6.8	Cr(53) Measured and calculated ENDOR frequencies in Cs(H ₂ O) alum on Z axis and in the perpendicular direction at 4.2 ⁰ K 153
6.9	Cr(53) Measured and calculated ENDOR frequencies in Cs(D ₂ O) alum on Z axis and in the perpendicular direction at 4.2 ⁰ K 154
6.10	Angular variation of ENDOR frequencies in the low field ESR line of the Cs(D ₂ O) alum in the (111) plane at 4.2 ⁰ K. 155
6.11	Spin Hamiltonian parameters and their absolute signs for the Cr ⁺³ ion in the Cs(H ₂ O) and Cs(D ₂ O) alums at 4.2 ⁰ K 156
6.12	Direct, indirect and "e" ENDOR transitions on the Z axis of the Rb alums at 4.2 ⁰ K. 160

	Page
7.1 Nuclear quadrupole interactions, electric field gradients and nuclear quadrupole moment of Cr(53) in Rb and Cs alums	172
7.2 Comparison of the isotropic part of the hyperfine interaction of $^{53}\text{Cr}^{3+}$ in two environments.	179

TABLE OF CONTENTS

	<u>Page</u>
ABSTRACT	iv
ACKNOWLEDGEMENTS	vii
LIST OF ILLUSTRATIONS	viii
LIST OF TABLES	xii
CHAPTER I INTRODUCTION	1
CHAPTER II CRYSTALLOGRAPHY AND MATERIAL PREPARATION	9
A. Alum Crystallography	
B. Material Preparation	
C. Pseudo Soda Alum	
CHAPTER III THEORY	22
A. Introduction	22
B. Crystal Field Theory	25
C. Hyperfine Interaction	28
D. Quadrupole Interaction	31
E. Nuclear Zeeman Interaction	33
F. The Spin Hamiltonian	34
G. ESR Transitions and Energy Levels for Chromium in Alums	48
H. ESR Line Widths	52
J. Double Resonance	53

	<u>Page</u>
CHAPTER IV EQUIPMENT	58
A. Introduction	58
B. Commercial X-Band Spectrometer	58
C. X-Band Superheterodyne ESR and ENDOR Spectrometer	60
D. X-Band ESR Cavities	65
E. ENDOR Cavity	69
F. Dewar System for Liquid Helium Operation	69
G. Magnetic Field Measurement	71
CHAPTER V EXPERIMENTAL PROCEDURE AND RESULTS, ESR OF $^{52}\text{Cr}^{3+}$ IN THE ALUMS.	72
I Introduction	72
II The Rubidium Alum (α -type)	73
A The Rubidium Alum Grown From Solution in Ordinary Water	73
(i) Observations at room temperature	73
(ii) Observations at liquid helium temperature	83
B The Rubidium Alum Grown From Solution in Heavy Water	93
(i) Observations at room temperature	93
(ii) Observations at liquid helium temperature	96
III The Cesium Alum (β -type)	98
A The Cesium Alum Grown From Solution in Ordinary Water	98
(i) Observations at room temperature	98
(ii) Observations at liquid helium temperature	101

	<u>Page</u>
B The Cesium Alum Grown From Solution in Heavy Water	104
(i) Observations at room temperature	104
(ii) Observations at liquid helium temperature	106
IV The Soda Alum (γ -type)	108
V The Pseudo Soda Alum	113
CHAPTER VI EXPERIMENTAL PROCEDURE AND RESULTS, ENDOR OF $^{53}\text{Cr}^{3+}$ IN Rb and Cs ALUMS	121
I The Rubidium Alum	121
A Crystals Grown from Solution in Ordinary Water	121
B Crystals Grown from Solution in Heavy Water	136
II The Cesium Alum, Crystals Grown From Solution in Ordinary Water and Heavy Water	148
III The "e" ENDOR Transitions	159
CHAPTER VII DISCUSSION AND CONCLUSIONS	162
A ESR of Chromium in the Alums	162
B Nuclear Zeeman Interaction	165
C The Nuclear Quadrupole and Crystal Field Interactions	168
D Hyperfine Interaction	176
E Post Oral Discussion	181
APPENDIX	185
LIST OF REFERENCES	187
VITA AUCTORIS	191

CHAPTER I

INTRODUCTION

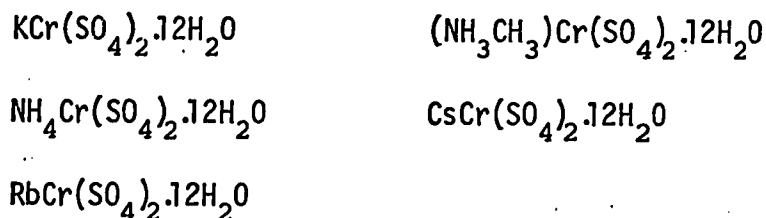
The alums consist of a large group of crystals which belong to the cubic system and possess the space group T_h^6 (Pa3) ¹. Slight differences in atomic arrangement enable three types of alum structures to be determined termed α , β and γ . In each case there are four formula units per unit cell, with the general formula for the sulfate alums being $M'M'''(SO_4)_2 \cdot 12H_2O$. In this formula M' and M''' are monovalent and trivalent cations respectively. Each trivalent ion has as its nearest neighbors six water molecules forming a trigonally distorted octahedron, with the distortion being along the $\langle 111 \rangle$ crystal direction.

In the X-ray crystallography work of Lipson ² it was suggested that the different types of alums were determined by the size of the monovalent ion: the γ class for small ions, the β class for large ions and the α class for those intermediate in size. With the exception of KCr alum, the investigations were confined to samples in which the trivalent ion was aluminum. In the X-ray crystallographic work of Ledsham and Steeple ³ on NaCr alum it was shown that the type of alum can depend on the particular combination of monovalent and trivalent ions present. This was concluded from the fact that NaAl alum is of the γ type while NaCr alum is α type. In the ESR study of VO^{2+} ions in RbAl alum and CsAl alum by Manoogian and MacKinnon ⁴ it was shown that the VO^{2+} ion can affect the class to which an alum belongs. In particular, under the influence of this impurity an α alum would appear as a β alum, and vice versa.

The X-ray work of Lipson and Beevers ¹ and Lipson ² showed that in the α type of alums the [111] axis of the octahedron of water molecules surrounding an aluminum atom coincides with the [111] crystal axis, but the cubic axes of the octahedron are displaced from the cubic axes of the crystal by a rotation of approximately 9.5° about the [111] direction. In the β type of alums the cubic axes of the octahedron are directed along the cubic axes of the crystal. The γ alums are said to differ from the α and β alums in that the sulfate groups of the γ alums are oriented oppositely along the crystal body diagonals to those of the α and β alums. The cubic axes of the octahedron in the γ alums are rotated about the [111] crystal direction by about 40° . The only known γ alum is soda alum, $\text{NaAl}(\text{SO}_4)_2 \cdot 12\text{H}_2\text{O}$.

The earliest ESR studies on alums were performed by Weiss et al ⁵ and by Whitmer et al ⁶. They investigated ammonium chrome alum and potassium chrome alum in concentrated and somewhat diluted form. The precision of their measurements was quite limited as they were hindered by the very wide absorption lines which were due to high concentration of chromium in their salts. This high concentration was necessary in order to produce strong absorption signals required by the relatively low sensitivity of the early spectrometers. Nevertheless, these workers were able to show that chromium is subject to a predominantly cubic electric field with a superimposed slight axial distortion. This distortion was found to be along the $\langle 111 \rangle$ directions. They obtained a g value for chromium in the ground state, of about 1.98. The zero field splitting (Kramer's doublet separation), was found to be about 0.14 cm^{-1} .

The first comprehensive attempt to study paramagnetic absorption in the alums was undertaken by Bagguley and Griffiths⁷, and by Bleaney⁸ who selected the following five salts for their investigation:



The salts in the first column belong to the α type, while those in the second column belong to the β type. Bagguley and Griffiths carried out their investigation at room temperature while Bleaney studied the same salts at low temperature, (down to 20°K). In these concentrated salts the absorption lines are quite wide and the spectrum is poorly resolved. In spite of this it was shown that at room temperature the chromium ions exist in four differently oriented, but otherwise equivalent, sites. It was also shown that the octahedra of water molecules surrounding the chromium exhibit an axial distortion. This distortion was found to be along the $\langle 111 \rangle$ directions. The amount of this distortion varied from 0.12 cm^{-1} to 0.165 cm^{-1} at room temperature for the five salts investigated. The work of Bleaney showed that chromium spectra underwent changes at low temperature. It was observed that the magnitude of the axial distortion changed in Rb, Cs and NH_3CH_3 alums. In NH_4 alum a crystallographic transition took place, while in K alum an additional chromium spectrum appeared. The zero field splittings associated with the two spectra are $.15$ and $.27 \text{ cm}^{-1}$. The chromic methyamine alum was redone by Baker⁹. He showed that the axial field changed to rhombic symmetry at about 160°K .

As representatives of the α and β types, RbGa and CsGa respectively, were selected. In order to reduce the problems associated with large linewidths encountered by the early investigators, chromium was introduced as an impurity and not as the main trivalent ion. Gallium was selected as the trivalent ion rather than aluminum because Ga³⁺ ionic radius of 0.62 Å is quite close to 0.64 Å the ionic radius of Cr³⁺; that of Al³⁺ being 0.50 Å. A duplicate set of alum crystals were grown from a heavy water solution. This was first proposed by Bleaney et al¹⁰, the idea being, that since deuterons have a smaller magnetic moment than the protons in the waters of hydration, the hyperfine interaction due to surrounding neighbours would be smaller and hence the absorption line widths are expected to diminish. In the above cited work this is found to be the case for diluted copper potassium sulphate, where a linewidth of about 6 gauss was reduced to about 2 gauss. Bleaney and Bowers¹¹ have assumed that this effect is valid for all deuterated salts. In the course of this work it was found that deuteration did not in any crystal reduce linewidths with respect to the hydrated crystals.

The information that one can hope to obtain by studying the ESR of chromium impurities in alums is limited by the following considerations. Eighty four per cent of naturally occurring chromium (Cr(52)) has no nuclear magnetic moment. Chromium (53), on the other hand, which is about 9% abundant, does have a magnetic moment, its nuclear spin being 3/2. Unfortunately, most chromium spectra at room and even at liquid helium temperature do not show a hyperfine structure. This is because the linewidth of the 84% abundant isotope even at low concentrations masks the low intensity Cr(53) spectrum. As a consequence of this fact hyperfine interactions due to chromium can not be studied readily. Even if one

attempts to circumvent this problem by growing crystal enriched in the Cr(53) isotope not very much is gained. The reason for this is that the relatively weak hyperfine interaction of Cr(53) and the various line broadening mechanisms result in only a partly resolved hyperfine spectrum.

In this case one is limited in the study of hyperfine interactions by not being able to detect small anisotropy, the nuclear quadrupole interaction or nuclear Zeeman interaction.

Because of such considerations the Rb and Cs alums enriched in the Cr(53) isotope have also been studied by the ENDOR method. No study of any alum by the ENDOR method has been reported. The enriched crystals were also studied in their deuterated form in this way. The ENDOR technique depends on measuring transitions between energy levels due to hyperfine interactions whereas the ESR technique measures transitions between energy levels due to Zeeman interaction. Using the ENDOR method one can study hyperfine interactions with increased accuracy; this increase being given roughly by the ratio of the Zeeman interaction to hyperfine interaction. In case of $^{53}\text{Cr}^{3+}$ at X-band this ratio is about 100.

The ENDOR method was first proposed¹² and developed by Feher¹³ and has been used successfully for over a decade to study paramagnetic centers having hyperfine interactions. Terhune et al¹⁴ have reported on ENDOR of $^{53}\text{Cr}^{3+}$ in Al_2O_3 . Terhune et al¹⁵ in subsequent work on $^{53}\text{Cr}^{3+}$ in Al_2O_3 have measured the hyperfine interaction, with what at that time, was greatest precision. They found the interaction to be isotropic. Also they were able to calculate the quadrupole moment for the Cr(53) nucleus after making some assumptions about the electric field gradient in the Al_2O_3 lattice.

It can be seen that the results obtained are varied. In the case of potassium alum, where an additional spectrum appears, no adequate explanation has been proposed. That all five salts investigated at room temperature have an axial crystal field distortion along the $\langle 111 \rangle$ directions, at the trivalent sites appears to be the only common feature. Although Bagguley and Griffith report no rhombic distortion at room temperature this possibility can not be excluded with certainty. The reason for this is the fact that all spectra at room temperature are quite poorly resolved. With poor resolution of spectral lines and with no detailed study of angular variation of the spectrum in the (111) plane one can not exclude the presence of a small rhombic term in the crystal field.

These early studies suggested that ESR spectra could not be related to an α , β , or γ type. This, of course, was inconclusive since only the alpha and beta types were investigated and no sign determinations of spin Hamiltonian parameters were made. The rather varied paramagnetic behaviour of the alums provides motivation for further study of these salts by ESR. For this purpose a representative of each of the three types of alums was selected for investigation. In case of the γ type the choice is quite simple since only one alum of this type is known, that being the soda alum, $\text{NaAl}(\text{SO}_4)_2 \cdot 12\text{H}_2\text{O}$. No ESR study of the γ alum has been reported. When growing the soda alum from solution often another crystal of unknown structure termed "pseudo soda alum" crystallizes. This crystal usually grows in thin flat elongated form, but short ones also grow. One can not often know by visual observation whether or not a given crystal is soda alum or pseudo soda alum. The ESR results allow an unambiguous identification.

The value which they obtained for the quadrupole moment of Cr(53) and their observation of isotropic hyperfine interaction was later strongly criticized by Lawrence and Lambe¹⁶. This is the only available determination of Cr(53) nuclear quadrupole moment. Woonton and Dyer¹⁷ have studied $^{53}\text{Cr}^{3+}$ in MgO. They measured a very weak quadrupolar interaction and could not deduce the quadrupole moment. The weakness of the interaction is presumably due to a very small electric field gradient at the chromium ion in the cubic lattice. Motivation for studying Cr(53) in the alums by the ENDOR method was threefold. Firstly, it was hoped that the high precision of the technique would yield some new information about the alums. Secondly, it was hoped to deduce the quadrupole moment of Cr(53). Thirdly, although a number of ESR observations of the Cr(53) hyperfine structure have been made* all but two^{17,18} have reported an isotropic interaction. This is thought to be due to the relatively low precision of ESR method in detecting small anisotropy in the chromium hyperfine interaction and that the reported observations are more the exception than the rule. In the course of this work the above objectives have been satisfied to a considerable extent. The parameters in the spin Hamiltonian of axial symmetry have been measured and their absolute signs determined. From this it was possible to calculate the quadrupole moment of Cr(53) to be - 0.039 barns, a value that agrees well with that obtained by Terhune et al. It was found that for the Rb alums the trigonal component of the crystalline electric field (D) is positive and that the hyperfine interaction is anisotropic (A>B). For the Cs alum it was found that D is negative and that B>A. This reversal of magnitudes of A and B and the sign of the D parameter is to be associated with trigonal extension or compression

* See Table 7.2

of the octahedron of the water molecules around the chromium ion.

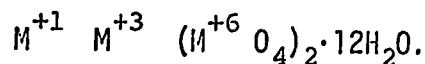
A tentative conclusion is that this extension and compression are related to the α and β type alums respectively.

CHAPTER II

CRYSTALLOGRAPHY AND MATERIAL PREPARATION

A. Alum Crystallography

The alums comprise an extensive group of double salts. The general formula is:



M^{+1} is a monovalent metal ion, M^{+3} is a trivalent metal ion, M^{+6} can be a sulphur, selenium or tellurium ion. Table 2.1 shows whether or not the various combinations of monovalent and trivalent metals form an alum. Some pertinent characteristics of ions in alum salts are presented in Table 2.2.

The space group of the alums is T_h^6 (Pa3). That is, the symmetry elements are those of a primitive cubic bravais lattice with $a/2$ glide plane along $\langle 100 \rangle$ and 3-fold rotation axes. The unit cell customarily chosen contains four formula units. The crystallography and classification of the alums were originally done by Lipson and Beevers¹ and Lipson². Slight differences in the atomic arrangement enable three types of alum structures to be distinguished, termed the α , β and γ types. Each trivalent metal ion has as its nearest neighbours six water molecules forming about the ion a nearly regular octahedron. It is the orientation of this octahedron with respect to the crystal cubic axes that determines the alum type.

Table 2.1 Mono and trivalent metal combinations which form alum salts*.

	Al	Cr	Fe	Co	Ga	In	V	Ti	Mn	Rh	Ir
Na	1	1	0	0	0	0	0	0	0	0	0
K	1	1	1	0	1	0	1	0	0	1	1
NH ₄	1	1	1	0	1	1	1	0	0	1	1
Rb	1	1	1	1	1	1	1	1	1	1	1
Cs	1	1	1	1	1	1	1	1	1	1	1
Tl	1	1	1	1	1	0	1	0	0	1	1

* 1 indicates formation of an alum

Table 2.2 Characteristics of Ions in Alums

Atom	Atomic No.	Ion Formed	No. of Electrons	Ground Config.	Ionic Radius (Å)
Na	11	Na ⁺¹	10	1s ² 2s ² 2p ⁶	0.97
Al	13	Al ⁺³	10	1s ² 2s ² 2p ⁶	0.51
O	8	O ⁻²	10	1s ² 2s ² 2p ⁶	1.32
S	16	S ⁺⁶	10	1s ² 2s ² 2p ⁶	0.30
Cr	24	Cr ⁺³	21	(A) ¹⁸ .3d ³	0.63
Ga	31	Ga ⁺³	28	(A) ¹⁸ .3d ¹⁰	0.62
Rb	37	Rb ⁺¹	36	(K) ³⁶	1.47
Cs	55	Cs ⁺¹	54	(X _e) ⁵⁴	1.67

(A)¹⁸ indicates the argon core 1s²2s²2p⁶3s²3p⁶.

(K)³⁶ indicates the krypton core (")·3d¹⁰4s²4p⁶

(X_e)⁵⁴ indicates the Xenon core (")·4d¹⁰5s²5p⁶

In the α type the [111] axis of the octahedron of the water molecules coincides with the [111] axis of the crystal, but the cubic axes of the octahedron are displaced from the cubic axes of the crystal by a rotation of approximately 9.5° about the [111] direction. Also, the octahedron of water molecules has a small trigonal distortion along the [111] direction. The β alums are described as having nearly regular groups of water molecules with the cubic axes of the octahedron being directed along the cubic axes of the crystal. The γ alums are said to differ from the α and β types in that the sulphate groups of the γ alums are oriented oppositely along the crystal body diagonals to those of the α and β alums. The cubic axes of the octahedron in the γ type are rotated about the crystal [111] direction by about 40° . The only known γ type is the soda alum, $\text{NaAl}(\text{SO}_4)_2 \cdot 12\text{H}_2\text{O}$.

The crystallography of typical members representing each type of alum has been accurately redetermined recently by others, the α alums K, Rb, and $\text{NH}_4\text{Al}(\text{SO}_4)_2 \cdot 12\text{H}_2\text{O}$ by Larson and Cromer¹⁹, the β alum $\text{CsAl}(\text{SO}_4)_2 \cdot 12\text{H}_2\text{O}$ by Cromer, Kay, and Larson²⁰, and the γ alum $\text{NaAl}(\text{SO}_4)_2 \cdot 12\text{H}_2\text{O}$ by Cromer, Kay and Larson²¹. In the α alums the authors found the presence of disordered sulfate groups. That is, some of the sulfate groups in an α alum are inverted along the crystal body diagonals, and the fraction of reversed sulfate groups tends to increase as the cation size decreases. This means that the α alums, with their medium-sized monovalent cations, tend to be like the γ alum which has the smallest monovalent cation, and which has inverted sulfate groups. Furthermore, it was observed that in K alum, the reversal of some of the sulfate groups only appears to affect the position of potassium.

The crystallographic work on the β alum showed that the octahedron of water molecules surrounding an aluminum atom is oriented almost exactly along the crystal axes, and it is only slightly distorted. In the γ alum, the water molecules about the aluminum atom were found to form a perfect octahedron, with the octahedron being rotated by 39.4° . Crystallographic studies indicate that the classification of the alums can best be described by the angle of rotation about a crystal body diagonal of the cubic axes of the octahedron of waters surrounding the trivalent cation.

The unit cell dimensions for the Rb alum, which is an α type, and for Cs alum which is a β type, are given by Wyckoff²² as 12.270 \AA and 12.402 \AA respectively.* These dimensions are evaluated at 25°C . Crystal structures for these salts were not determined, and only the unit cell dimensions are available. For the soda alum, on the other hand, which has recently been redone, the actual location for the atom positions in the unit cell is given by Cromer et al.²¹ The unit cell dimension reported is $12.213 \pm .003 \text{ \AA}$. One quarter of a unit cell of Rb and Na alum is shown in Figures 2.1 and 2.2.² The octahedron of water molecules is shown, for simplicity, around only one trivalent ion, i.e., gallium or aluminum.

B. Material Preparation

The various alum crystals were obtained by mixing solutions of gallic sulphate and the appropriate univalent sulphate in the proportions determined by the alum molecular formula. For Rb alum the ratio of rubidium sulphate to gallic sulphate is 1 to 1.601. For Cs alum the ratio

* Rb alum stands for $\text{RbGa}(\text{SO}_4)_2 \cdot 12\text{H}_2\text{O}$ and Cs alum stands for $\text{CsGa}(\text{SO}_4)_2 \cdot 12\text{H}_2\text{O}$.

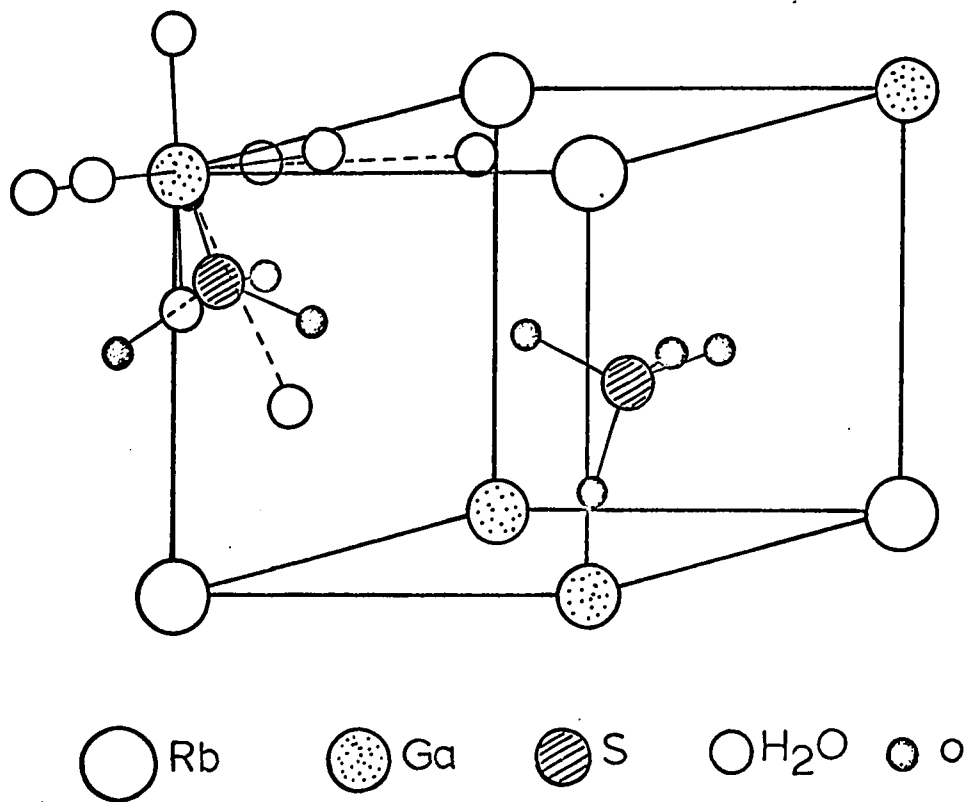


Figure 2.1 One quarter of the unit cell of Rb alum (α-type)

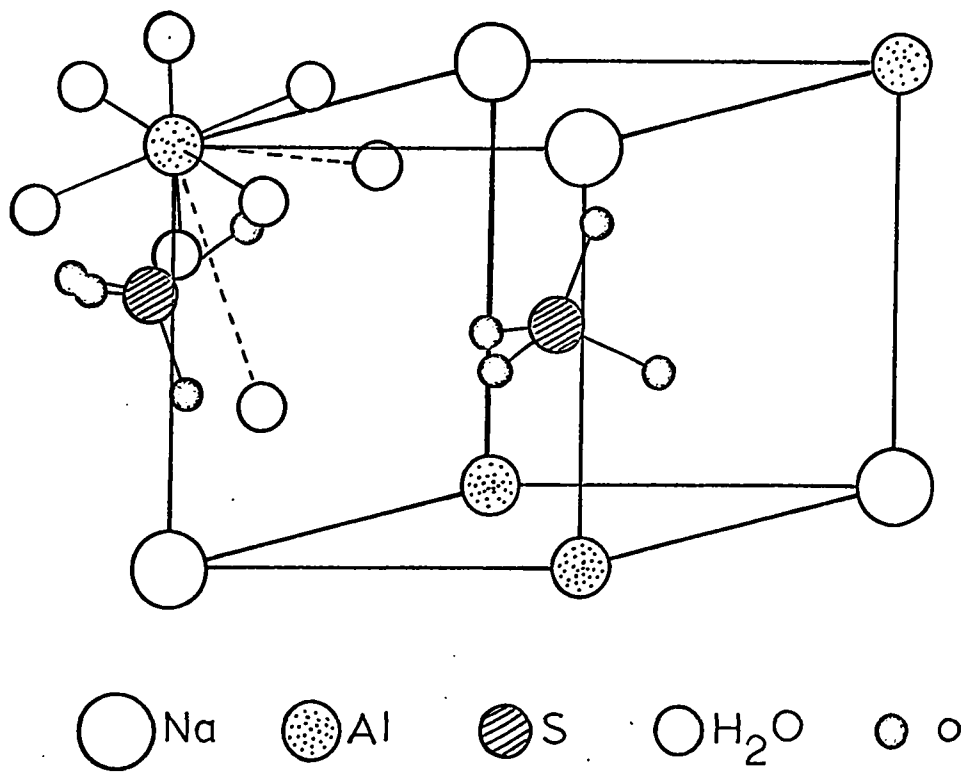


Figure 2.2 One quarter of the unit cell of Na alum (γ -type)

of cesium sulphate to gallic sulphate is 1 to 1.182. For the Na alum^{*}, sodium sulphate and $Al_2(SO_4)_3 \cdot 18H_2O$ were used, their ratio being 1 to 4.692 respectively.

Crystals were obtained in most cases by allowing a saturated alum solution to slowly evaporate at room temperature. In some cases crystals were obtained by allowing a saturated solution above room temperature to cool slowly. In both instances crystals of high quality were obtained. This was attested to by well formed crystal faces and by generally flawless visual appearance. The growth habit of Rb alum was such as to exhibit most often only the {111} faces. Occasionally higher order planes were formed but these were always small in number.

The Cs alum, however, grew in two fairly distinct habits. One of its habits is essentially the same as the Rb alum's, that is the crystal grew with well defined {111} faces and a few higher order planes. The other habit had many higher order faces and consequently only a few large {111} faces. This latter habit was of more common occurrence than the former. In both case, however, the faces were well formed; although in the Cs alums because of the larger number of higher order planes the faces were of smaller area, and this gave the Cs alums a chunkier appearance. The soda alum habit was similar to the Rb alum habit although it was sometime possible to confuse it with the pseudo soda alum.

The Rb and Cs crystals showed a high degree of stability at all temperatures. After many thermal cycles from room to liquid helium temperature in the course of the experiments only slight dulling of the originally sharp interfacial edges developed. The soda alum, on the other hand, was quite

* Na alum stands for $NaAl(SO_4)_2 \cdot 12H_2O$.

unstable and retained its waters of crystallization for several hours only. To prevent this rapid decomposition the crystals were sprayed with several coats of krylon varnish. This procedure maintained the crystals for a period of 2 to 3 weeks. After this time they invariably disintegrated fairly rapidly. Thermal cycling in the case of the soda alum resulted in the crystal's disintegration into many small crystallites even after a single cooling to liquid helium temperature.

The dopant used was chromium sulphate. The even isotope, Cr(52) was obtained by dissolving reagent grade $\text{Cr}_2(\text{SO}_4)_3 \cdot n\text{H}_2\text{O}$. The odd isotope, Cr(53), was obtained as chromium sulphate from Oak Ridge National Laboratory. Chromium (53) was enriched to 96.4 per cent in the sulphate, which was in anhydrous form. Because of this fact some difficulty was encountered in dissolving the chromium sulphate. After application of heat most of the sulphate dissolved. This solution was then filtered several times and used as dopant.

No quantitative measurements of chromium concentration in the grown crystals were made. The lower and upper limits of chromium concentration are, however, known fairly accurately. In no case, with the exception cited below, was more than five milligrams of chromium sulphate added to 1 gramme of alum salt when the dopant was Cr(52), and in the case of Cr(53), at most 3 milligrams were used for 1 gramme of alum salt. The lower limit on the concentration is somewhat uncertain but if one assumes the unlikely situation where only every tenth, say, chromium ion actually available enters the crystal, one obtains for the lower and upper concentration limits .05 to .5 percent and .03 to .3 percent for the even and odd isotopes, respectively. In the case of soda alum there could have been up to 1 percent

chromium in the salt.

In order to verify the cubic nature of the grown crystals typical samples of the alums were examined using an optical two circle goniometer. In all cases, the observed crystal faces could be related to low order planes of the cubic system. This was done by measuring angles formed by sets of planes. This method is illustrated for a typical set of measurements in the stereographic projection of Figure 2.3. Only the very prominent {111} faces are shown. The $70^{\circ} 32'$ angles observed between the large faces agree exactly with the angle between {111} faces in a cubic system.

Rb and Cs alum crystals were also grown from solution in heavy water. Purity of the heavy water was about 99 percent D_2O . No special difficulty was encountered in growing the deuterated crystals. All crystals studied had well developed faces and visually appeared to be of as high quality as the crystals grown from H_2O . In fact Rb (D_2O)* crystals were exceptionally well formed.

C Pseudo soda alum

This crystal grew out of the same solution as did the soda alum. For this reason it will be referred to in this study as the pseudo soda alum. The crystal usually grew in thin elongated form. Its well developed faces appeared to define a monoclinic crystal. This observation was confirmed by x-ray analysis employing the precession camera technique. The results

* (H_2O) or (D_2O) in parenthesis indicates the hydrated or deuterated form of the alum.

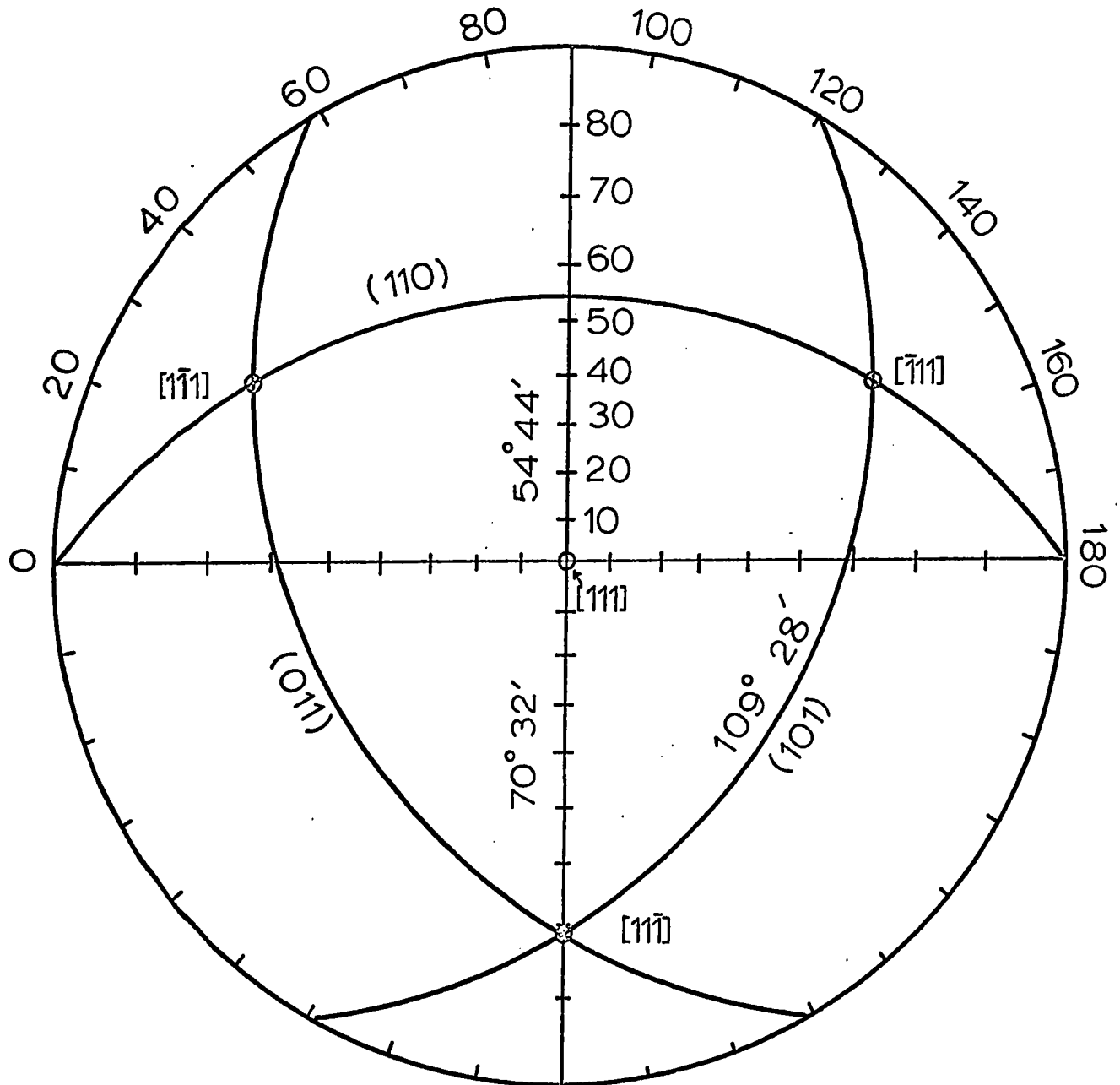


Figure 2.3 Stereographic projection onto the (111) plane of the {111} alum faces

obtained for the crystal parameters are: $a = 21.3 \text{ \AA}$, $b = 8.97 \text{ \AA}$, and $c = 8.28 \text{ \AA}$. The monoclinic angle β equals 92.5° . The space group was found to be either $C2/c$ or Cc . The relation between the crystal axes and the growth habit is shown in Figure 2.4. The pseudo alum exhibited approximately the same stability as did the soda alum. On cooling to liquid helium temperature the crystal did not break up into small crystallites as was the case for the soda alum.

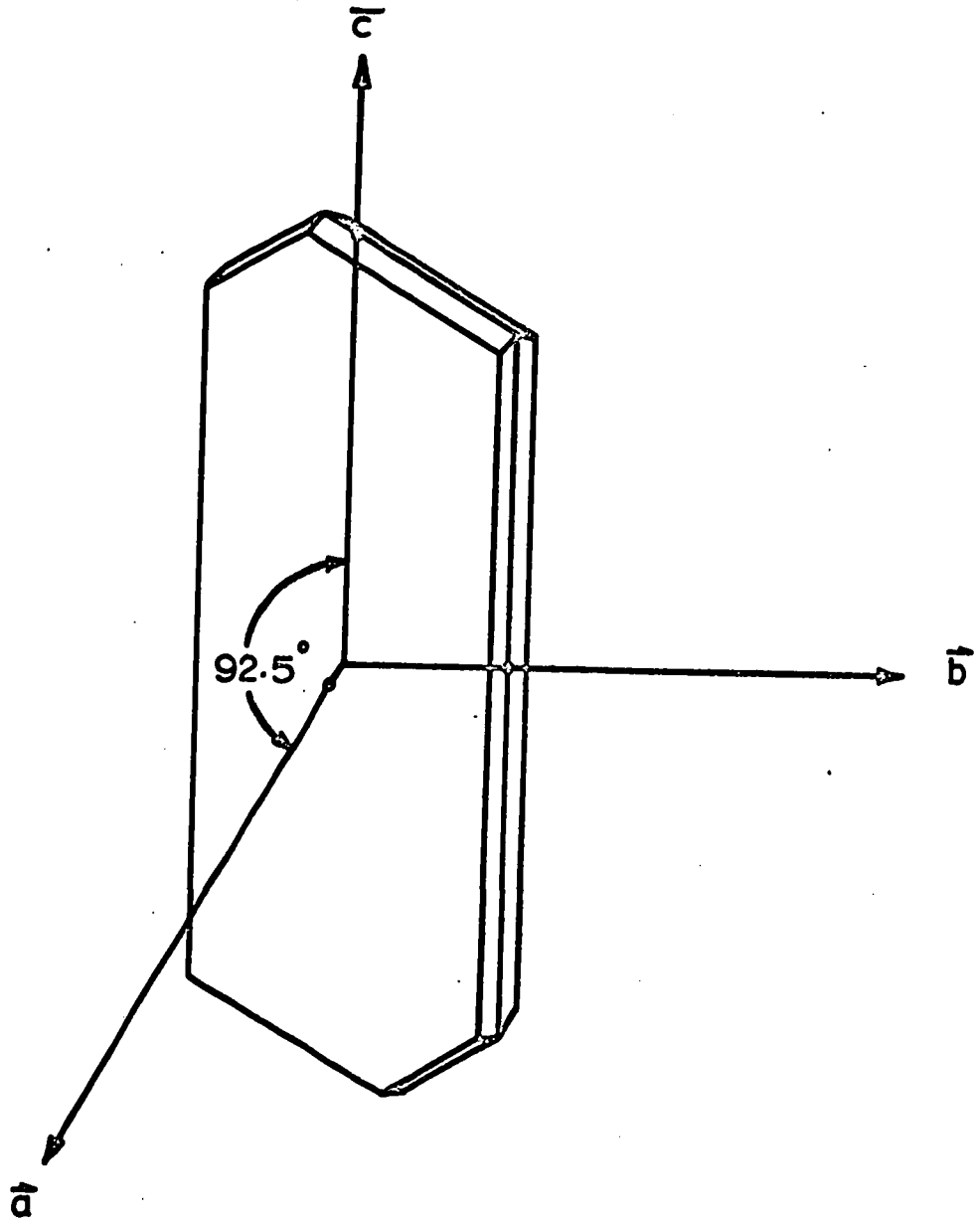


Figure 2.4 Growth habit of pseudo soda alum

CHAPTER III

THEORY

A. Introduction

The important terms in the general Hamiltonian of an ion in a crystalline environment and subjected to an external magnetic field H can be written as²³

$$H = H_E + H_{LS} + H_{SI} + H_Q + H_{CF} + H_{SH} + H_{IH}$$

The meaning of the terms is as follows:

(i) The term H_E represents the total kinetic energy of the electrons, the Coulomb attraction between the electrons and the nucleus, and the repulsion between the individual electrons. It is written as

$$H_E = \sum_i \left(\frac{\vec{p}_i^2}{2m} - \frac{Ze^2}{r_i} \right) + \sum_{i,j} \frac{e^2}{r_{i,j}}$$

where \vec{p}_i is the momentum of the i 'th electron, of mass m and charge e ,

r_i is the position of the i 'th electron with respect to the nucleus,

$r_{i,j}$ is the distance between electron i and electron j , and

Z is the atomic number.

The summation is over all the electrons in the atom. This term gives energy levels which are separated the order of 10^5 cm^{-1} apart.

(ii) H_{LS} gives the energy due to spin-orbit coupling, and may be written as

$$H_{LS} = \sum_{i,j} \lambda_{i,j} \vec{l}_i \cdot \vec{s}_j$$

where \vec{l}_i is the orbital angular momentum of the i 'th electron,
 \vec{s}_j is the spin angular momentum of the j 'th electron, and
 $\lambda_{i,j}$ is an interaction constant, and the summation is over all the electrons in the atom.

If one considers energy states derived from the ground state (given by H_E) the spin orbit interaction may be written more simply as

$$H_{LS} = \lambda \vec{L} \cdot \vec{S}$$

where \vec{L} is the free ion orbital angular momentum, and
 \vec{S} is the free ion spin angular momentum.

The magnitude of this effect varies with the strength of the coupling and the ion state but it is generally between 10^2 and 10^3 cm^{-1} .

(iii) The magnetic interaction between each electron and the nucleus is given by

$$H_{SI} = \sum_i a_i \vec{J}_i \cdot \vec{I}_i$$

where \vec{J}_i is the total angular momentum of the i 'th electron,
 \vec{I}_i is the nuclear spin, and
 a_i is the coupling constant for the interaction

This interaction produces the hyperfine levels which are of the order of 10^{-2} cm^{-1} in separation.

(iv) H_Q describes a very small effect. It is of the order of 10^{-4} cm^{-1} and is attributed to the nuclear quadrupole interaction which is in effect for nuclei with spin greater than 1/2. Its effect can be neglected in the ESR part of this work because the selection rule $\Delta m = 0$ causes the term to vanish for allowed transitions. It must be brought in for ENDOR studies.

(v) The expression for the effect due to the crystal field can be written as

$$H_{CF} = \sum_i e_i V(\vec{r}_i)$$

where $V(\vec{r}_i)$ is the electrostatic potential at the ion due to the ligands with which each electron i interacts. The magnitude of this interaction varies widely and may give a splitting as large as 10^4 cm^{-1} . This term is discussed more fully below.

(vi) The interaction between the total angular momentum of the ion and the external magnetic field H is given by H_{SH} . It is commonly referred to as the Zeeman term and may be written as

$$H_{SH} = \beta \vec{H} \cdot \vec{g} \cdot \vec{J}$$

where g is the spectroscopic splitting tensor,

β is the Bohr magneton ($= eh/4\pi mc$),

$$\vec{J} = \vec{L} + \vec{S}$$

(vii) The effect of H on the nuclear magnetic moment is given by

$$H_{IH} = -\frac{h}{2\pi} \gamma \vec{I} \cdot \vec{H}$$

where γ is gyromagnetic ratio of the nucleus, and

\vec{I} is the spin of the nucleus

This is a small effect, and gives a splitting of about 10^{-4}cm^{-1} . It is taken into account when considering second order effects in the hyperfine interaction. Its effect can also be neglected in ESR studies because the selection rule $\Delta m = 0$ causes the term to vanish for allowed transitions. It must be brought in for ENDOR studies. The various terms considered so far will now be discussed in greater detail and with more specific reference to Cr^{+3} in the alums.

B. Crystal Field Theory (Fine Structure)

The crystal field theory for a paramagnetic ion in a solid assumes that the ion resides in a crystalline electric field due to point charges or point dipoles which are the coordinated ligands lying wholly outside the paramagnetic ion.

The ground state of the free ion Cr^{+3} containing $3d^3$ electrons in its outermost occupied shell is described by ${}^4F_{3/2}$.

In this state the ion has resultant orbital angular momentum given by $L = 3$ and consequently orbital degeneracy is 7. The spin multiplicity is 4 hence the spin is $3/2$. J is $3/2$ also, according to Hund's rule. Bethe²⁴ has shown by group theoretical methods that the 7-fold orbital degeneracy is partially removed by a crystal field of cubic symmetry. The resolution is into a lower orbital singlet and two higher lying orbital triplets. Additional lowering of crystal field symmetry to, say, tetrahedral or orthorhombic will further split the ground state (now an orbital singlet) into two Kramer's doublets as allowed by the 4-fold spin degeneracy and the odd number of electrons in the d subshell. The spin being $3/2$, the doublets are to be associated with $M_S \pm 3/2$ and $M_S \pm 1/2$. The doublets are further split when a constant magnetic field is applied. Kramer's theorem states that a purely electrostatic field acting on a system of an odd number of electrons can never reduce the degeneracy below two. Wigner²⁵ has shown that this degeneracy is related to the invariance of the system under time reversal.

The mechanism via which the distortion from cubic symmetry produces the Kramer doublets is via the spin orbit coupling interaction and may be explained as follows. Starting with the free chromium ion and considering the effect of the crystal field and external magnetic field the energy levels in Figure 3.1 are obtained. Direct action of the cubic component of the crystal field on the F state produces a splitting into an orbital singlet and two orbital triplets.

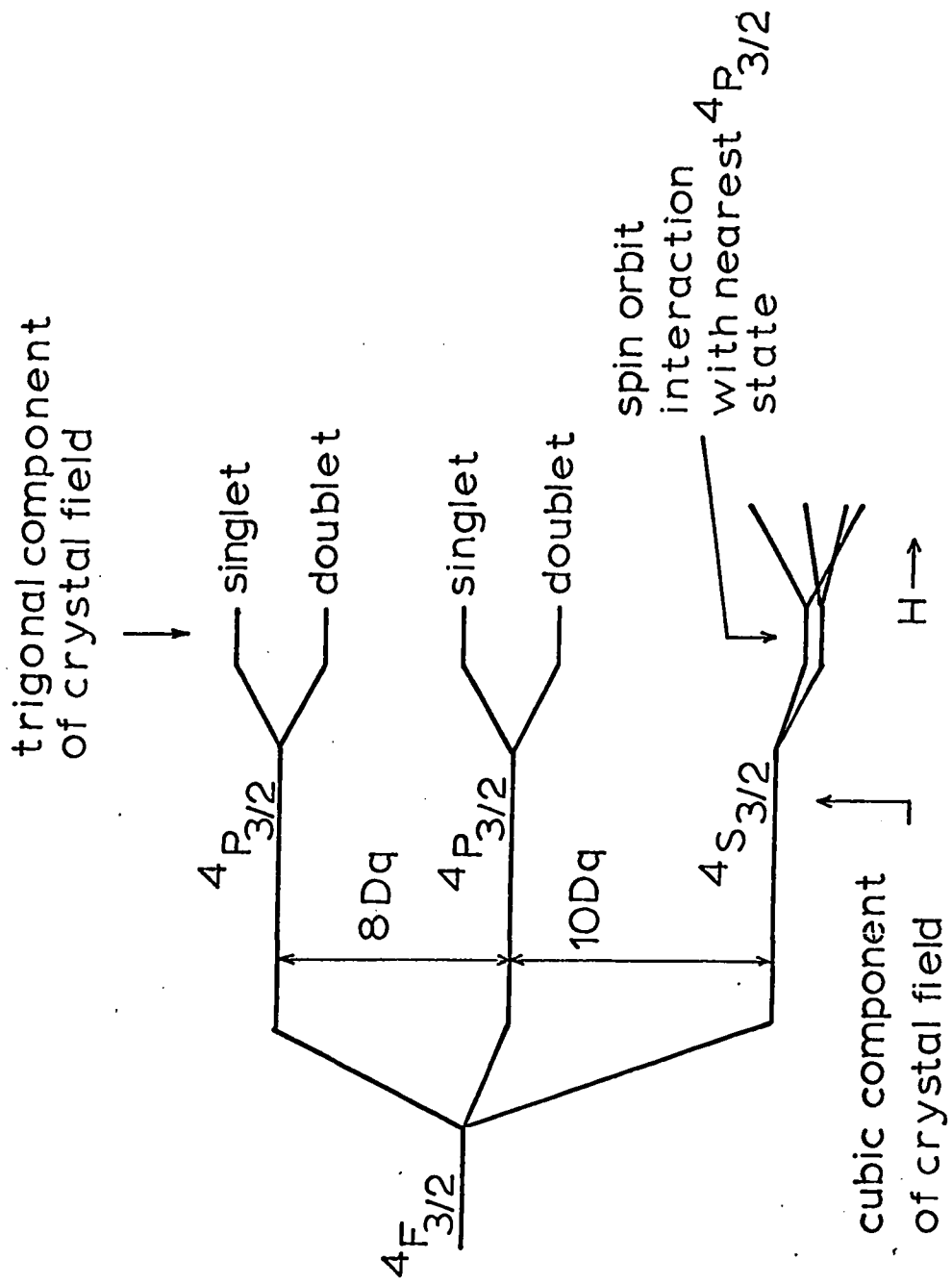


Figure 3.1 Splitting of the $4F_{3/2}$ state of Cr^{3+} by the cubic and trigonal components of the crystal field.

If present, a small additional tetragonal or trigonal component will further split the excited orbitally degenerate states as shown. No direct effect is expected on the ground state since it is an orbital singlet, however, matrix elements for the spin orbit interaction $\vec{L} \cdot \vec{S}$ exist between the ground state and the first excited doublet and singlet. The result is the resolution of the ground state into two doublets. No matrix elements for $L \cdot S$ exist between the highest occurring doublet and singlet and the ground state.²⁶ On this mechanism, therefore, the axial component of the crystal field is only indirectly responsible for the zero field splitting.

Theoretical considerations regarding Kramer's doublets do not indicate which doublet lies lowest. To obtain this information the paramagnetic resonance spectrum must be studied at a sufficiently low temperature so that the effect of spin populations of the levels is observable. The doublet separation is designated $2D$ according to Spin Hamiltonian usage. D is positive when the $M_S = \pm 3/2$ doublet lies above the $M_S = \pm 1/2$ doublet and negative if the converse is true.

C. Hyperfine Interaction

The Hamiltonian for the magnetic interaction of a single electron with the nucleus can be written as follows²⁷.

$$H = gg_I \beta \beta_I \vec{I} \cdot \left\{ \frac{\vec{l}}{r^3} - \frac{\vec{s}}{r^3} + \frac{3\vec{r}(\vec{s} \cdot \vec{r})}{r^5} + \frac{8\pi}{3} \delta(\vec{r}) \vec{s} \right\} \quad (3.1)$$

where g is the electronic g-value
 g_I is the nuclear g-value
 β is the Bohr magneton
 β_I is the nuclear magneton
 I is the nuclear spin
 ℓ is the orbital angular momentum of the electron
 s is the electron spin
 $\delta(r)$ is the Dirac delta function

If several electrons surround the nucleus, the interaction Hamiltonian is the sum of the contributions of the individual electrons. One obtains the interaction energy by multiplying equation (3.1) by $|\psi|^2$ and integrating over the electron coordinates. A simple picture for the hyperfine interaction may be obtained by replacing the quantity in parentheses in equation (3.1) by a vector \vec{H}_e , one then has

$$H \approx \text{constant} (\vec{H}_e \cdot \vec{I}) \quad (3.2)$$

This equation is of the same form as the Zeeman interaction, i.e. an interaction between angular momentum and magnetic field. The \vec{H}_e may be thought of as an effective magnetic field produced at the nucleus by the orbital and spin motion of the electrons. This field quantizes the nuclear magnetic moment into $(2I + 1)$ different orientations causing a perturbation on the electronic system of the atom and splitting each of the four electronic energy levels into $2I + 1 = 4$ sublevels for the case of Cr(53). The four lines are in general unequally spaced.

The interaction energy producing the hyperfine splitting can arise via two essentially different mechanisms. There is the dipolar interaction of magnetic moments due to nuclear and electron spin. This interaction is anisotropic since it depends on the direction joining the electron and nucleus. The first three terms in the parentheses of equation 3.1 represent this interaction. The second mechanism which may contribute to the hyperfine interaction is given by the last term in equation (3.1). This is the so-called Fermi contact term; it is proportional to the unpaired spin density at the nucleus. The unpaired spin density is given by $\lim_{r \rightarrow 0} |\psi(r)|^2$. This quantity is finite for s electrons and zero for all other orbitals. The interaction is isotropic since the unpaired spin density is not field dependent. The chromium ion hyperfine interaction is then expected to be primarily dipole-dipole. The contact term is expected to be zero since the chromium d orbitals have zero spin density at the nucleus. This is a general consideration which should be valid for most transition metal ions since their electron configurations are $3d^x$. Experimentally, however, it is found that measured hyperfine splittings exceed considerably the value predicted by the dipole-dipole interaction.

The concept of configuration mixing is used to partially explain the discrepancy. The ground state for chromium is said not to be made up of d orbitals alone, but may contain small quantities of s character from higher states. Such a ground state would have a resultant unpaired spin density at the nucleus and Fermi's contact term would be operative. There is another mechanism whereby unpaired spin density at the nucleus may arise. This involves core polarization. In this mechanism the unpaired

electrons in the d orbitals tend to polarize s electrons in the inner closed shells. The polarization for ns spin up electron would be different than for the ns spin down electron because Pauli's exclusion principle prevents them from being at the same point in space. The spin densities of the two s electrons would not cancel at the nucleus and unpaired spin density would be produced. Some recent calculations^{28,29} for transition metal ions indicate that the core polarization predicts closer agreement with experiment than does the configuration mixing mechanism.

D. Quadrupole Interaction

Nuclei with $I \geq 1$ possessing electric quadrupole moment will interact with a non-uniform electric field at the nucleus to produce small changes in the energy levels as determined by the A interaction. For a single nucleus the electric quadrupole moment Q is defined by the equation

$$Q = \frac{1}{e} \int \rho r^2 (3 \cos^2 \theta - 1) dv \quad (3.3)$$

where

ρ is the nuclear charge density,

r is the distance from the center of gravity of the nuclear charge to volume element dv

θ is the angle between r and the spin axes z

e is the proton charge

The quadrupole moment is a measure of the out-of-roundness of a nucleus. The Q is positive if the charge distribution is greater along the spin axis (elongated ellipsoid) and negative if it is less (flattened ellipsoid). The quadrupole interaction energy with an electric field gradient of axial symmetry is given by equation (3.4)

$$\begin{aligned}
 W &= \frac{3eQ}{4I(2I-1)} \frac{\partial^2 V}{\partial z^2} \left(I_z^2 - \frac{1}{3} I(I+1) \right) \\
 &= Q' \left(I_z^2 - \frac{1}{3} I(I+1) \right)
 \end{aligned}
 \tag{3.4}$$

The non-uniform electric field at the nucleus is produced by any deviation from spherical symmetry of the electrons belonging to the nucleus. It can also be produced by electrons belonging to ligands in non cubic arrays. Measurement of the quadrupole interaction produces the product of the quadrupole moment with the electric field gradient at the nucleus. Calculation of one of these quantities depends on the knowledge of the other. This product has been measured for Cr(53) in cubic and axial environments and has been found to vary from 10^{-7} to 10^{-4} cm^{-1} respectively^{17,15}. In the ESR part of this work, the quadrupole interaction is not measured because, for the sample orientations studied, the selection rule $\Delta m = 0$ causes the term to vanish for allowed transitions. It is of great importance in the ENDOR measurements since the transitions involved are between nuclear levels and the sensitivity of the method readily measures the interaction.

E. Nuclear Zeeman Interaction

The interaction between the nuclear magnetic moment and the external magnetic field H may be written as

$$W = - \beta_{\text{I}} \vec{H} \cdot \vec{g}_{\text{I}} \cdot \vec{I} \quad (3.5)$$

This equation is analogous to the electronic Zeeman interaction. The interaction energy is field dependent and for $I = 1/2$ and $H=3000$ gauss its magnitude is about $.2 \times 10^{-4} \text{ cm}^{-1}$. Measurement of this interaction can determine the nuclear g factor. The magnetic field as seen by the nucleus is not always simply the applied external field. When an external magnetic field is applied the electronic wave function is changed by an amount proportional to H and the electronic field at the nucleus is modified. A consequence of this is paramagnetic shielding or antishielding. This interaction is called the pseudo-nuclear Zeeman effect after Baker and Bleaney³⁰. The magnetic shielding of the nucleus can be treated phenomenologically according to Geschwind³¹ by writing for H , $H(1 + \sigma)$ where σ is the shielding parameter. Even for orbital singlet ground states, σ can contribute to effective nuclear g value by several percent. One may attempt to calculate σ according to Geschwind's formula,

$$\sigma = - 5.84 \left\langle \frac{1}{r^3} \right\rangle_{\text{a.u.}} \frac{\Delta g}{\lambda (\text{cm}^{-1})} \quad (3.6)$$

where

Δg is the g -value shift from 2.0023

λ is the spin-orbit coupling parameter.

Experimentally $H_0 (1 + \sigma)$ is manifested in an effective nuclear g-value. One can designate the effective g-value as g' ; the nuclear Zeeman term then becomes

$$E = - \vec{H} \cdot \tilde{g}'_I \cdot \vec{I}$$

F. The Spin Hamiltonian

The Hamiltonian for a paramagnetic ion in a crystalline electric field is in general quite complicated. Pryce³² and Abragam and Pryce³³ have developed a very useful method for carrying out the perturbation calculation, and have applied it especially to the iron group. This calculation is based on the fact that transitions between the lowest energy levels are observed in the phenomenon of paramagnetic resonance. If transitions between $2S' + 1$ levels are observed experimentally, then S' can be defined as the fictitious spin of the system. In some cases, e.g. in the $4F_{3/2}$ state of Cr^{+3} the fictitious spin is identical to the free ion spin. Abragam and Pryce transform the various terms in the Hamiltonian into a form involving appropriate angular momentum operators L, S and J . The advantage of using a spin Hamiltonian is that the rather complicated behaviour of the lowest energy levels of the paramagnetic ion in a crystal subjected to a magnetic field can be described in a

relatively simple way by specifying the effective spin, together with a small number of parameters which measure the magnitudes of the various terms in the Hamiltonian. One must then find a model of a crystal field which corresponds to the spin Hamiltonian and which will explain the observed parameters. The various interactions considered so far are now given as terms of a spin Hamiltonian. The terms contain constants and spin operators which are characteristic of the strength and symmetry of each interaction.

(i) Zeeman term

The Zeeman term can be written for the case of an orbital singlet with the g tensor in diagonal form as

$$\begin{aligned}
 H &= \beta \vec{H} \cdot \vec{g} \cdot \vec{S} \\
 &= \beta (H_x \ H_y \ H_z) \begin{bmatrix} g_x & 0 & 0 \\ 0 & g_y & 0 \\ 0 & 0 & g_z \end{bmatrix} \begin{bmatrix} S_x \\ S_y \\ S_z \end{bmatrix} \\
 &= \beta g_x H_x S_x + \beta g_y H_y S_y + \beta g_z H_z S_z
 \end{aligned}$$

For axial symmetry $g_x = g_y = g_{\perp}$; $g_z = g_{\parallel}$

$$H = \beta g_{\parallel} H_z S_z + \beta g_{\perp} (H_x S_x + H_y S_y) \quad (3.7)$$

(ii) Hyperfine term.

Following Abragam and Pryce³³, the hyperfine interaction given by the contact term and dipole-dipole interaction discussed above can be written in the diagonal form as

$$H_{SI} = A I_z S_z + B I_y S_y + C I_x S_x$$

In case of axial symmetry the last two terms may be grouped together as:

$$H = A I_z S_z + B(I_x S_x + I_y S_y) \quad (3.8)$$

(iii) Crystalline electric field interaction

The spin Hamiltonian for an ion with spin S in an anisotropic crystal electric field is $\vec{S} \cdot \tilde{D} \cdot \vec{S}$. This interaction is sometimes called the electronic quadrupole interaction. Referred to the principal axes system for \tilde{D} the term is

$$\begin{aligned} H &= \vec{S} \cdot \tilde{D} \cdot \vec{S} = D_x S_x^2 + D_y S_y^2 + D_z S_z^2 \\ &= D \left\{ S_z^2 - \frac{1}{3} S(S+1) \right\} + E (S_x^2 - S_y^2) \end{aligned} \quad (3.9)$$

where

$$D = (3/2)D_z; \quad E = (1/2)(D_x - D_y) \text{ and}$$

where

D is the axial field term

E is the orthorhombic field term

(iv) Nuclear Quadrupole interaction

This interaction has the same form as the crystalline electric field only now the spin and quadrupole pertain to the nucleus. Its general form is $\vec{I} \cdot \vec{Q}' \cdot \vec{I}$. In analogy to equation (3.9) this can be written as eq. (3.10) when referred to a principal axes system³⁴.

$$\begin{aligned} H &= \vec{I} \cdot \vec{Q}' \cdot \vec{I} = Q'_x I_x^2 + Q'_y I_y^2 + Q'_z I_z^2 \\ &= Q' \left\{ I_z^2 - \frac{1}{3} I(I+1) \right\} + \frac{1}{3} n' (I_x^2 - I_y^2) \end{aligned} \quad (3.10)$$

where $Q' = (3/2)Q'_z$; $n' = (Q'_x - Q'_y)/Q'_z$ and

Q' is the axial term

n' is the orthorhombic term

(v) Nuclear Zeeman interaction

This interaction is described by a term

$$H = -\beta_n \vec{H} \cdot \vec{g}'_n \cdot \vec{I}$$

In analogy to the electronic Zeeman interaction for the axial case, this term is

$$H = -\beta_n g'_{nII} H_z I_z - \beta g_{nI} (H_x I_x + H_y I_y) \quad (3.11)$$

where β_n is the nuclear magneton.

(vi) The Complete Spin Hamiltonian

Combining the terms given in (i) to (v) one has the total Hamiltonian for the case of orthorhombic symmetry. The principal directions for the tensor interactions involved are all assumed to be the same.

$$\begin{aligned}
 H = & D(S_z^2 - \frac{1}{3} S(S+1)) + E(S_x^2 - S_y^2) \\
 & + g_{\parallel} \beta S_z H_z + g_{\perp} \beta (H_x S_x + H_y S_y) \\
 & + AS_z I_z + B(S_x I_x + S_y I_y) \\
 & + Q'(I_z^2 - \frac{1}{3} I(I+1)) + \frac{1}{3} n' (I_x^2 - I_y^2) \\
 & - g'_{\parallel} \beta H_z I_z - g'_{\perp} \beta (H_x I_x + H_y I_y)
 \end{aligned} \tag{3.12}$$

For $^{52}\text{Cr}^{+3}$ we have $I=0$ and the spin Hamiltonian describing the fine structure is

$$H = \beta g_{\parallel} H_z S_z + \beta g_{\perp} (H_x S_x + H_y S_y) + D(S_z^2 - \frac{1}{3} S(S+1)) + E(S_x^2 - S_y^2)$$

The matrix elements form a $(2S+1)(2S+1) = 4 \times 4$ matrix in the $S = 3/2$ manifold. The matrix elements for this Hamiltonian are given below in Table 3.1. For $^{53}\text{Cr}^{+3}$ the inclusion of the hyperfine terms will give a matrix of dimensions $(2S+1)(2I+1) \times (2S+1)(2I+1) = 16 \times 16$ in the $S = 3/2, I = 3/2$ manifold. For the case of axial symmetry the

TABLE 3.1

Matrix of the fine structure spin Hamiltonian

	$ 3/2\rangle$	$ 1/2\rangle$	$ -1/2\rangle$	$ -3/2\rangle$
$\langle 3/2 $	$3/2 g_{II} \beta H_z + D$	$\sqrt{3/2} g_I \beta (H_x - iH_y)$	$\sqrt{3E}$	0
$\langle 1/2 $	$\sqrt{3/2} g_I \beta (H_x + iH_y)$	$1/2 g_{II} \beta H_z - D$	$g_I \beta (H_x - iH_y)$	$\sqrt{3E}$
$\langle -1/2 $	$\sqrt{3E}$	$g_I \beta (H_x - iH_y)$	$-\frac{1}{2} g_{II} \beta H_z - D$	$\sqrt{3/2} g_I \beta (H_x - iH_y)$
$\langle -3/2 $	0	$\sqrt{3E}$	$\sqrt{3/2} g_I \beta (H_x + iH_y)$	$-3/2 g_{II} \beta H_z + D$

Hamiltonian describing the hyperfine structure is.

$$\begin{aligned}
 H &= D(S_z^2 - 1/3 S(S + 1)) + g_{II} \beta S_z H_z + g_{\perp} \beta (H_x S_x + H_y S_y) \\
 &+ A S_z I_z + B (S_x I_x + S_y I_y) \\
 &+ Q'(I_z^2 - (1/3)I(I + 1)) - g'_{nII} \beta_n H_z I_z - g'_{n\perp} \beta_n (H_x I_x + H_y I_y) \quad (3.13)
 \end{aligned}$$

The matrix elements of this spin Hamiltonian are presented in Table 3.2 for the case when magnetic field is parallel to the z axis. In Table 3.3 the matrix elements are listed for the case when the external field is perpendicular to the z axis³⁵.

TABLE 3.2

SPIN HAMILTONIAN MATRIX ELEMENTS INCLUDING THE HYPERFINE STRUCTURE
FOR THE ORIENTATION $H = H_z$.

(i) Diagonal elements

$$\langle M_I \ M_S | H | M_S \ M_I \rangle$$

$$\langle 3/2 \ 3/2 | H | 3/2 \ 3/2 \rangle = (3/2 g_{II} \beta H_z) - 3/2 (g'_{nII} \beta_n H_z) + 9/4 A + D + Q'$$

$$\langle 1/2 \ 3/2 | H | 3/2 \ 1/2 \rangle = (\quad) - 1/2 (\quad) + 3/4 A + D - Q'$$

$$\langle -1/2 \ 3/2 | H | 3/2 - 1/2 \rangle = (\quad) + 1/2 (\quad) - 3/4 A + D - Q'$$

$$\langle -3/2 \ 3/2 | H | 3/2 - 3/2 \rangle = (\quad) + 3/2 (\quad) - 9/4 A + D + Q'$$

$$\langle 3/2 \ 1/2 | H | 1/2 \ 3/2 \rangle = (1/2 g_{II} \beta H_z) - 3/2 (g'_{nII} \beta_n H_z) + 3/4 A - D + Q'$$

$$\langle 1/2 \ 1/2 | H | 1/2 \ 1/2 \rangle = (\quad) - 1/2 (\quad) + 1/4 A - D - Q'$$

$$\langle -1/2 \ 1/2 | H | 1/2 - 1/2 \rangle = (\quad) + 1/2 (\quad) - 1/4 A - D - Q'$$

$$\langle -3/2 \ 1/2 | H | 1/2 - 3/2 \rangle = (\quad) + 3/2 (\quad) - 3/4 A - D + Q'$$

$$\langle 3/2-1/2 | H | -1/2 3/2 \rangle = (-1/2 g_{II} \beta H_z) - 3/2 (g'_{nII} \beta_n H_z) - 3/4 A - D + Q'$$

$$\langle 1/2-1/2 | H | -1/2 1/2 \rangle = (\quad " \quad) - 1/2 (\quad " \quad) - 1/4 A - D - Q'$$

$$\langle -1/2-1/2 | H | -1/2-1/2 \rangle = (\quad " \quad) + 1/2 (\quad " \quad) + 1/4 A - D - Q'$$

$$\langle -3/2-1/2 | H | -1/2-3/2 \rangle = (\quad " \quad) + 3/2 (\quad " \quad) + 3/4 A - D + Q'$$

$$\langle 3/2-3/2 | H | -3/2 3/2 \rangle = (-3/2 g_{II} \beta H_z) - 3/2 (g'_{nII} \beta_n H_z) - 9/4 A + D + Q'$$

$$\langle 1/2-3/2 | H | -3/2 1/2 \rangle = (\quad " \quad) - 1/2 (\quad " \quad) - 3/4 A + D - Q'$$

$$\langle -1/2-3/2 | H | -3/2-1/2 \rangle = (\quad " \quad) + 1/2 (\quad " \quad) + 3/4 A + D - Q'$$

$$\langle -3/2-3/2 | H | -3/2-3/2 \rangle = (\quad " \quad) + 3/2 (\quad " \quad) + 9/4 A + D + Q'$$

(ii) Off diagonal elements

$$\langle \underline{+3/2} \underline{+1/2} | H | \underline{+3/2} \underline{+1/2} \rangle = (3/2 B)$$

$$\langle \underline{-1/2} \underline{+1/2} | H | \underline{+3/2} \underline{-3/2} \rangle = "$$

$$\langle \underline{+3/2} \underline{+1/2} | H | \underline{+1/2} \underline{+1/2} \rangle = "$$

$$\langle \underline{-1/2} \underline{-3/2} | H | \underline{-1/2} \underline{-3/2} \rangle = "$$

$$\langle M_I M_S | H | M_S M_I \rangle$$

$$\langle \underline{+1/2} \underline{+1/2} | H | \underline{+3/2} \overline{+1/2} \rangle = (\sqrt{3} B)$$

$$\langle \underline{+3/2} \overline{+1/2} | H | \underline{+1/2} \underline{+1/2} \rangle = "$$

$$\langle \overline{+1/2} \overline{+1/2} | H | \underline{+1/2} \overline{+3/2} \rangle = "$$

$$\langle \underline{+1/2} \overline{+3/2} | H | \overline{+1/2} \underline{+1/2} \rangle = "$$

$$\langle \underline{+1/2} \overline{+1/2} | H | \underline{+1/2} \underline{+1/2} \rangle = 2 B$$

All other elements in this manifold are zero.

TABLE 3.3

SPIN HAMILTONIAN MATRIX ELEMENTS INCLUDING THE HYPERFINE STRUCTURE
WHEN THE MAGNETIC FIELD IS PERPENDICULUR TO THE Z AXIS.

(i) Diagonal elements.

$$\langle M_I M_S | H | M_S M_I \rangle$$

$$\langle 3/2 \ 3/2 | H | 3/2 \ 3/2 \rangle = (3/2 g_{\perp} \beta H_{\perp}) - 3/2 (g'_{n\perp} \beta H_{\perp}) + 9/4 B - 1/2 D - 1/2 Q'$$

$$\langle 1/2 \ 3/2 | H | 3/2 \ 1/2 \rangle = (\quad " \quad) - 1/2 (\quad " \quad) + 3/4 B - 1/2 D + 1/2 Q'$$

$$\langle -1/2 \ 3/2 | H | 3/2 - 1/2 \rangle = (\quad " \quad) + 1/2 (\quad " \quad) - 3/4 B - 1/2 D + 1/2 Q'$$

$$\langle -3/2 \ 3/2 | H | 3/2 - 3/2 \rangle = (\quad " \quad) + 3/2 (\quad " \quad) - 9/4 B - 1/2 D - 1/2 Q'$$

$$\langle 3/2 \ 1/2 | H | 1/2 \ 3/2 \rangle = (1/2 g_{\perp} \beta H_{\perp}) - 3/2 (g'_{n\perp} \beta H_{\perp}) + 3/4 B + 1/2 D - 1/2 Q'$$

$$\langle 1/2 \ 1/2 | H | 1/2 \ 1/2 \rangle = (\quad " \quad) - 1/2 (\quad " \quad) + 1/4 B + 1/2 D + 1/2 Q'$$

$$\langle -1/2 \ 1/2 | H | 1/2 - 1/2 \rangle = (\quad " \quad) + 1/2 (\quad " \quad) - 1/4 B + 1/2 D + 1/2 Q'$$

$$\langle -3/2 \ 1/2 | H | 1/2 - 3/2 \rangle = (\quad " \quad) + 3/2 (\quad " \quad) - 3/4 B + 1/2 D - 1/2 Q'$$

$$\langle 3/2-1/2 | H | -1/2 3/2 \rangle = (-1/2 g_{\perp} \beta H_{\perp}) - 3/2 (g'_{n\perp} \beta_n H_{\perp}) - 3/4 B + 1/2 D - 1/2 Q'$$

$$\langle 1/2-1/2 | H | -1/2 1/2 \rangle = (\quad " \quad) - 1/2 (\quad " \quad) - 1/4 B + 1/2 D + 1/2 Q'$$

$$\langle -1/2-1/2 | H | -1/2-1/2 \rangle = (\quad " \quad) + 1/2 (\quad " \quad) + 1/4 B + 1/2 D + 1/2 Q'$$

$$\langle -3/2-1/2 | H | -1/2-3/2 \rangle = (\quad " \quad) + 3/2 (\quad " \quad) + 3/4 B + 1/2 D - 1/2 Q'$$

$$\langle 3/2-3/2 | H | -3/2 3/2 \rangle = (-3/2 g_{\perp} \beta H_{\perp}) - 3/2 (g'_{r\perp} \beta_r H_{\perp}) - 9/4 B - 1/2 D - 1/2 Q'$$

$$\langle 1/2-3/2 | H | -3/2 1/2 \rangle = (\quad " \quad) - 1/2 (\quad " \quad) - 3/4 B - 1/2 D + 1/2 Q'$$

$$\langle -1/2-3/2 | H | -3/2-1/2 \rangle = (\quad " \quad) + 1/2 (\quad " \quad) + 3/4 B - 1/2 D + 1/2 Q'$$

$$\langle -3/2-3/2 | H | -3/2-3/2 \rangle = (\quad " \quad) + 3/2 (\quad " \quad) + 9/4 B - 1/2 D - 1/2 Q'$$

(ii) Off-diagonal elements

$$\langle M_I \quad M_S | H | M_S \quad M_I \rangle$$

$$\langle \bar{+}1/2 \quad 3/2 | H | 3/2 \underline{+}3/2 \rangle = (\sqrt{3/2}) Q'$$

$$\langle \bar{+}3/2 \quad 3/2 | H | 3/2 \underline{+}1/2 \rangle = "$$

$$\langle \bar{+}1/2 \quad 1/2 | H | 1/2 \underline{+}3/2 \rangle = "$$

$$\langle \bar{+}3/2 \quad 1/2 | H | 1/2 \underline{+}1/2 \rangle = "$$

$$\langle \bar{+}1/2 - 1/2 | H | -1/2 \underline{+}3/2 \rangle = "$$

$$\langle \bar{+}3/2 - 1/2 | H | -1/2 \underline{+}1/2 \rangle = "$$

$$\langle \bar{+}1/2 - 3/2 | H | -3/2 \underline{+}3/2 \rangle = "$$

$$\langle \bar{+}3/2 - 3/2 | H | -3/2 \underline{+}1/2 \rangle = "$$

$$\langle \underline{+}3/2 \underline{+}1/2 | H | \underline{+}3/2 \underline{+}1/2 \rangle = (3/2) A$$

$$\langle \bar{+}1/2 \underline{+}1/2 | H | \underline{+}3/2 \bar{+}3/2 \rangle = "$$

$$\langle \underline{+}3/2 \bar{+}3/2 | H | \bar{+}1/2 \underline{+}1/2 \rangle = "$$

$$\langle \bar{+}1/2 \bar{+}3/2 | H | \bar{+}1/2 \bar{+}3/2 \rangle = "$$

$$\langle \underline{+1/2} \underline{+1/2} | H | \underline{+3/2} \bar{\underline{+1/2}} \rangle = \sqrt{3} A$$

$$\langle \underline{+3/2} \bar{\underline{+1/2}} | H | \underline{+1/2} \underline{+1/2} \rangle = "$$

$$\langle \bar{\underline{+1/2}} \bar{\underline{+1/2}} | H | \underline{+1/2} \bar{\underline{+3/2}} \rangle = "$$

$$\langle \underline{+1/2} \bar{\underline{+3/2}} | H | \bar{\underline{+1/2}} \bar{\underline{+1/2}} \rangle = "$$

$$\langle \underline{+1/2} \bar{\underline{+1/2}} | H | \underline{+1/2} \bar{\underline{+1/2}} \rangle = 2 A$$

$$\langle \underline{+3/2} \bar{\underline{+1/2}} | H | \underline{+3/2} \bar{\underline{+3/2}} \rangle = (\sqrt{3}/2) D$$

$$\langle \underline{+1/2} \bar{\underline{+1/2}} | H | \underline{+3/2} \bar{\underline{+1/2}} \rangle = "$$

$$\langle \bar{\underline{+1/2}} \bar{\underline{+1/2}} | H | \underline{+3/2} \bar{\underline{+1/2}} \rangle = "$$

$$\langle \bar{\underline{+3/2}} \bar{\underline{+1/2}} | H | \underline{+3/2} \bar{\underline{+3/2}} \rangle = "$$

$$\langle \underline{+3/2} \bar{\underline{+3/2}} | H | \underline{+1/2} \bar{\underline{+3/2}} \rangle = "$$

$$\langle \underline{+1/2} \bar{\underline{+3/2}} | H | \underline{+1/2} \underline{+1/2} \rangle = "$$

$$\langle \bar{\underline{+1/2}} \bar{\underline{+3/2}} | H | \underline{+1/2} \bar{\underline{+1/2}} \rangle = "$$

$$\langle \bar{\underline{+3/2}} \bar{\underline{+3/2}} | H | \underline{+1/2} \bar{\underline{+3/2}} \rangle = "$$

All other matrix elements in this manifold are zero.

G. ESR transitions and energy levels for chromium in alums

(i) Fine structure

Using the selection rules $\Delta M_S = \pm 1$, $\Delta M_I = 0$, one can find the magnetic field positions for the fine structure transitions. This has been done to fourth-power in E for the case of orthorhombic symmetry. The equations for transitions when the magnetic field direction is along the Z axis are:

$$\begin{aligned}
 H_{1, M_S(1/2 \rightarrow -3/2)} &= H_0 - 2D + \frac{3E^2 D}{H_1^2 - D^2} - \frac{9}{8} E^4 \left[\frac{1}{(H_1 - D)^3} - \frac{1}{(H_1 + D)^3} \right] \\
 H_{2, M_S(1/2 \rightarrow -1/2)} &= H_0 - 3E^2 \left[\frac{H_2^2}{(H_2 + D)(H_2 - D)} \right] + \frac{9}{8} E^4 \left[\frac{1}{(H_2 - D)^3} + \frac{1}{(H_2 + D)^3} \right] \\
 H_{3, M_S(1/2 \rightarrow 3/2)} &= H_0 + 2D - \frac{3E^2 D}{H_3^2 - D^2} - \frac{9}{8} E^4 \left[\frac{1}{(H_3 + D)^3} - \frac{1}{(H_3 - D)^3} \right]
 \end{aligned} \tag{3.14}$$

where

$$H_0 = h\nu/g\beta H$$

For the case of axial symmetry the analogous expressions are obtained by setting $E = 0$ in equations (3.14).

The equations given above may be used for other orientations provided suitable transformation of D, E and g parameters is performed. The transformations between the three principal axes are given in Table 3.4

Table 3.4 Transformation of D, E and g amongst the three principal axes.

D'	E'	g'	axis
$- 1/2 (D-3E)$	$- 1/2(E+D)$	g_x	x
$- 1/2 (D+3E)$	$- 1/2(E-D)$	g_y	y
D	E	g_z	z

(ii) Fine plus hyperfine structure

The 16 X 16 matrix can be diagonalized exactly using numerical methods to obtain energy levels for a given magnetic field and a specific choice of fine and hyperfine structure constants. Also the matrix may be diagonalized to second-order in perturbation theory to give approximate values of the parameters. In either of these ways one may compare the experimentally

measured transitions with theoretical values. To second-order, the energy levels including the hyperfine interactions, are given below for the case of axial symmetry¹⁵. The orientation of H is along the symmetry axis.

$$\begin{aligned}
 E_{M,m} = & g_{II} \beta H_z M + D [M^2 - 1/3 S(S + 1)] \\
 & + AmM - g'_n \beta_n H_z m + Q' [m^2 - 1/3 I(I + 1)] \\
 & + \frac{1/4B^2 [S(S + 1) - M(M + 1)][I(I + 1) - m(m-1)]}{-g\beta H - D(2M + 1) + A(M-m + 1)} \\
 & - \frac{1/4B^2 [S(S + 1) - M(M - 1)][I(I + 1) - m(m+1)]}{g\beta H + D(2M - 1) + A(m - M + 1)}
 \end{aligned} \tag{3.15}$$

These equations may be used to obtain the energy separation between hyperfine levels; these separations correspond to the ENDOR transition frequencies. For the $M_S = + 3/2$ multiplet one has:

$$\begin{aligned}
 h\nu_{(m=3/2 \rightarrow 1/2)} & = 1.5A + 2Q' - g'_n \beta_n H_z - \frac{9B^2}{4[2D + g_{II} \beta H_z]}
 \end{aligned}$$

$$h\nu \quad (m = 1/2 \rightarrow -1/2) = 1.5A - g'_n \beta_n H_z + \frac{9B^2}{4[2D+g_{II}\beta H_z]} - \frac{12B^2}{4[2D+g_{II}\beta H_z - A]}$$

$$h\nu \quad (m = -1/2 \rightarrow -3/2) = 1.5A - 2Q' - g'_n \beta_n H_z + \frac{12B^2}{4[2D+g_{II}\beta H_z - A]} - \frac{9A^2}{4[2D-2A+g_{II}\beta H_z]}$$

(3.16)

For the $M_S = -3/2$ multiplet the equations are:

$$h\nu \quad (m = 3/2 \rightarrow 1/2) = 1.5A - 2Q' + g'_n \beta_n H_z + \frac{12B^2}{4[2D-A-g_{II}\beta H_z]} - \frac{9B^2}{4[2D-2A-g_{II}\beta H_z]}$$

$$h\nu \quad (m = 1/2 \rightarrow -1/2) = 1.5A + g'_n \beta_n H_z + \frac{9B^2}{4[2D-g_{II}\beta H_z]} - \frac{12B^2}{4[2D-A-g_{II}\beta H_z]}$$

$$h\nu \quad (m = -1/2 \rightarrow -3/2) = 1.5A + 2Q' + g'_n \beta_n H_z - \frac{9A^2}{4[2D-g_{II}\beta H_z]} \quad (3.17)$$

H. ESR Line Widths

In paramagnetic resonance the two major causes of line broadening are the interaction between the paramagnetic ions and the lattice, and the interaction between the ions themselves. These interactions have often been treated as giving relaxation effects, characterized by the spin-lattice relaxation time τ and the spin-spin relaxation time.

(i) Spin-lattice interaction. The inverse of the spin-lattice relaxation time is a measure of the rate at which a spin exchanges a whole quantum of energy with the lattice. The theory of this is mainly due to Van Vleck³⁶. The mechanism considered is one in which the thermal vibrations of the lattice give a fluctuating crystalline electric field. The spin-orbit coupling plays an essential role as the mechanism by which the spin of the paramagnetic ion feels the effect of the thermal vibrations. The development of the theory shows that the spin-lattice relaxation time τ is strongly temperature dependent, becoming longer as the temperature is reduced. The theory also shows that τ depends very markedly on the separation between the ground state and the first excited state. If this separation is large then τ is long, and if the separation is small τ is short.

(ii) Spin-spin interaction. The broadening due to this process arises from the interaction between the paramagnetic dipoles. There is no dependence on temperature due to this broadening, and the effect can only be reduced by separating the magnetic carriers. A picture of the broadening process can be obtained as follows. The magnetic moment of

each ion is regarded as precessing about the external magnetic field H , and can be resolved into a component which is steady and directed along H , together with a rotating component perpendicular to H . The steady component sets up a steady field at neighbouring ion positions, and so the ions behave as if they were in a magnetic field which is slightly different from the external magnetic field. The rotating component sets up a rotating magnetic field. If this rotating field has the same frequency as the other paramagnetic ions, then there will be a couple acting on the steady component of the magnetic moment of the latter ion, tending to change its direction. The first process gives a broadening which is similar to that which arises from using an inhomogeneous magnetic field, and the second gives a resonance broadening because it tends to reduce the lifetime of an ion in a given state.

J. Double Resonance

Double resonance is the observation of nuclear magnetic resonance via the electron spin resonance. The scheme which was developed by Feher¹³ permits a direct measurement of the hyperfine level spacings. The hyperfine structure constant A , B , Q' and g'_n can be accurately calculated.

The double resonance technique depends on the nucleus having a nuclear spin, that is, on hyperfine structure. The hyperfine structure may arise through the interaction of the electrons of the paramagnetic ion with its own nuclear magnetic moment or with the nuclear magnetic moments of the surrounding diamagnetic ions - sometimes called superhyperfine structure.

The Feher mechanism of double resonance can be explained using the four level energy diagram in Figure 3.2. At thermal equilibrium the lower levels are more densely populated than the upper levels in the ground state, the distribution being given by

$$\frac{N_b}{N_c} = \exp \frac{\Delta E}{kT} \approx 1 + \frac{\Delta E}{kT}$$

where N_b is the number of spins in level b, N_c is the number in level c, and ΔE is the energy spacing between the levels. The approximation is valid only for $\Delta E \ll kT$. If the total number of spins in the ground state is $4N$ the levels will be populated as in case 1 of Figure 3.2. We can then write

$$\frac{N_b}{N_c} \approx 1 + \frac{\Delta E}{kT}$$

$$= \frac{1+\epsilon}{1-\epsilon}$$

$$\approx 1 + 2\epsilon$$

where $\epsilon = \Delta E/2 kT \ll 1$. The population difference between adjacent hyperfine levels has been ignored because of the very small energy spacing in comparison with the larger splitting. A low power microwave transition now applied will not change the distribution of the levels because the average time for an upward transition is larger than the average time for a downward transition by relaxation; and so the populations will remain

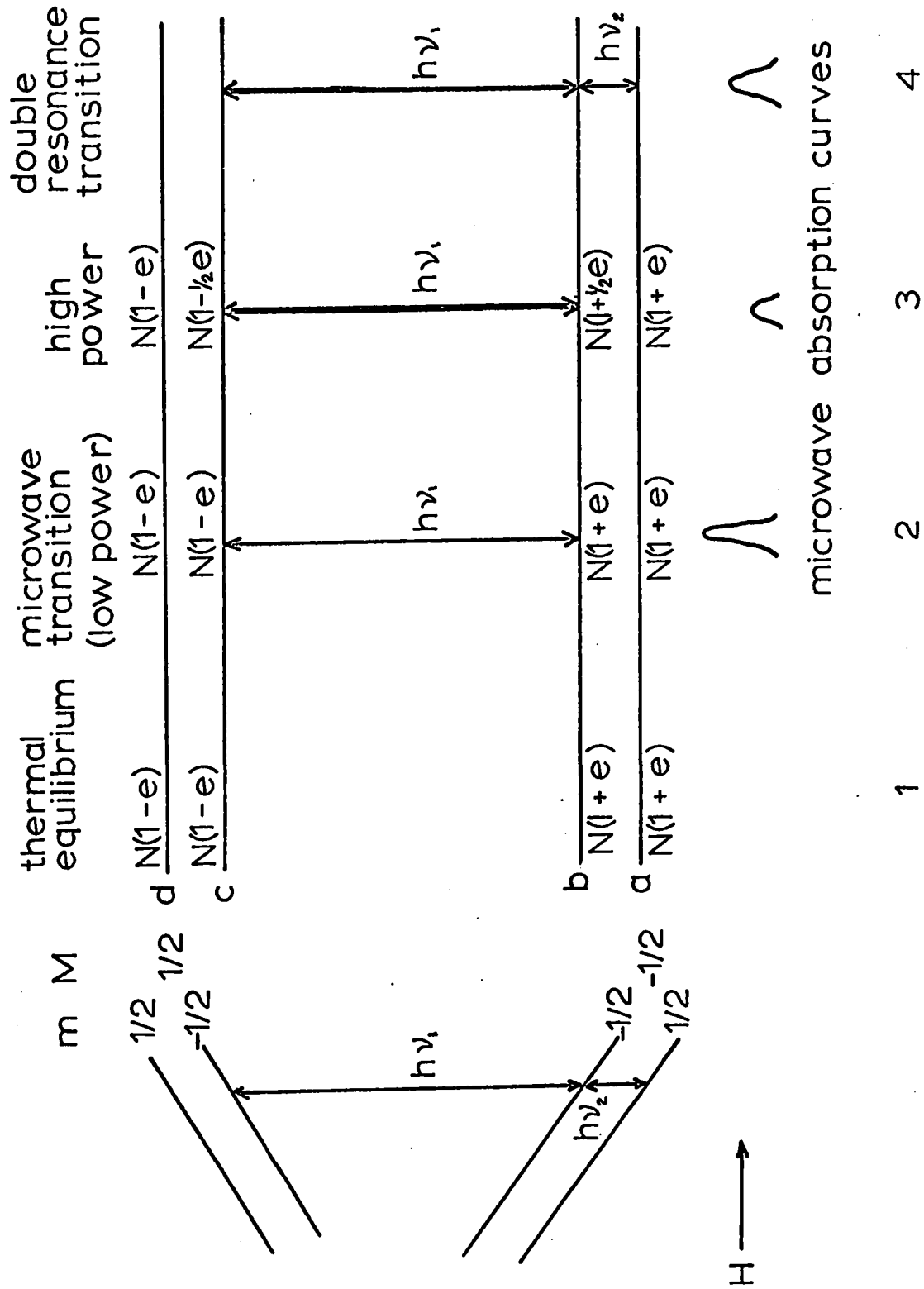


Figure 3.2 Populations in a Double Resonance Experiment

as in case 2. If the microwave power is now increased sufficiently the situation will be, for example, as in case 3, with the microwave transition being nearly saturated. The population difference of levels b and c have changed, now being more nearly equal, and the detected microwave signal consequently will be nearly of zero intensity. The saturation occurs because at high microwave power the average time for an upward transition is smaller than the average time for a downward transition by relaxation; and so some spins will accumulate in the upper level making the two levels concerned more nearly equal in population. The ratio of the distribution in the levels b and c is now given by

$$\begin{aligned} \frac{N_b}{N_c} &\approx 1 + \frac{\Delta E}{kT_s} \\ &= \frac{1 + 1/2\epsilon}{1 - 1/2\epsilon} \\ &\approx 1 + \epsilon \end{aligned}$$

where T_s is the spin temperature. In this case $\epsilon = \Delta E/kT_s$ and $T_s = 2T$ indicating that the spin temperature has been doubled. The doubling of the spin temperature was used as a convenient but arbitrary example.

Because of the saturation effect the adjacent hyperfine levels now have different populations. One can now induce nuclear transitions between the hyperfine levels as shown in case 4. This changes the population difference of the electronic levels making the difference between levels

involved in ESR transitions greater. Consequently this causes the electron resonance signal to reappear. The ENDOR frequency at this point is recorded. In general the situation may be considerably more involved because of a number of relaxation effects and incomplete saturation of the various transitions.

CHAPTER IV

EQUIPMENT

A Introduction

In the course of this study two X-band spectrometers were used. One spectrometer was of commercial design and was manufactured by Hilger and Watts Ltd. of England. The other spectrometer, utilizing superheterodyne detection, was constructed in this laboratory by the author. Commercially available components were used in the construction of this spectrometer. Both instruments could be operated at room, liquid nitrogen and liquid helium temperatures.

B Commercial X-band Spectrometer

X-band power, at a nominal frequency of 9.4 GHz, was obtained from a klystron capable of supplying about 35 mW. The principle of operation is as follows. Microwave energy from the klystron is divided into two branches. One branch feeds the automatic frequency control (AFC) loop and the other is utilized in the detection system. Frequency stabilization is accomplished by using a transmission cavity as a reference. The klystron was first tuned to the resonance frequency of the sample cavity. The frequency of the reference cavity is then tuned to coincidence with the sample cavity frequency.

Finally the klystron frequency is locked to the reference cavity. The correction voltage added to the reflector voltage of the klystron is proportional to the frequency difference between the reference transmission cavity and the klystron. The sign of the correction voltage is determined by the positive or negative deviation of the klystron frequency with respect to the reference cavity frequency.

In order to detect the signal, it is common to modulate the external magnetic field with a small a.c. component. In this case a 100 kHz oscillator coupled to a small coil in the microwave cavity was used. Amplitude of the a.c. field was about 1 gauss. Whenever the external magnetic field satisfied the resonance condition ($h\nu = g\beta h$) the complex susceptibility of the sample is altered and the reflection coefficient of the cavity alters; so unbalancing a magic-T bridge. The out of balance signal passes through a 100 kHz preamplifier and narrow band amplifier to a phase-sensitive detector (PSD). The PSD receives its reference signal from the 100 kHz oscillator adjustable in phase relative to the modulation. The PSD produces a derivative of the absorption or dispersion signal, depending on the balance condition of the magic-T. The time constant of the output circuit of the PSD is adjustable to suit the various sweep rates of the external magnetic field, the signal being presented on a strip chart recorder.

The external magnetic field was produced by an 8 inch magnet with a rotating base. Fields of up to 14 kgauss could be readily obtained, although in this study it was not required to go above 8 kgauss. Almost linear sweeps were obtainable in this range. Field stability was achieved by current regulation and for steady state modes the resolution was about

100 mgauss. Field homogeneity was high, this is shown by noting that proton resonant frequency did not change perceptibly when the proton probe was moved within the volume occupied by the sample cavity.

C X-band Superheterodyne ESR and ENDOR Spectrometer

The superheterodyne spectrometer was constructed in this laboratory utilizing commercially available components. Following Llewellyn, Whittlestone and Williams³⁷, a single klystron was used as the power source for both the sample cavity and the local oscillator (LO). The present spectrometer differs from the one used by these workers in that they obtained the LO power by frequency modulating the klystron and separating one of the resulting side bands. In our case a portion of the microwave power was removed via a directional coupler and amplitude modulated by a microwave switch to produce side bands about the carrier frequency. This system is an improvement over the method of Brown, Mason and Thorpe³⁸ who amplitude modulated the entire klystron output and then selected a fraction of a side band as a source of LO power. The disadvantage of their method, as pointed out by Buckmaster and Dering,³⁹ is that they did not remove from the cavity power side bands generated in the modulation process. A consequence of this fact is that the IF amplifier will saturate at lower microwave power (with subsequent loss in sensitivity) than if the side bands were removed.

The source of microwave power in this spectrometer was a specially selected low noise Varian X-band reflex klystron capable of producing about 350 mW. A block diagram of the ESR system is shown in Figure 4.1, and the

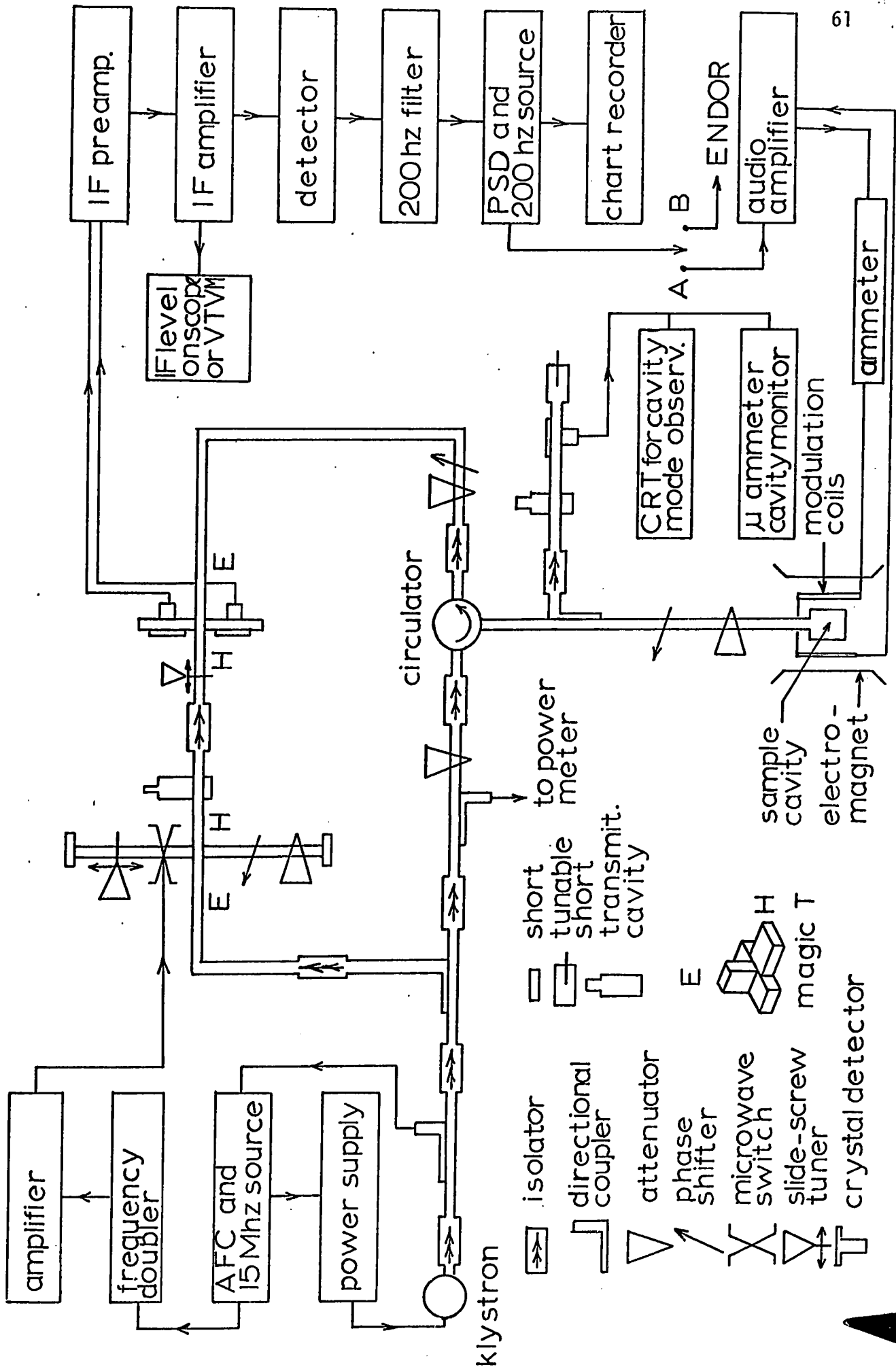
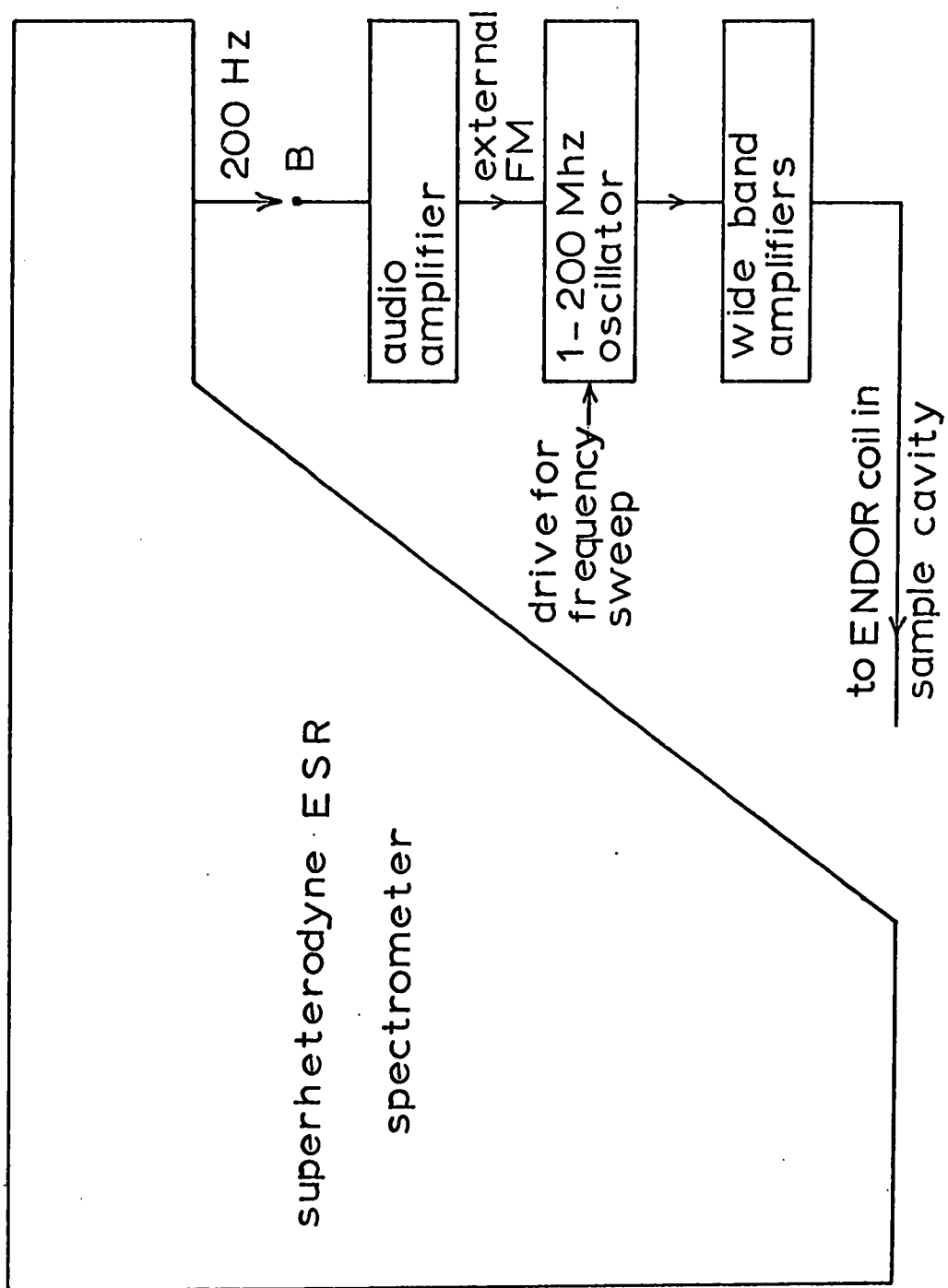


Figure 4.1 X-band superheterodyne ESR spectrometer

block diagram of the modification for ENDOR is shown in Figure 4.2.

The spectrometer operates as follows. The klystron frequency is mechanically tuned to the resonant frequency of the sample cavity. The klystron frequency is then stabilized against a high harmonic of a stable crystal oscillator which is temperature controlled. Electronic tuning of the klystron is possible via the frequency stabilizer for exact frequency coincidence with the sample cavity.

Frequency stabilized microwave power is fed via a 10db coupler to a magic T, one arm of which contains a microwave switch. The microwave switch is driven by a 30 MHz signal derived from an auxiliary output of the frequency stabilizer. The microwave switch driven by the 30 MHz signal amplitude modulates the microwave power in that arm of the magic T. Consequently, side bands are produced and microwave energy is available at the center frequency and 30 MHz above and below the carrier. One of these side arms, usually the stronger one, is selected by tuning the high Q transmission cavity. In this way microwave power 30 MHz away from the carrier is obtained and made available in the H arm of a second magic T. This magic T is in effect a frequency mixer and contains two balanced crystals. Incident on the E arm of the balanced mixer is the RF carrier reflected from the sample cavity and at the center frequency. The two signals are mixed in the balanced mixer and the intermediate frequency (IF) is obtained. In the actual detection of paramagnetic absorption the microwave bridge, consisting of a circulator, is close to balance so that offresonance only a small constant microwave level is present in the E arm of the mixer. On energy absorption by the sample the reflection coefficient of the cavity changes, further unbalancing the microwave bridge. This in turn produces a larger



superheterodyne ESR spectrometer

Figure 4.2 X-band ENDOR spectrometer

microwave level in the E arm and thereby a larger IF signal is produced; the change in the IF level being related to the amount of paramagnetic absorption.

The customary field modulation in this case is at 200 Hz, the signal being derived from an auxiliary output of the PSD and amplified before being applied to a set of Helmholtz coils mounted on the magnet pole faces. The effect of this modulation, as the external field is slowly swept through resonance, is to amplitude modulate at 200 Hz the reflected power from the cavity. The IF is consequently amplitude modulated at the same frequency. After IF amplification a crystal detector stage picks up the 200 Hz signal, riding on the slowly varying IF level due to paramagnetic absorption, which is then amplified and filtered at 200 Hz. It is then fed to the PSD where the 200 Hz signal is integrated and a derivative of the absorption or dispersion signal, depending on the type of unbalance of the microwave bridge, is produced. The PSD output is shown on a strip chart recorder. The time constant of the PSD could be varied for optimum signal to noise ratio for a given magnetic sweep rate.

The ENDOR detection scheme is only slightly different. In this case the magnetic field is constant and no field modulation is employed. Instead, the magnetic field is centered on an ESR absorption line which is made partially power saturated, and the microwave bridge is brought close to balance. It is the ENDOR signal generator (1 to 220 MHz oscillator) which is slowly frequency swept. The 200 Hz signal from the PSD is utilized to FM modulate the ENDOR signal generator. When absorption at an ENDOR frequency occurs, the microwave bridge is unbalanced and a 200 Hz modulated IF is produced as in straight ESR detection.

Superhet spectrometers are notoriously difficult to operate, this being due primarily to the difficulty of maintaining a constant microwave bridge balance for extended times under high gain conditions. The usual design incorporates a slide-screw tuner in the cavity arm of the bridge. With this arrangement it was possible to maintain bridge balance for several minutes only. This barely suffices for measurement purposes when absorption frequencies are known; searching for them is extremely tedious and time consuming because one constantly has to rebalance the microwave bridge. The bridge stability was extended by a factor greater than 10 at the highest gains and by about 30 times at lower gains, by replacing the slide screw tuner by a precision attenuator and precision phase shifter. The significance of precision components in attaining a high degree of bridge balance for extended periods of time is discussed in detail by Buckmaster and Dering⁴⁰.

D X-BAND ESR CAVITIES

(i) Rectangular cavity

This cavity was rectangular and operated in the TE_{014} mode. A diagram of this system is shown in Figure 4.3. The 100 KHz magnetic field modulation is provided by a single turn of copper wire, mounted as shown on the bottom plate. Samples under investigation were placed within this loop in one of two ways. For studies in the (111) plane the crystals were placed with the (111) face flat on the bottom plate and within the 100 KHz loop. Since the waveguide is vertical, rotation of the magnet base sufficed for studies in this plane. For work in (110) plane the crystals were

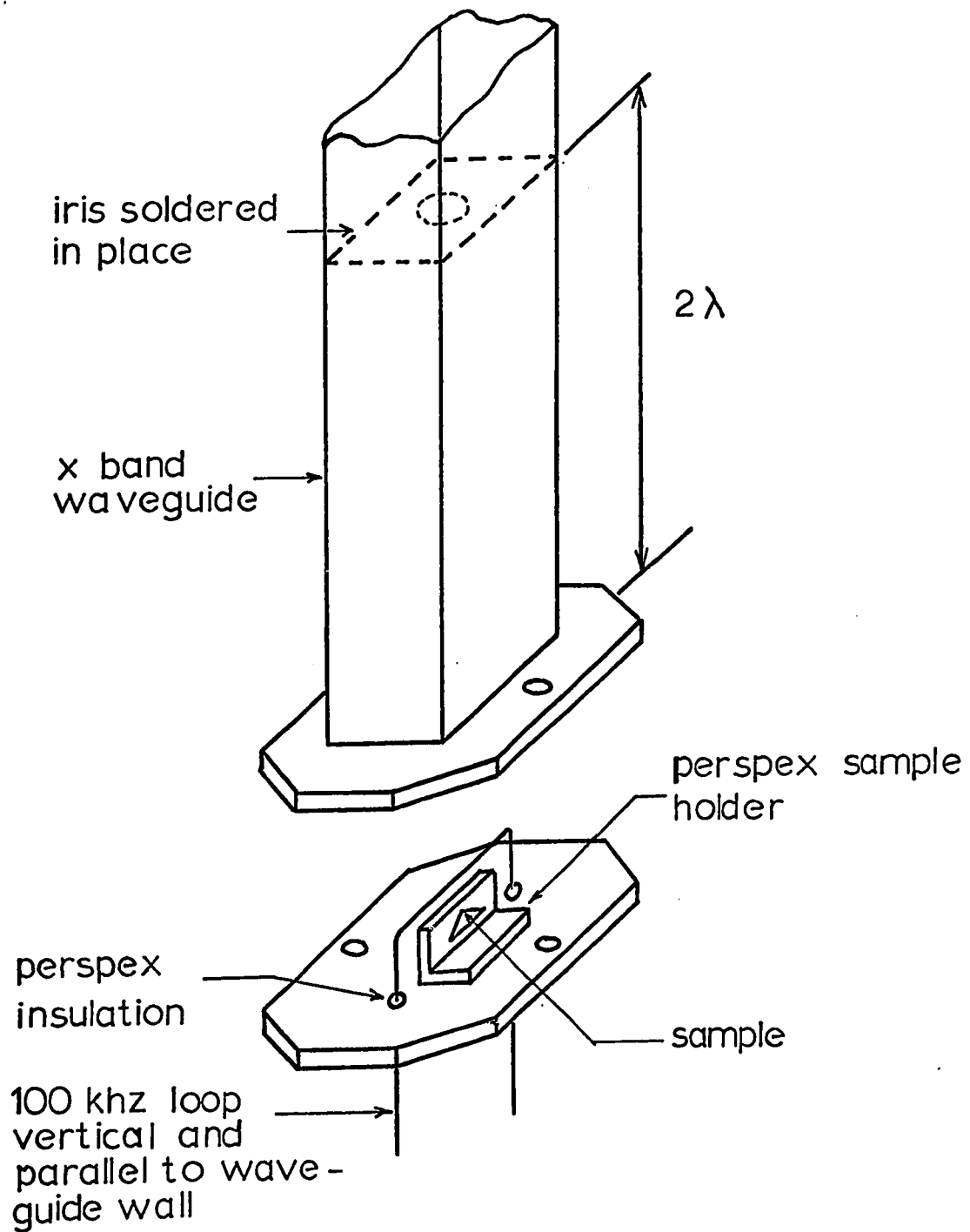


Figure 4.3 TE_{014} mode X-band cavity

mounted with the (111) face flat against a perspex sample holder which when placed within the 100 KHz loop maintained this face in vertical plane. The crystal was then rotated in this plane until one of the edges on the (111) face was vertical. This oriented the sample as shown in Figure 4.4 (b) and (c), (a) shows the crystal (111) face and the pertinent directions and planes. The perspex holder was then rotated about a vertical axis (within the 100 KHz loop) until the (111) face was normal to the external field. Rotation of the magnet base was then sufficient for angular variation studies in the (110) plane. Angles of $54^{\circ} 44'$ and $35^{\circ} 16'$ sufficed to have the magnetic field parallel to [001] and [110] directions.

Inside dimensions of the cavity are 10 mm X 23 mm X 87 mm. The unloaded Q was about 6000 and the loaded Q was about 4000. The resonant frequency was 9.276 GHz at room temperature and 9.155 GHz with the cavity immersed in liquid helium. These values varied somewhat with the actual sample and its orientation, this being due to the fact that the sample acts as a dielectric tuner over a small frequency range. In order to maintain a high Q value it is important to make the 100 KHz loop truly parallel to the wide wall of the cavity. In that case there is no microwave magnetic field component normal to the loop and consequently no energy loss from the cavity occurs due to the fact that one has a conductor in the cavity.

(ii) Cylindrical Cavity

This cavity operated in the TE_{011} mode. The microwave magnetic field at the sample is always vertical. Rotation of the magnet base would not reduce the sensitivity of the spectrometer because the external magnetic field is always normal to the microwave field. The cavity utilized a

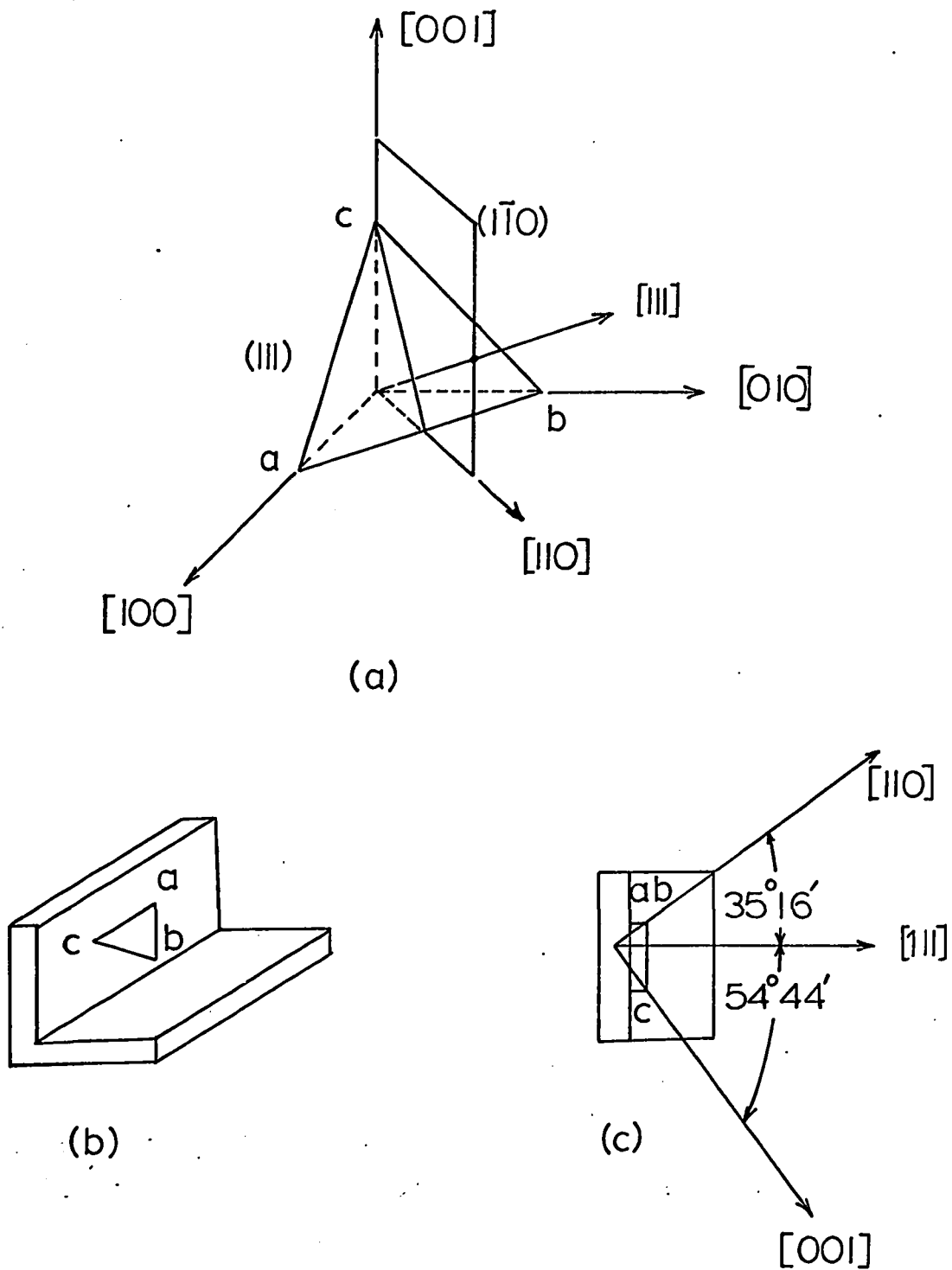


Figure 4.4 (a) Important directions and planes in the cubic system,
 (b) Crystal on sample holder,
 (c) Crystal directions.

special goniometer type sample holder. A working drawing of this goniometer is shown in Figure A1 of the appendix. With this goniometer the sample was rotated in the vertical and horizontal planes by angles θ and ϕ . These angles were plotted on a stereographic projection. This cavity was used for some preliminary ESR studies of the alums and in studying the pseudo soda alum.

E. ENDOR Cavity

This cavity is of rectangular shape and operates in the TE_{014} mode. A diagram of this system is shown in Figure 4.5. The three magnetic fields at the sample are shown in (c). This cavity was designed to resonate at liquid helium temperature at the highest klystron power mode, so that ample microwave power would be available for partial saturation of ESR absorption lines. The resonant frequency at liquid helium was 9.345 GHz. The unloaded Q was about 6000 and the loaded Q was about 4500. To obtain this value extreme care had to be taken in positioning the ENDOR coil. That is, the plane of the coil had to be truly in the $\lambda/2$ plane. The sample holder, shown in Figure 4.5 (b), had machined surfaces so that it was possible to orient the sample with the external field along [111] direction and in the (111) plane as described in part D, of this chapter.

F. Dewar System For Liquid Helium Operation

A standard two dewar system was employed. An outer evacuated wall dewar contained liquid nitrogen. An inner dewar, which was evacuated

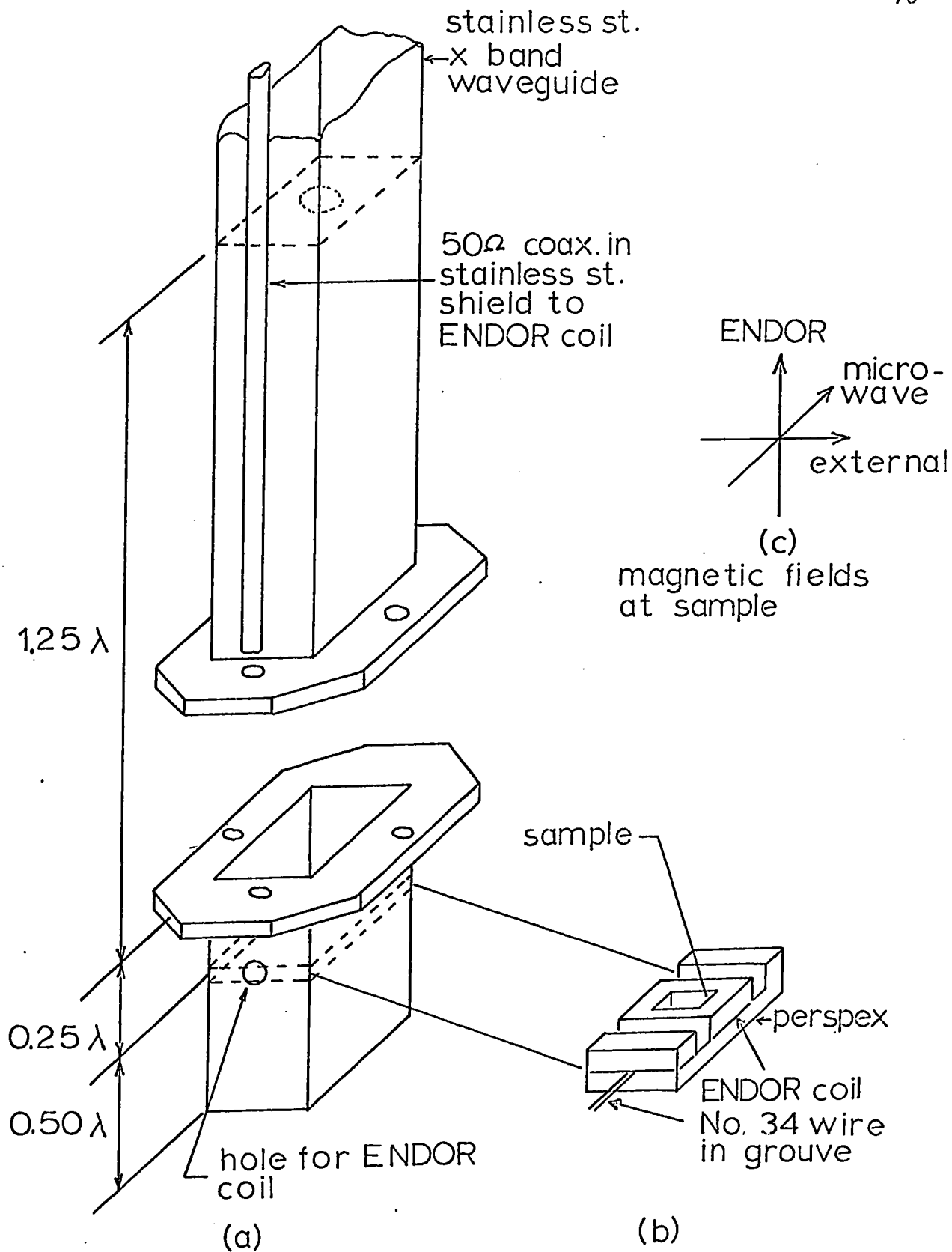


Figure 4.5 (a) ENDOR X-band cavity, (b) sample holder and ENDOR coil support
(c) Magnetic fields at sample.

before each run contained liquid helium. The stainless steel guide and brass cavity were immersed in the liquid. About 1 liter of liquid helium sufficed to fill the system, while about 2 liters were required for the actual transfer. About 6 hours of continuous operation could be obtained.

G. Magnetic Field Measurement

Nuclear magnetic resonance of hydrogen protons in water was used to measure the magnetic field at which ESR transitions occurred. For this purpose water doped with a small amount of copper sulphate was used. The nuclear absorption signal was observed on an oscilloscope, with the signal fed to the vertical input and a 60 Hz signal with a phase shifter applied to the horizontal input. The magnetic field was also modulated at 60 Hz. For a given magnetic field, the frequency applied to the coil containing the sulphate solution was varied until an absorption line appeared on the oscilloscope. The frequency at resonance was measured with a Hewlett Packard No. 52533 frequency counter. The magnetic field was calculated from the formula,

$$H \text{ (kgauss)} = \frac{\nu \text{ (MHz)}}{4.25759}$$

where, ν is the proton resonance frequency, and 4.25759 is the frequency in MHz for proton resonance at 1000 gauss.

CHAPTER V

EXPERIMENTAL PROCEDURE AND RESULTS

ESR OF $^{52}\text{Cr}^{+3}$ IN THE ALUMSI Introduction

The ESR spectra of Cr^{+3} in Rb, Cs, Na, and pseudo soda alum were analyzed at X-band microwave frequencies. Detailed analysis were carried out at room and liquid helium temperatures for the Rb and Cs alums. The Rb and Cs alums were also investigated at these temperatures in their deuterated forms. The Na and pseudo-soda alums were studied at room temperature. The work on these salts at liquid helium temperature was confined to relative intensity determination of the $M_S = \pm 3/2 \rightarrow \pm 1/2$ spectral lines in order to ascertain the signs of the zero field splitting parameters.

II The Rubidium Alums (α -type)

A The Rubidium alum grown from solution in ordinary water

(i) $^{52}\text{Cr}^{+3}$ Observations at room temperature

The ESR experimental results and analysis of the Rb alums will be presented in considerable detail. This is done with the intention of making the subsequent discussion of the other alums less repetitious.

This crystal was initially investigated using the cylindrical cavity and goniometer system of Figure A1 . This cavity system was used because it provided the maximum facility in orienting the external magnetic field along any desired crystal direction. It soon became evident that the chromium spectrum consisted of four differently oriented but otherwise equivalent complexes. Each complex consisted of three fine structure lines as is characteristic of $^{52}\text{Cr}^{+3}$ subjected to zero field splitting: some extra lines at low field were also observed and these were attributed to forbidden transitions, presumably of the $\Delta M_S = \pm 2$ type.

In general, the magnetic axes of a given complex are obtained when the fine structure lines show extrema in their separation with respect to the external magnetic field direction. This occurs when the external magnetic field points along the three mutually perpendicular axes of the crystal field tensor. One such extremum was found when the external magnetic field was along the $[111]$ direction. In this orientation the spectrum showed the greatest separation. This direction, as is

customary, was termed the z axis. Subsequent investigation revealed that the spectrum associated with this complex was axially symmetric with respect to the $[111]$ direction. That is, when the external field is anywhere on the cone defined by the $[111]$ direction and an angle θ with respect to it, the ESR spectrum for the complex in question is identical. When the external field is in a plane perpendicular to the z axis, i.e. the (111) plane, one would in the case of orthorhombic symmetry for the crystal field tensor obtain the other two extrema of the spectrum. For the case of axial symmetry, on the other hand, no angular variation of the spectrum is to be expected. This was observed experimentally to be the case to a fair degree of accuracy using the cylindrical cavity system.

The equivalence of the remaining three complexes was established by locating other z axes along the remaining $\langle 111 \rangle$ directions. This was confirmed by noting that the magnetic field values for equivalent transitions agreed to several tens of gauss. Additional evidence for equivalence of the complexes was obtained by studying the angular variation of the spectrum in the (111) plane and in the $(1\bar{1}0)$ plane. In the (111) plane, one expects the three complexes with their z axes along $[1\bar{1}1]$, $[\bar{1}11]$ and $[\bar{1}\bar{1}1]$ to be equivalent in the sense that they show similar angular variation. This follows from the cubic nature of the crystal. In the $(1\bar{1}0)$ plane, two complexes, the ones which see the $(1\bar{1}0)$ plane as a mirror plane, have their spectra superimposed. The remaining two complexes, the ones whose centers lie on the $(1\bar{1}0)$ plane, are expected

to show similar spectra. Their spectra would be displaced by

$70^{\circ} 32'$; which is the angle between the $[111]$ and the $[\bar{1}\bar{1}1]$ directions

All these relationships were observed experimentally to a reasonable degree of accuracy. For example, magnetic field positions for equivalent transitions belonging to different complexes were out at most by 20 gauss. In the $(1\bar{1}0)$ plane some separation of the spectra for the two complexes which are mirrored in the $(1\bar{1}0)$ plane was noted. These slight deviations from magnetic complex equivalence are thought to be due to imperfect alignment of the crystals in the cylindrical cavity. Orientation of the sample in this cavity depends on two angles θ , and ϕ , and it is possible to be out by as much as 2 to 4 degrees when working far from the z axis. In particular, the angular variation in the (111) plane may be out by this much. It is thought that such misalignment could easily account for above apparent complex non-equivalence. In order to verify this point, the rectangular cavity and plastic sample holder of Figure 4.4 was used. With this system, after careful alignment in the sample holder using the well developed crystal faces, angular variation in the (111) and $(1\bar{1}0)$ planes could be done by rotating the magnet base only. In this way considerable improvement in orienting the sample so that the external field is in either of the above two planes was achieved. A typical spectrum along one of the z axis is shown in Figure 5.1. The lines marked a and c in the figure are single lines, the ones marked d and e are triple, while the one marked b contains four lines. The three lines corresponding to the z axis in question are a, c, and one of b. The nine lines of the other three complexes are

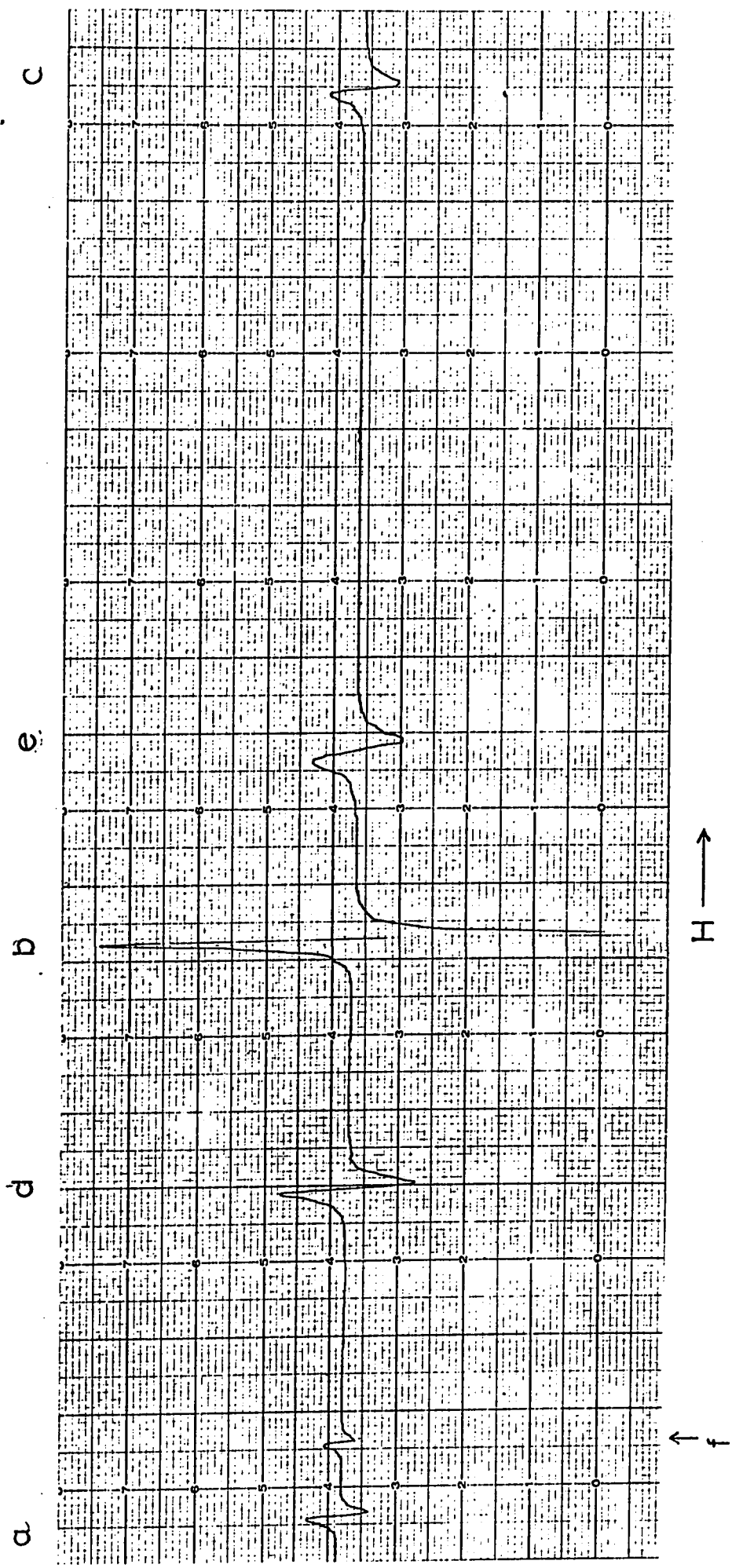


Figure 5.1 Rb(H₂O) alum Z axis at room temperature, magnetic field is along the [111] crystal direction 76

degenerate in three in this direction. Several forbidden lines were also observed. One of them appears on the chart recording.

The magnetic field values for the transitions on the z axis and in the (111) plane are given in Table 5.1. The field values on the z-axis and in the (111) were used to calculate the spin Hamiltonian parameters which also appear in the table. Shown also are the peak-to-peak line widths for transitions on the z axis. The corresponding power level in the cavity was about 15mW.

The sign of the zero field splitting, D, was determined by noting the relative intensity of the low field and high field lines at liquid helium temperature. The lines in question had equal intensities at room temperature. Careful measurement of the relative intensities of these lines at 4.2⁰K and at very low microwave power, (about 40 db down from 180 mW) using the superheterodyne spectrometer showed the high field line to be of greater intensity than the low field line. From this comparison one can conclude that the high field lines is in a lower energy state than the low field line. This implies a positive sign for the D constant. The identification of the transitions with respect to ΔM_S in Table 5.1 is based on D being positive.

Angular variation of the complete spectrum in the (111) plane is shown in Figure 5.2 the lines a, b, and c associated with the z axis spectrum are identified there. It is seen that they exhibit no angular variation in this plane as is consistent with axial symmetry of the chromium site. It is to be noted that lines a, and c now appear at high and low field respectively whereas on the z axis the opposite was

Table 5.1 ESR transition Field values and spin Hamiltonian parameters for the $\text{Rb}(\text{H}_2\text{O})$ alum at room temperature

	$H \parallel z$	$H \perp z$	ΔH_{pp} z axis
ΔM_s	Gauss	Gauss	Gauss
$3/2 \rightarrow 1/2 (H_a)$	1527.9 ± 5	4292.0 ± 5	27.3
$1/2 \rightarrow -1/2 (H_b)$	3370.4 ± 5	3191.9 ± 5	20.5
$-1/2 \rightarrow -3/2 (H_c)$	5226.6 ± 5	2515.4 ± 5	18.4
frequency	$\nu = 9.338 \pm .002 \text{GHz}$	$\nu = 9.374 \pm .002 \text{GHz}$	
$g_{\parallel} = 1.9754 \pm .005$ $g_{\perp} = 1.9675 \pm .005$ $D = +925.6 \pm 5 \text{ gauss}$			

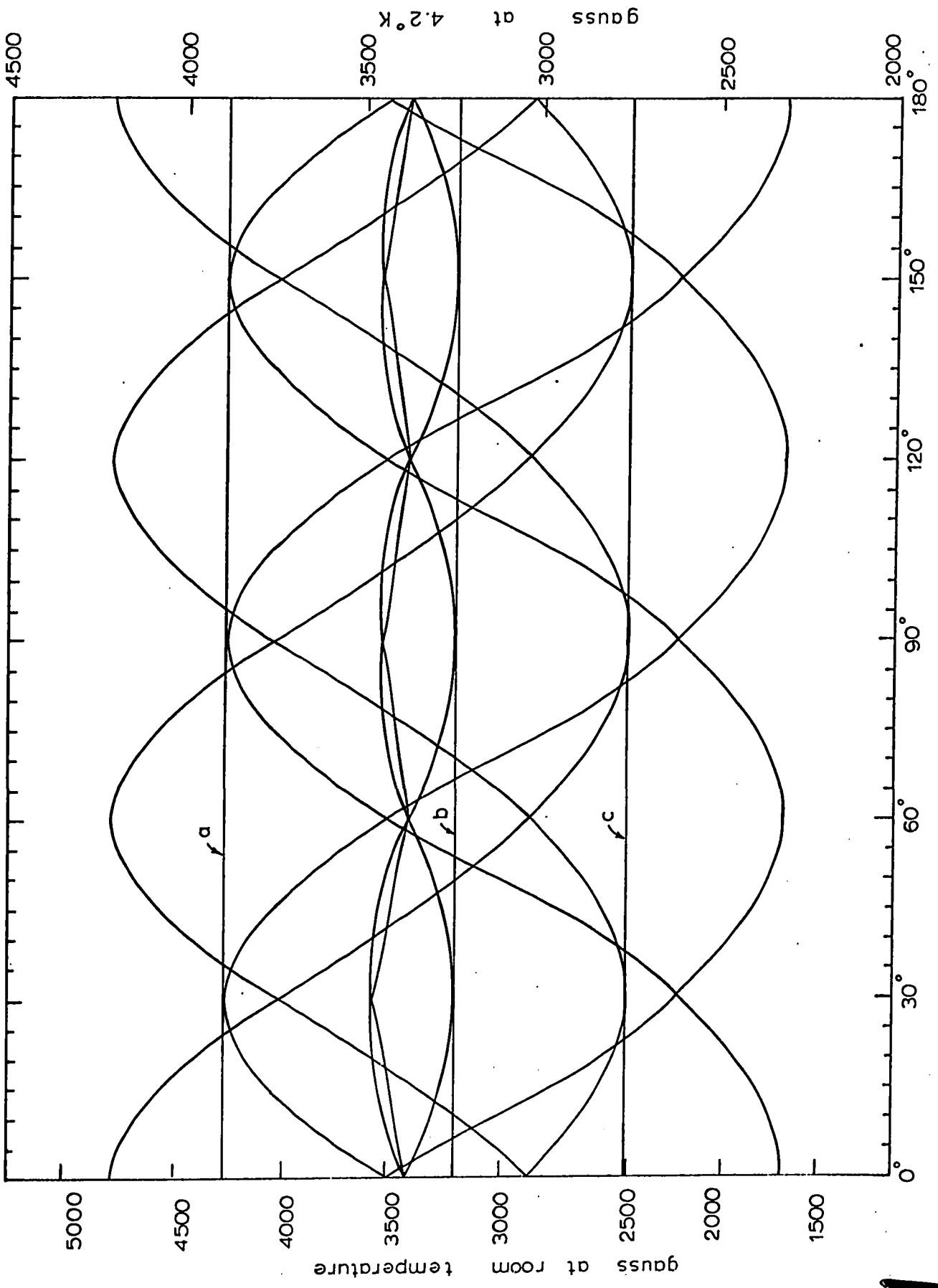


Figure 5.2 Angular variation in the (111) plane, Rb(H₂O) alum

PHYSICS DEPARTMENT, UNIVERSITY OF CALIFORNIA, BERKELEY

the case. Experimental evidence for this crossing may be seen in Figure 5.3 which shows angular variation in $(1\bar{1}0)$ plane. The remaining three complexes show their equivalence by their similar angular variation. The magnetic field values for the transitions in Figure 5.2 are presented in Table 5.2 for a range of 30 degrees. Field values for other angular orientations in this plane are not given since that can be readily obtained by constructing a mirror plane or translating the spectrum by $\pm 60^\circ$ as reference to Figure 5.2 will show. In Table 5.2 lines a, b and c, associated with the complex whose z axis is normal to (111) plane are enclosed in parenthesis. It may be seen that the variation in the magnetic field values for these lines is usually only a few gauss. This is attributed to experimental error. Only slight deviation from the (111) plane, about $1/2$ degree, would suffice to produce the observed results. Some forbidden lines at low field in this plane were observed. They were not studied other than to ascertain that they did not belong to the allowed transitions. With regard to the angular variation in Figure 5.2 the following should be pointed out. The diagram was actually drawn for the angular variation at 4.2°K on the basis of field values in Table 5.4. The room temperature scale of the diagram was adjusted so as to fit the transitions at 0° in Table 5.2.

Angular variation of the spectrum in the $(1\bar{1}0)$ plane is shown in Figure 5.3 for a range of 90° . This plane contains the $[110]$, $[111]$, and the $[\bar{1}10]$ directions. At these orientations the spectrum is particularly simple and can be used to further verify the equivalence of the complexes.

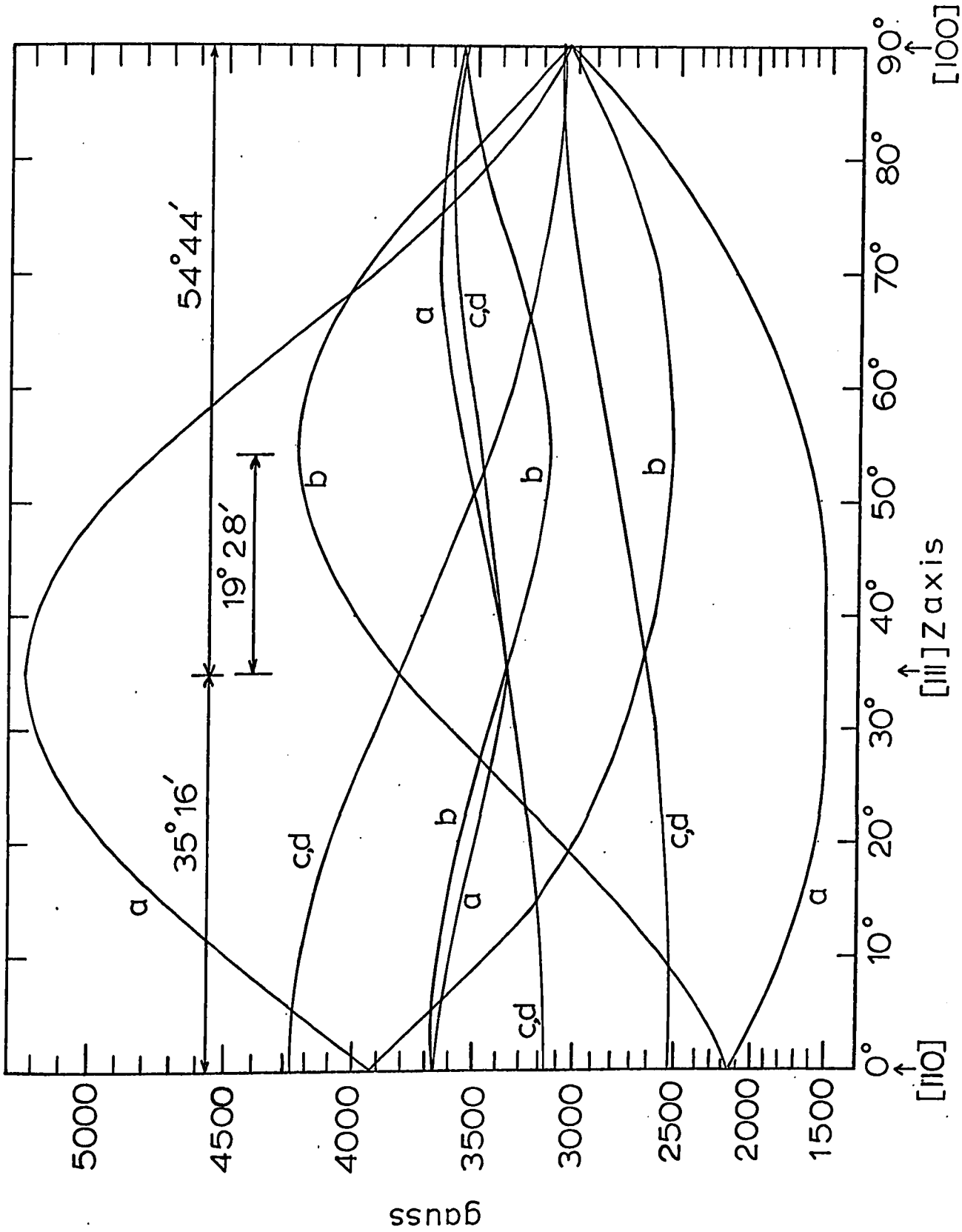


Figure 5.3 Angular variation in the (110) plane at room temperature, Rb(H₂O) alum.

Table 5.2 Field values for ESR transitions in (111) plane of the $Rb(H_2O)$ alum at room temperature

0°	5°	10°	15°	20°	25°	30°
1678.7	1716.3	1743.9	1810.8	1894.3	2004.4	2142.5
(2515.4)	(2514.6)	(2515.0)	(2516.5)	2508.9	2307.8	"
2838.1	2730.2	2648.3	2589.4	(")	(2519.2)	(2519.6)
"	2969.0	2947.8	2716.3	"	"	"
(3191.9)	(3191.4)	3132.0	(3192.6)	(3193.8)	(3199.0)	(3195.4)
3508.6	"	(3193.3)	"	3242.7	"	"
"	3439.7	3366.9	3300.9	3520.4	3658.3	3676.5
"	3561.5	3575.4	3603.4	3633.5	3684.3	"
3550.0	"	3619.3	3656.1	3677.1	"	3956.1
"	3672.3	3880.6	4059.1	4192.5	4176.2	"
(4292.0)	(4291.8)	(4290.8)	(4291.9)	(4294.4)	4268.5	(4291.1)
4780.9	4752.5	4673.1	4546.1	4375.9	(4284.9)	"

Note: All field values are in gauss. The transitions a, b and c in Figure 5.2 are in parenthesis.

The complexes in pairs are designated c and d. The complex whose z axis is along [111] is designated a and the remaining complex, with its z parallel to $[\bar{1}\bar{1}1]$ is designated b. The spectrum along [100] and [110] are shown in Figure 5.4 and Figure 5.5 respectively.

Using the constants, g_{II} , g_{\perp} , and D in Table 5.1 the matrix of the fine structure spin Hamiltonian was diagonalized for incremental values of magnetic field. This was done using an IBM 360 diagonalization subroutine and the energy level diagram for the z axis and the perpendicular direction was plotted. This is shown in Figure 5.6 .

(ii) $^{52}\text{Cr}^{+3}$ observations at liquid helium temperature.

As at room temperature, four differently oriented but otherwise equivalent complexes were observed. The z axis of the complexes were found to be along the $\langle 111 \rangle$ directions. A chart recording of the spectrum on the z axis is shown in Figure 5.7. The identification of the lines is the same as in Figure 5.1.

The magnetic field values for transitions on the z axis and in the (111) plane are given in Table 5.3. The field values and equations 3.14 were used to calculate the spin Hamiltonian parameters which also appear in the Table. Presented also are the peak to peak linewidths on the z axis. The microwave power in the cavity was about 20 db down from 15 mW. Angular variation of the spectrum in the (111) plane was studied. Figure 5.2 shows the angular variation for all four complexes. The lines a, b and c of the z axis normal to (111) are identified. The magnetic fields

The complexes in pairs are designated c and d. The complex whose z axis is along [111] is designated a and the remaining complex, with its z parallel to $[\bar{1}\bar{1}1]$ is designated b. The spectrum along [100] and [110] are shown in Figure 5.4 and Figure 5.5 respectively.

Using the constants, g_{II} , g_I , and D in Table 5.1 the matrix of the fine structure spin Hamiltonian was diagonalized for incremental values of magnetic field. This was done using an IBM 360 diagonalization subroutine and the energy level diagram for the z axis and the perpendicular direction was plotted. This is shown in Figure 5.6 .

(ii) $^{52}\text{Cr}^{+3}$ observations at liquid helium temperature.

As at room temperature, four differently oriented but otherwise equivalent complexes were observed. The z axis of the complexes were found to be along the $\langle 111 \rangle$ directions. A chart recording of the spectrum on the z axis is shown in Figure 5.7. The identification of the lines is the same as in Figure 5.1.

The magnetic field values for transitions on the z axis and in the (111) plane are given in Table 5.3. The field values and equations 3.14 were used to calculate the spin Hamiltonian parameters which also appear in the Table. Presented also are the peak to peak linewidths on the z axis. The microwave power in the cavity was about 20 db down from 15 mW. Angular variation of the spectrum in the (111) plane was studied. Figure 5.2 shows the angular variation for all four complexes. The lines a, b and c of the z axis normal to (111) are identified. The magnetic fields

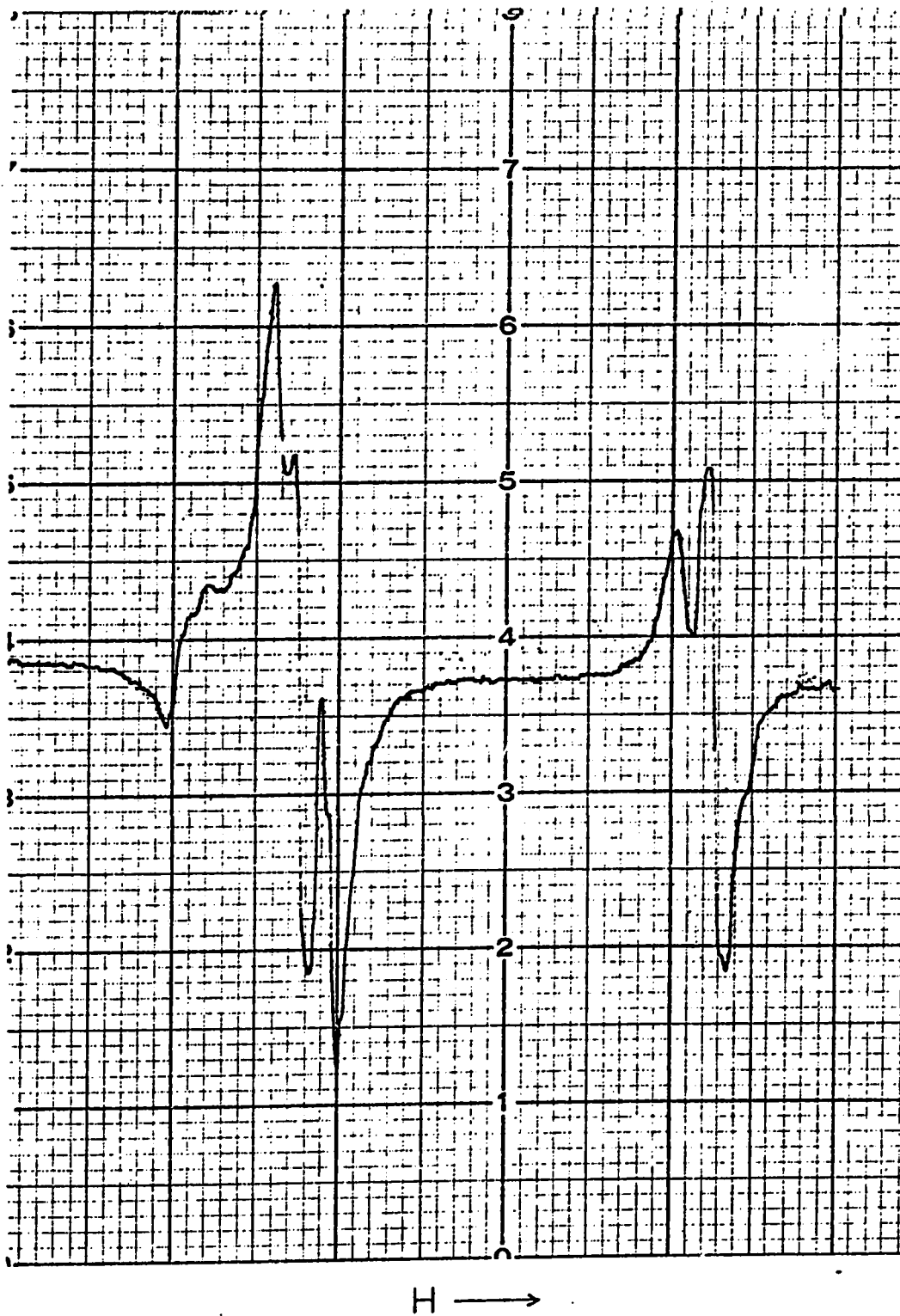


Figure 5.4 ESR spectrum at room temperature when the magnetic field is along the [001] crystal direction, $\text{Rb}(\text{H}_2\text{O})$ alum.

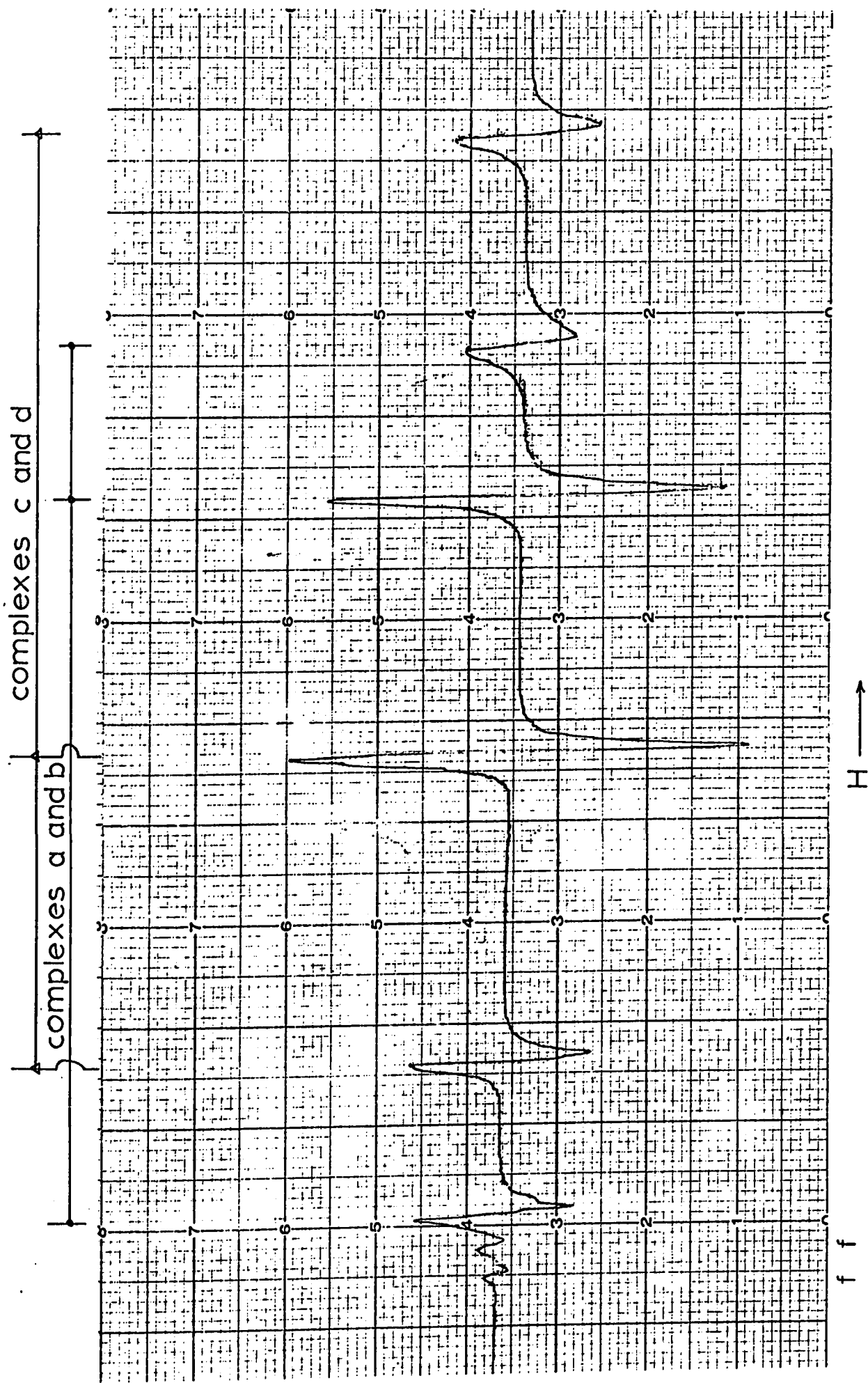


Figure 5.5 ESR spectrum at room temperature when the magnetic field is along the [110] direction, $\text{Rb}(\text{H}_2\text{O})$ alum

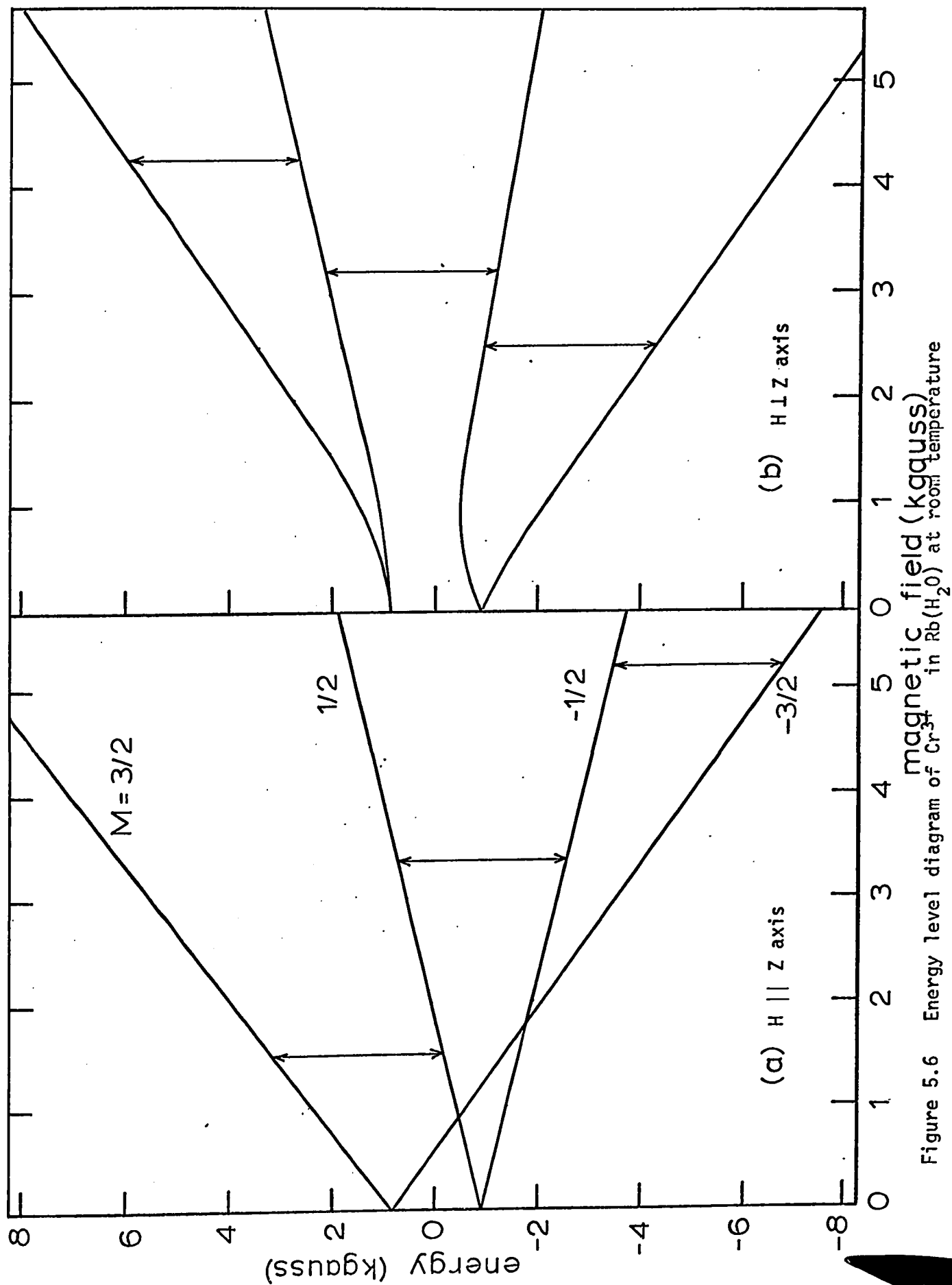


Figure 5.6 Energy level diagram of Cr^{3+} in $\text{Rb}(\text{H}_2\text{O})$ at room temperature

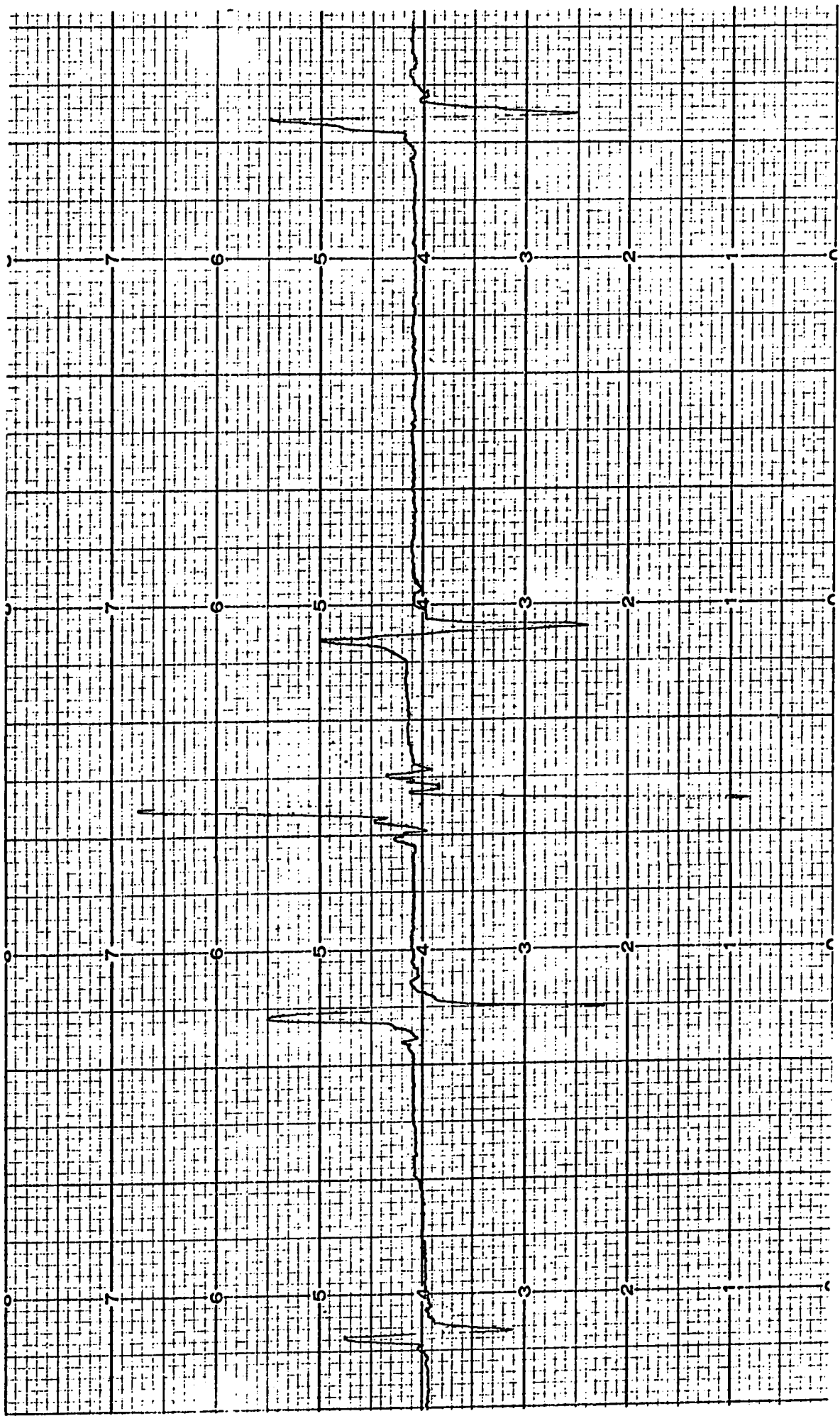


Figure 5.7 Rb(H₂O) alum Z axis at 4.2°K, magnetic field is along the [111] crystal direction identification at the lines is same as in Figure 5.1

Table 5.3 ESR transition field values and spin Hamiltonian parameters for the Rb(H₂O) alum at 4.2⁰K

	H \bar{z}	H \perp Z	ΔH_{pp} z axis
ΔM_S	gauss	gauss	gauss
$3/2 \rightarrow 1/2(H_a)$	2167.4 ± 5	3887.6 ± 5	8.8
$1/2 \rightarrow -1/2(H_b)$	3309.5 ± 5	3247.4 ± 5	16.9
$-1/2 \rightarrow -3/2(H_c)$	4454.4 ± 5	2761.5 ± 5	16.8
frequency	$9.155 \pm .002$ GHz	$9.183 \pm .002$ GHz	
$g_{II} = 1.9751 \pm .005$ $g_{\perp} = 1.9734 \pm .005$ $D = +571.9 \pm 5$ gauss			

(for a range of 30°) on which Figure 5.2 is based are given in Table 5.4. Other magnetic field values in the figure may be obtained by translation of 60° or by suitable mirror planes. The fact that lines a, b and c show no angular variation in the (111) plane indicates that the chromium ions are in sites which are axially distorted and that the distortion is trigonal since the z axis are along the $\langle 111 \rangle$ directions as was the case at room temperature. The overall features of the chromium spectrum are seen to be qualitatively the same as at room temperature. Several differences were observed, however. Firstly, the separation of the extreme spectral lines on the z axis and in other orientations is considerably reduced at 4.2°K . This is readily seen by comparing magnetic field values in Tables 5.1 & 5.3. Secondly, the absorption signal at this temperature is considerably stronger than at room temperature. For example, the spectrum in Figure 5.7 was taken at about the same gain as that in Figure 5.1 the microwave power in the cavity was about 20 db down from that at room temperature. Thirdly, Figure 5.7 shows clusters of small lines in the wings of the main transitions. These lines could be due to the hyperfine structure of chromium (53), or they could be due to chromium pair interaction as reported by Baker⁹ and Slichter⁴¹. The latter explanation is the correct one since ΔH_{pp} for the main ESR line is about 20 gauss; the wings of the absorption lines are at least as wide so the hyperfine structure is masked completely. Measurements of this separation are over 70 gauss. This fact also excludes the lines as being due to the hyperfine structure of chromium (53). These lines were in evidence only on or very close to the z axis.

Table 5.4 Field values for ESR transitions in (111) plane of the $Rb(H_2O)$ alum at $4.2^\circ K$

0°	5°	10°	15°	20°	25°	30°
2312.2	2323.9	2348.1	2393.7	2457.7	2537.7	2617.7
(2760.9)	(2762.7)	(2761.3)	(2759.3)	(2759.9)	2713.0	"
3033.9	2942.3	2878.9	2825.9	2788.5	(2761.5)	(2759.4)
"	3141.0	3117.6	2974.3	2841.1	"	"
(3248.1)	(3248.6)	(3247.7)	(3246.9)	(3246.5)	(3249.5)	(3249.8)
3377.8	3257.0	"	3286.9	3266.2	"	"
"	3344.1	3316.5	3376.7	3417.8	3432.7	3442.6
"	3386.1	3395.4	3405.8	3444.3	3447.5	"
3411.1	3403.0	3423.7	3436.9	3507.7	3646.4	3760.2
"	3551.7	3663.1	3760.5	3830.4	3366.0	"
(3888.0)	(3888.5)	(3888.9)	(3889.2)	(3888.8)	3878.6	(3889.6)
4215.4	4196.9	4151.3	4077.5	3983.2	(3892.1)	"

Note: All field values are in gauss. The transitions a, b and c in Figure 5.2 are in parenthesis

The constants g_{II} , g_I , and D in Table 5.3, were used to diagonalize the spin Hamiltonian matrix for incremental values of the magnetic field; the energy level diagrams in Figure 5.8 were thus obtained.

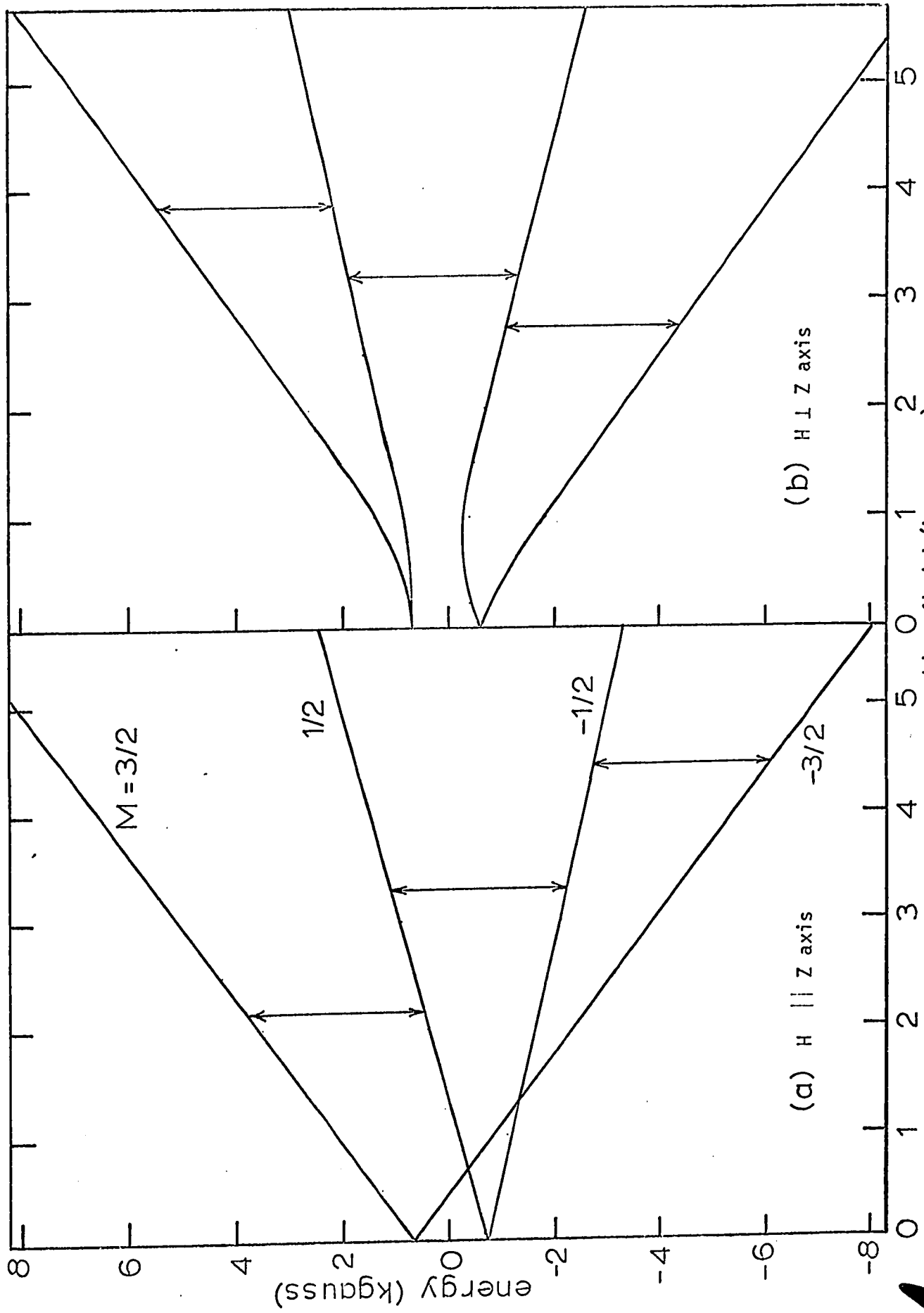


Figure 5.8 Energy level diagram of Cr³⁺ in Rb(H₂O) at 4.2°K

UNIVERSITY MICROFILMS

B. The Rubidium Alum grown from solution in heavy water.

(i) $^{52}\text{Cr}^{+3}$ observations at room temperature.

Careful study of the spectrum revealed little difference from the spectrum of the hydrated salt. Four differently oriented but otherwise equivalent complexes of chromium were found. The z axis were again determined to be along the $\langle 111 \rangle$ directions. Magnetic field values for the transitions on the z axis and in the (111) plane are given in Table 5.5. The field values and equations 3.14 were used to obtain the spin Hamiltonian constants g_{II} , g_{\perp} , and D which are also presented in the Table 5.5. The peak-to-peak linewidth for the z axis are also given.

Study of the spectrum in the (111) plane revealed no angular variation for the lines associated with the complex whose z axis is normal to the (111) plane. The remaining complexes were entirely similar in this plane. Data for a diagram of the angular variation of all the allowed spectral lines in this plane was obtained and is presented in Table 5.6 for a range of 30° . The diagram, however, is not constructed since qualitatively it would be the same as diagram of Figure 5.2. If desired, magnetic field values outside the range of 30° can be obtained by using the mirror planes and translation properties of Figure 5.2.

It was determined that the intensity of the high field line was greater than the intensity of the low field line at liquid helium temperature. This measurement established the sign of the zero field splitting parameter to be positive and the identification of ΔM_S in Table 5.5 is accordingly given.

Table 5.5 ESR transition field values and spin Hamiltonian parameters for the $\text{Rb}(\text{D}_2\text{O})$ alum at room temperature

	H Z	H \perp Z	ΔH_{pp} z axis
ΔM_S	gauss	gauss	gauss
$3/2 \rightarrow 1/2(H_a)$	1523.7 ± 5	4295.9 ± 5	32.1
$1/2 \rightarrow -1/2(H_b)$	3376.3 ± 5	3193.4 ± 5	30.3
$-1/2 \rightarrow -3/2(H_c)$	5241.6 ± 5	2516.7 ± 5	33.3
frequency	$9.353 \pm .002$ GHz	$9.372 \pm .002$ GHz	
$g_{II} = 1.9754 \pm .005$ $g_{\perp} = 1.9653 \pm .005$ $D = +930.3 \pm 5$ gauss			

Table 5.6 Field values for ESR transitions in (111) plane of the $Rb(D_2O)$ alum at room temperature.

0°	5°	10°	15°	20°	25°	30°
1789.2	1787.0	1808.9	1848.6	1919.3	2020.3	2140.6
(2516.7)	(3516.0)	(2516.5)	(2515.6)	(2506.4)	2292.6	"
2875.8	2783.6	2683.3	2610.1	"	(2520.6)	(2516.6)
"	2976.9	2924.0	2695.0	(3194.3)	"	"
(3199.6)	3168.1	(3196.6)	"	"	(3205.0)	(3193.7)
3410.8	(3198.6)	3402.6	(3196.6)	3262.8	"	"
"	3478.5	"	3331.3	3558.7	3681.3	3680.2
"	"	3616.0	3624.1	3645.3	"	"
3572.0	"	"	3662.4	3681.3	3752.1	3963.8
"	3593.8	3780.7	3981.5	4140.7	4136.2	"
(4278.0)	(4279.0)	(4285.0)	(4287.2)	(4296.7)	(4273.3)	(4297.9)
4579.4	4582.9	4536.6	4445.4	"	"	"

Note: All field values are in gauss. Transitions a, b and c are in parenthesis

(ii) $^{52}\text{Cr}^{+3}$ observations at liquid helium temperature.

As at room temperature, the four identical complexes were found to have their z axis along the $\langle 111 \rangle$ directions. The magnetic field values for the transitions on the z axis and in the (111) plane are given in Table 5.7. Presented also are the peak-to-peak linewidths on the z axis. These field values and equations 3.14, were used to calculate the spin Hamiltonian constants g_{\parallel} , g_{\perp} and D, which are also given in Table 5.7. Study of the angular variation in the (111) plane revealed no angular variation for the complex whose z axis is normal to this plane. The remaining three complexes were entirely similar. In this instance absolute magnetic field value measurements for the transitions in the (111) plane were not made other than on the lines associated with the z axis normal to (111) plane. Angular variation of the other complexes was studied by comparing chart recordings at 5° intervals and utilizing the almost linear magnetic field sweep.

As for the hydrated Rb alum at 4.2°K the absorption spectrum is over an order of magnitude stronger than at room temperature. Also, the presence of satellite lines in the wings of the main transitions was clearly discernible on the z axis.

Table 5.7 ESR transition field values and spin Hamiltonian parameters
for the $\text{Rb}(\text{D}_2\text{O})$ alum at 4.2°K

	H Z	H \perp Z	ΔH_{pp} z axis
ΔM_S	gauss	gauss	gauss
$3/2 \rightarrow 1/2$	2179.3 ± 5	3891.5 ± 5	29.5
$1/2 \rightarrow -1/2$	3310.7 ± 5	3254.2 ± 5	17.5
$-1/2 \rightarrow -3/2$	4436.2 ± 5	2775.7 ± 5	35.1
frequency	$9.167 \pm .002$ GHz	$9.187 \pm .002$ GHz	
$g_{\parallel} = 1.9799 \pm .005$ $g_{\perp} = 1.9688 \pm .005$ $D = +563.5 \pm 5$ gauss			

III The Cesium alums (β -type)

A The Cesium alum grown from solution in ordinary water

(i) $^{52}\text{Cr}^{+3}$ observations at room temperature

Four differently oriented but otherwise equivalent magnetic complexes of chromium were found. The z axes were determined to be along the $\langle 111 \rangle$ directions. Study of angular variation in the (111) plane revealed no angular variation for the transitions associated with the complex where z axis is normal to this plane. The remaining three complexes were entirely similar in this plane.

Field values for transitions on the z axis and in the (111) plane along with peak-to-peak linewidths on the z axis are presented in Table 5.8. Given also are the spin Hamiltonian parameters calculated from the field values and equations 3.14. Table 5.9 presents field values for all the allowed transitions for a range of 30° in 5 degree steps. A diagram entirely similar to that in Figure 5.2 may be constructed by applying the proper mirror planes and 60 degree translations.

The superheterodyne spectrometer was used to compare the intensity of the low and high field lines on the z axis at liquid helium temperature. It was found that the low field line was more intense than the high field line. This established the sign of the zero field splitting to be negative. The ΔM_S identification of the transitions in Table 5.8 is based on this conclusion.

Table 5.8 ESR transition field values and spin Hamiltonian parameters for the Cs(H₂O) alum at room temperature.

	H Z	H ⊥ Z	ΔH_{pp} z axis
ΔM_S	gauss	gauss	gauss
$-3/2 \rightarrow -1/2$ (H _a)	1824.5 ± 5	4164.2 ± 5	29.4
$-1/2 \rightarrow 1/2$ (H _b)	3387.6 ± 5	3254.2 ± 5	27.0
$1/2 \rightarrow 3/2$ (H _c)	4956.2 ± 5	2639.6 ± 5	23.0
frequency	9.356 ± .002 GHz	9.378 ± .002 GHz	
$g_{\parallel} = 1.9715 \pm .005$ $g_{\perp} = 1.9694 \pm .005$ $D = -783.2 \pm 5$ gauss			

Table 5.9 Field values for ESR transitions in (111) plane of the Cs(H₂O) alum at room temperature

0°	5°	10°	15°	20°	25°	30°
1957.0	1972.3	2005.0	2057.6	2136.6	2240.8	2371.8
(2639.5)	(2640.2)	(2639.8)	(2635.8)	(2646.0)	2513.5	"
2940.8	2818.5	2748.3	2692.2	"	(2637.1)	(2637.4)
"	3091.7	3045.7	2852.2	"	"	"
(3254.2)	3147.4	(3252.6)	(3249.8)	3259.6	(3252.5)	(3254.7)
3475.5	(3249.8)	"	3314.3	3563.8	"	"
"	3414.0	3360.7	3390.3	"	3600.9	3605.8
"	3500.2	3521.2	3543.1	3610.4	"	"
3545.9	3539.9	3573.4	3602.0	"	3742.1	3921.7
"	3734.8	3893.7	4021.0	4109.3	4115.2	"
(4164.1)	(4164.3)	(4163.9)	(4161.9)	(4162.8)	"	(4161.4)
4644.1	4613.7	4540.1	4430.4	4284.0	4160.2	"

Note: All field values are in gauss. Transitions a, b, and c are in parentheses.

(ii) $^{52}\text{Cr}^{+3}$ observations at liquid helium temperature

Qualitatively the chromium spectrum was found to be the same at this temperature as at room temperature. The z axis were found to be along the $\langle 111 \rangle$ directions and the transitions associated with a given z axis were found to have no angular variation in the (111) plane normal to the z axis.

Field values for transitions on the z axis and normal to it along with peak-to-peak linewidths on the z axis are presented in Table 5.10. These field values and equations 3.14 were used to calculate the spin Hamiltonian constants g_{\parallel} , g_{\perp} and D.

Angular variation in the (111) plane was studied and it was determined that the remaining three complexes were entirely similar. Field values for transitions in the (111) plane for a 30 degree range, in steps of 5 degrees, are given in Table 5.11; a diagram qualitatively the same as in Figure 5.2 may be constructed by using the mirror planes and 60 degree translations appearing there.

Table 5.10 ESR transition field values and spin Hamiltonian parameters for the Cs(H₂O) alum at 4.2⁰K

	H Z	H ⊥ Z	ΔH_{pp} z axis
ΔM_S	gauss	gauss	gauss
-3/2 → -1/2 (H _a)	1888.7 ± 5	4031.5 ± 5	27.9
-1/2 → 1/2 (H _b)	3321.2 ± 5	3207.1 ± 5	28.6
1/2 → 3/2 (H _c)	4757.6 ± 5	2628.0 ± 5	30.9
frequency	9.172 ± .002 GHz	9.192 ± .002 GHz	
$g_{II} = 1.9718 \pm .005$ $g_{\perp} = 1.9722 \pm .005$ $D = -717.4 \pm 5$ gauss			

Table 5.11 Field values for ESR transitions in (111) plane of the Cs(H₂O) alum at 4.2°K

0°	5°	10°	15°	20°	25°	30°
2009.5	2028.2	2061.5	2111.5	2189.4	2279.5	2401.0
(2628.0)	(2629.7)	(2630.3)	(2631.6)	(2638.8)	2537.5	"
2815.6	2801.7	2731.3	2683.9	"	2631.7	(2629.7)
"	3067.0	3016.5	2848.4	"	"	"
(3207.1)	(3205.6)	(3203.8)	(3204.5)	(3210.3)	(3205.6)	(3203.9)
3392.8	3343.7	3300.2	3255.7	"	"	"
"	"	"	3340.9	3475.6	3501.6	3505.9
"	3412.9	3433.9	3451.7	3514.4	"	"
3468.9	3458.9	3485.3	3502.4	"	3663.9	3823.2
"	3646.2	3790.6	3904.4	3984.5	4019.0	"
(4031.4)	(4031.4)	(4031.9)	(4030.9)	(4032.1)	(4030.6)	4025.2
4478.1)	4449.2	4380.3	4284.4	4156.3	"	"

Note All field values are in gauss. Transitions a, b and c are in parentheses.

B The cesium alums grown from solution in heavy water

(i) $^{52}\text{Cr}^{+3}$ observations at room temperature

The spectrum of the deuterated crystals was qualitatively the same as for the hydrated crystals. The z axes were again determined to be along the $\langle 111 \rangle$ directions and the spectrum for a given complex was axially symmetric with respect to its z axis. This was, as in previous instances, determined by studying the angular variation in the (111) plane.

In this case, absolute field values for the variation in the (111) plane were not measured. Angular variation was studied by utilizing the approximately linear magnetic field sweep and making sure that each sweep was started at the same field value. Essentially the same variation as in Figure 5.2 was obtained.

The magnetic field values for the transitions on the z axis and perpendicular to it along with peak-to-peak linewidths on the z axis are presented in Table 5.12. The field values on the z axis and equations 3.14 were used to calculate the spin Hamiltonian parameters g_{II} , g_{I} and D. The superheterodyne spectrometer was used to establish that the low field line was of greater intensity than the high field line on the z axis at 4.2°K . The sign of the zero field splitting parameter was thus established to be negative and the ΔM_{S} identification of the transitions in Table 5.12 is accordingly given.

Table 5.12 ESR transition field values and spin Hamiltonian parameters
for the Cs(D₂O) alum at room temperature

	H Z	H ⊥ Z	ΔH_{pp} z axis
ΔM_S	gauss	gauss	gauss
-3/2 → -1/2	1771.1 ± 5	4195.7 ± 5	12.5
-1/2 → 1/2	3384.3 ± 5	3246.0 ± 5	-
1/2 → 3/2	4996.7 ± 5	2616.1 ± 5	18.1
frequency	9.353 ± .002 GHz	9.374 ± .002 GHz	
$g_{ } = 1.9746 \pm .005$ $g_{\perp} = 1.9663 \pm .005$ $D = -806.3 \pm 5 \text{ gauss}$			

(ii) $^{52}\text{Cr}^{+3}$ observations at liquid helium temperature

The chromium spectrum of the deuterated crystals was qualitatively the same as that of the hydrated crystals at this temperature. The z axes were found to be along the $\langle 111 \rangle$ directions and the spectrum of each complex was axially symmetric with respect to its z axis. This was verified by studying the angular variation in the (111) plane. As at room temperature, the almost linear magnetic field sweep was utilized to obtain the angular variation. This variation was established to be qualitatively the same as in all previous cases.

Magnetic field values for transitions on the z axis and in the (111) plane are presented in Table 5.13 along with peak-to-peak linewidths on the z axis. These field values and equations 3.14 were used to calculate the spin Hamiltonian constants g_{\parallel} , g_{\perp} and D.

Table 5.13 ESR transition field values and spin Hamiltonian parameters for the Cs(D₂O) alum at 4.2°K.

	H Z	H ⊥ Z	ΔH_{pp} z axis
ΔM_S	gauss	gauss	gauss
-3/2 → -1/2	1821.0 ± 5	4068.4 ± 5	20.4
-1/2 → 1/2	3318.7 ± 5	3196.2 ± 5	-
1/2 → 3/2	4812.8 ± 5	2598.7 ± 5	18.6
frequency	9.168 ± .002 GHz	9.190 ± .002 GHz	
$g_{ } = 1.9747 \pm .005$ $g_{\perp} = 1.9696 \pm .005$ $D = -747.7 \pm 5$ gauss			

IV The Soda Alum (γ - type)

This crystal was studied at room temperature. Four differently oriented but otherwise equivalent chromium complexes were found. The z axes were found to along the $\langle 111 \rangle$ directions. A chart recording of the z axis is shown in Figure 5.9. The spectrum of each complex was axially symmetric with respect to its z axis. This was confirmed by studying the angular variation in the (111) plane. Comparison of spectra taken at 5° intervals in the (111) plane showed that the three complexes were entirely the same. The three lines associated with the complex whose z axis is normal to the (111) plane had no angular variation. Figure 5.10 show the angular variation of the ESR lines in the (111) plane.

The sign of the zero field splitting parameter was obtained by comparing the relative intensities of the low field and high field lines at 4.2°K using the superheterodyne spectrometer. This information was not easy to obtain for the soda alum because the crystal seemed to crack at low temperature and each line, which was single at room temperature appeared as a group of lines at low temperature. Nevertheless, by using low power level in the resonant cavity so as not to saturate the lines, it was determined that the ratio of the average line intensity in the low field group to that of the high field group increased at low temperature. This means that the low field line must be a $M_S = -3/2 \rightarrow -1/2$ transition. Field positions and spin Hamiltonian parameters on the z axis and normal to it are presented in Table 5.14, along with spin Hamiltonian

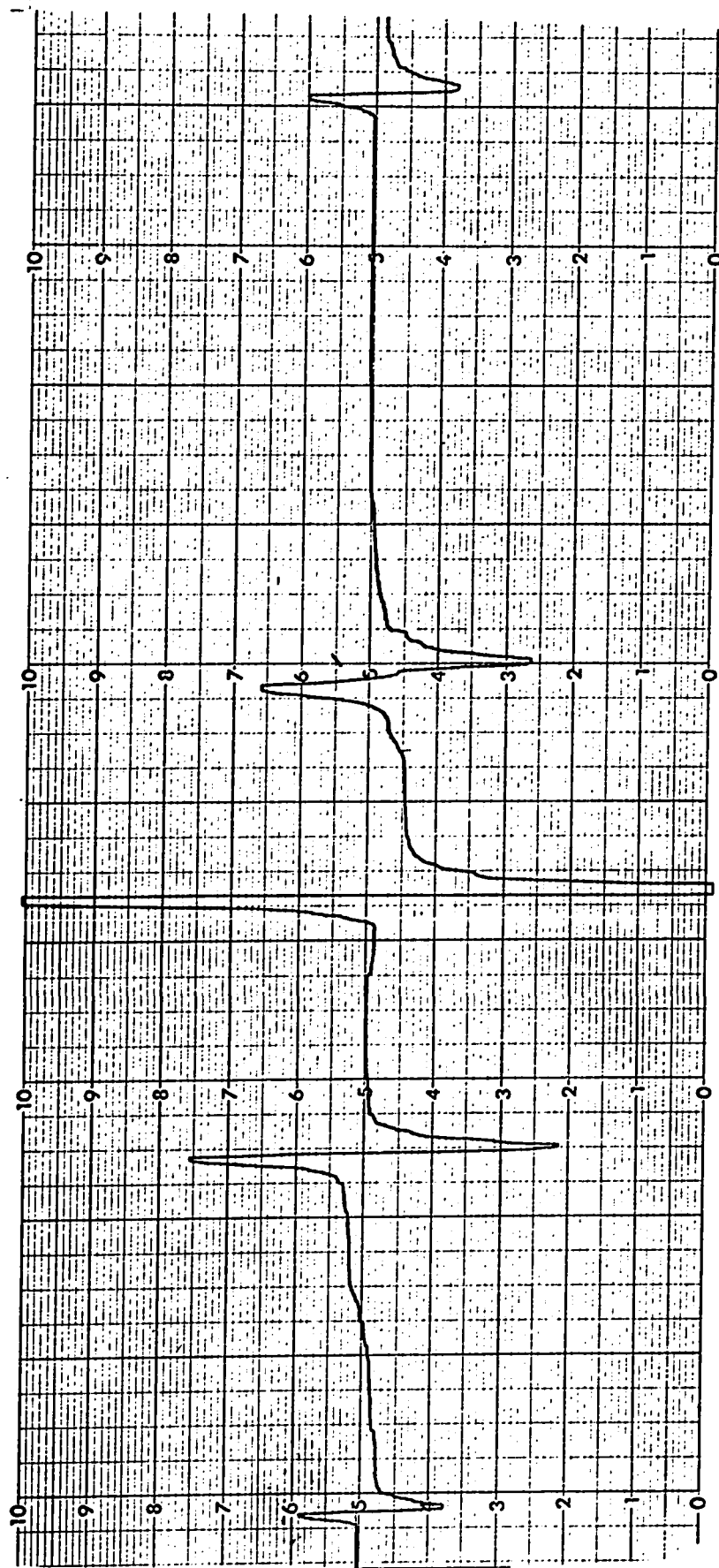


Figure 5.9 Soda alum Z axis at room temperature, magnetic field is along [111] crystal direction.

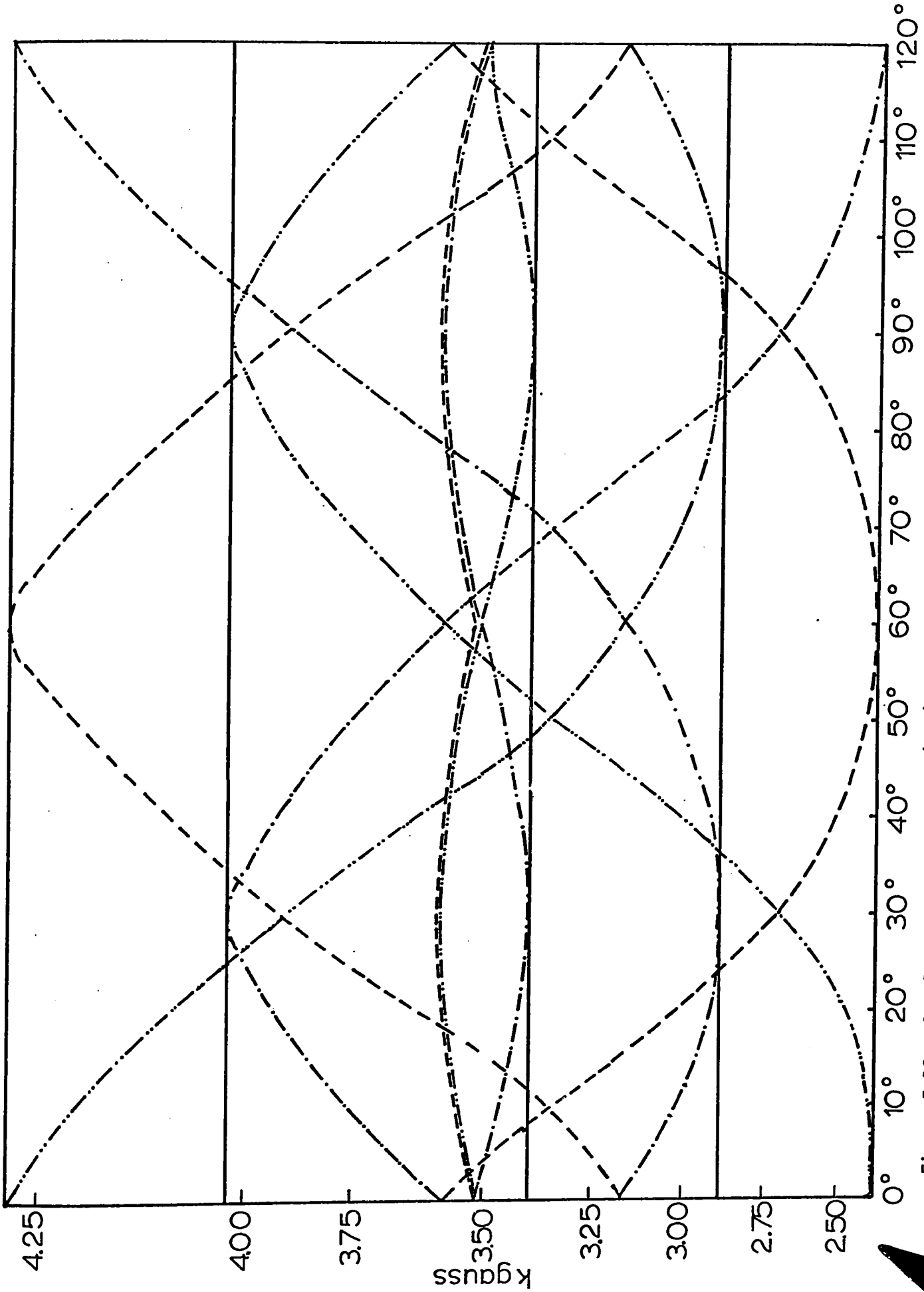


Figure 5.10 Angular variation in the (111) plane at room temperature, Soda alum.

Table 5.14 ESR transition field values and spin Hamiltonian parameters
for the soda alum at room temperature

	H Z	H ⊥ Z
ΔM_S	gauss	gauss
$-3/2 \rightarrow -1/2$	2230.3 ± 5	4046.1 ± 5
$-1/2 \rightarrow 1/2$	3443.2 ± 5	3361.0 ± 5
$1/2 \rightarrow 3/2$	4668.6 ± 5	2848.9 ± 5
frequency	$9.525 \pm .002$ GHz	$9.525 \pm .002$ GHz
$g_{\parallel} = 1.9733 \pm .005$ $g_{\perp} = 1.9747 \pm .005$ $D = -303.8 \pm 5$ gauss		

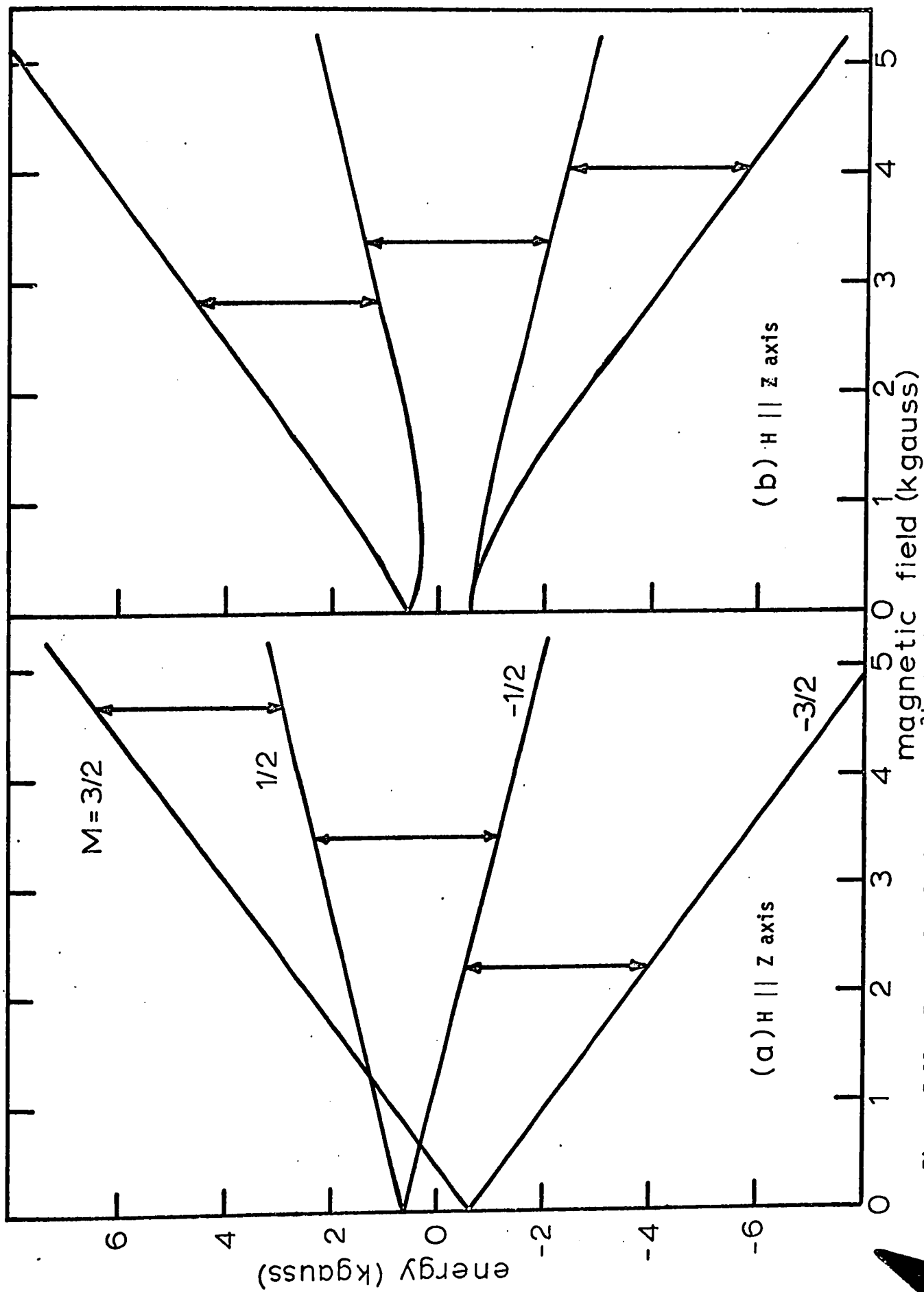


Figure 5.11 Energy level diagram of Cr^{3+} in the Soda alum at room temperature

parameters calculated by using these values and equations 3.14 . The energy level diagram for the soda alum based on these parameters is shown in Figure 5.11. The diagram reflects the negative sign of the zero field splitting parameter D. The spin Hamiltonian parameters for the Rb, Cs and Na alums are collected together in Table 5.15.

V The Pseudo Soda Alum

This crystal was also found to give up its water of crystallization readily and would disintegrate within several hours. Several coats of varnish were sprayed on the crystals and this procedure increased their lifetime to several weeks.

The crystal was investigated using the cylindrical cavity system of Figure A1 . The ESR spectrum consisted of six lines in two groups of three, plus some forbidden lines at low values of magnetic field. Each group of lines showed an identical angular variation of its line positions when the magnetic field direction was varied in the xy, yz, and xz planes of the magnetic complex. A chart recording along a typical z axis is given in Fig.5.12. In this figure all the lines are single except the one marked c, which is double. The lines corresponding to the z axis in question are those marked a, e, and one of c. The angular variations of the lines in one group between their x, y, and z magnetic axes are shown in Figure 5.13 as solid lines. The dotted lines indicate the consequent variation in position of the remaining three lines. The positions of the magnetic axes, in conjunction with the crystallographic directions, are shown in the

Table 5.15 Spin Hamiltonian parameters for the Rb, Cs and Na alums.

			Rb alum α type	Cs alum β type	Na Alum γ type
HYDRATED	Room Temp.	g_{II}	1.9754	1.9715	1.9733
		g	1.9675	1.9694	1.9745
		D	+ 925.6 gauss	- 783.2 gauss	-609.5 gauss
	4.2°K	g_{II}	1.9751	1.9718	
		g	1.9734	1.9722	
		D	+ 571.9 gauss	- 717.4 gauss	
DEUTERATED	Room Temp.	g_{II}	1.9754	1.9746	
		g	1.9653	1.9663	
		D	+ 930.3 gauss	- 806.3 gauss	
	4.2°K	g_{II}	1.9799	1.9747	
		g	1.9688	1.9696	
		D	+ 563.9 gauss	- 747.7 gauss	

Note All g values are $\pm .005$ and D values are ± 5 gauss

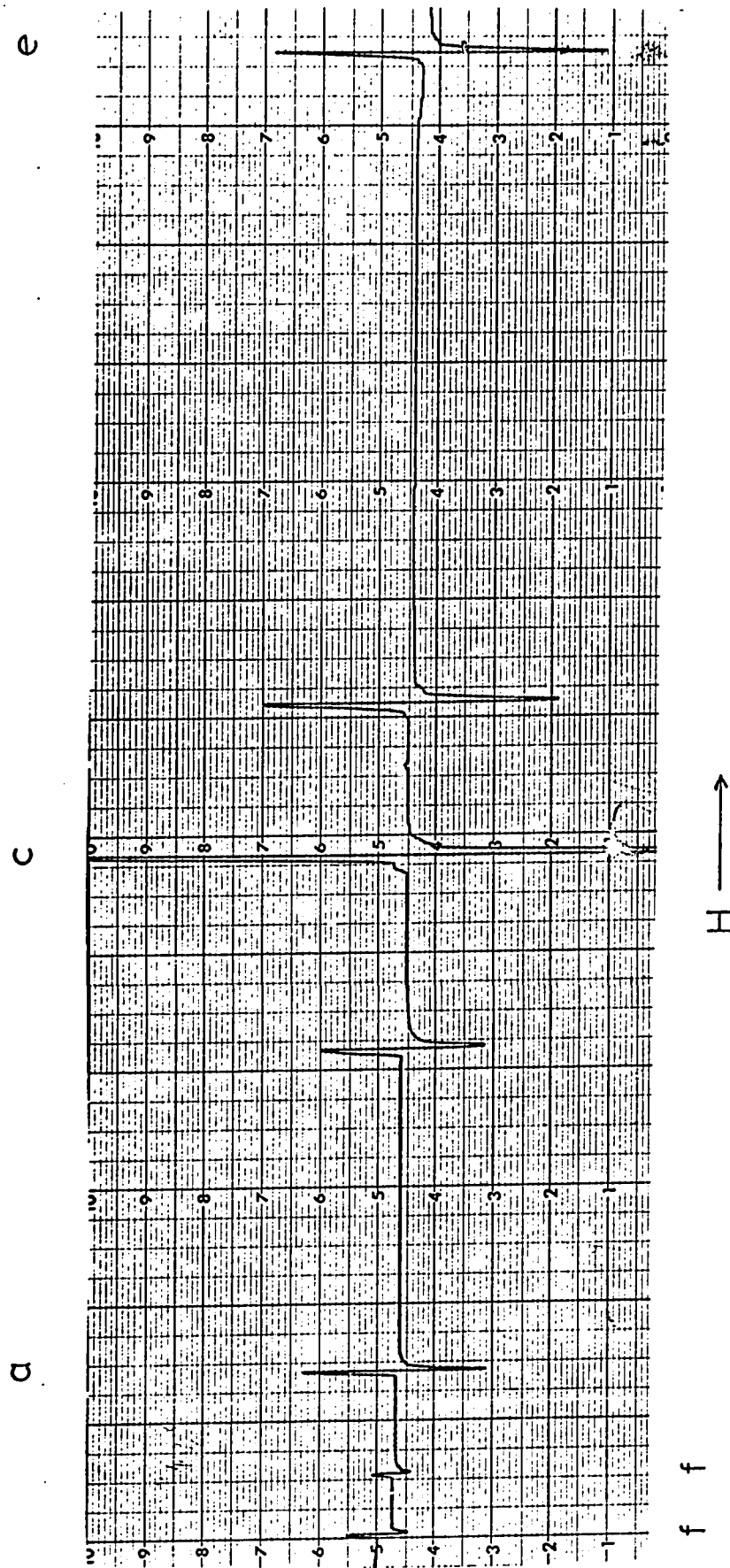


Figure 5.12 Pseudo soda alum Z axis at room temperature

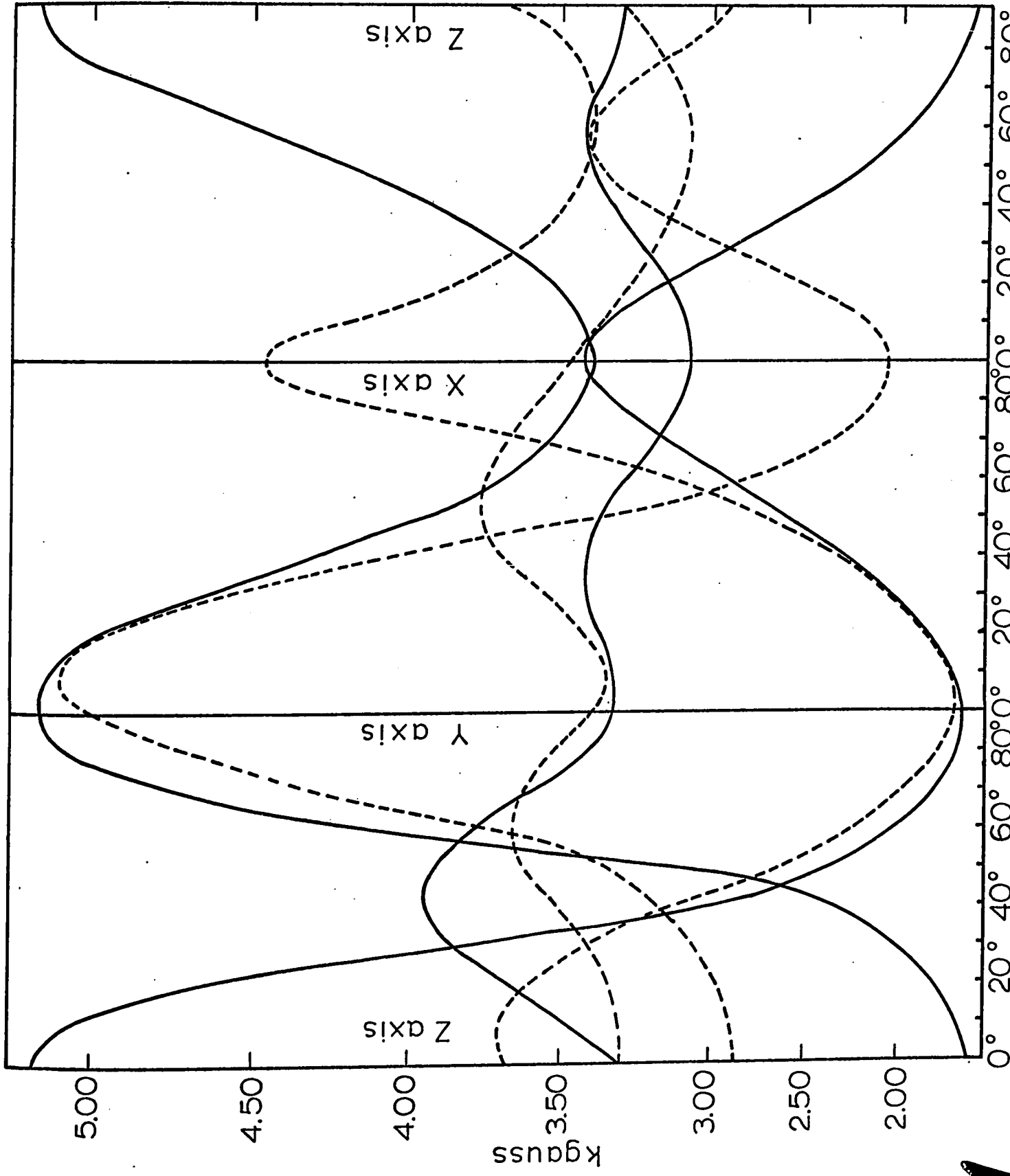


Figure 5.13 Angular variation in the ZY, YX and XZ planes in the pseudo soda alum at room temperature

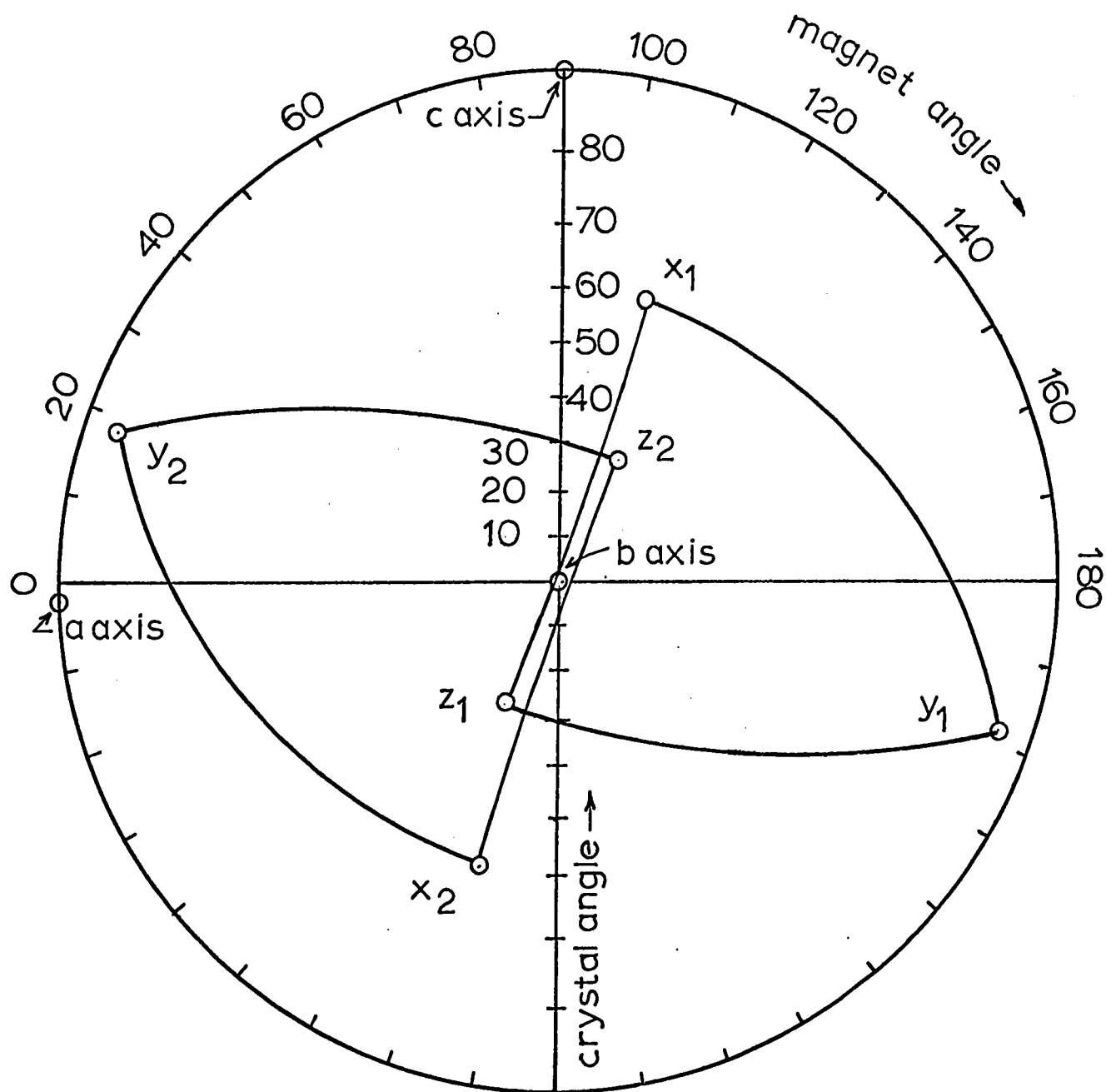


Figure 5.14 Stereographic projection of the crystal and magnetic axes in the pseudo soda alum at room temperature.

stereographic plot of Figure 5.14. When the magnetic field direction was varied in the a-c plane the two complexes appeared as one, indicating that the complexes had twofold symmetry with respect to the monoclinic b axis. The three axes of one complex are derived from those of the other by reflection in the a-c plane. The above results indicate that there are two differently oriented, but otherwise equivalent, chromium complexes in pseudo soda alum. The following angular relationships are obtained from the stereogram between the magnetic and crystallographic axes:

$$\begin{bmatrix} X_1 \\ Y_1 \\ Z_1 \end{bmatrix} = \begin{bmatrix} -\sin 30^\circ & \sin 4^\circ & \cos 30^\circ \\ \sin 4^\circ & \cos 4^\circ & \sin 4^\circ \\ \cos 30^\circ & \sin 4^\circ & \sin 30^\circ \end{bmatrix} \begin{bmatrix} X_2 \\ Y_2 \\ Z_2 \end{bmatrix}$$

$$\begin{bmatrix} X_1 \\ Y_1 \\ Z_1 \end{bmatrix} = \begin{bmatrix} -\sin 16^\circ & \sin 30^\circ & \cos 34^\circ \\ -\cos 23^\circ & \sin 2^\circ & -\sin 20^\circ \\ \sin 14^\circ & \cos 30^\circ & -\sin 26^\circ \end{bmatrix} \begin{bmatrix} a \\ b \\ c \end{bmatrix}$$

All the angles have an accuracy of $\pm 2^\circ$

Since the two complexes are identical magnetic field measurements of the line positions were made along the z, y, and x axis of only one complex. The values are given in Table 5.16. Using these field values and equations 3.14 the parameters for a spin Hamiltonian of orthorhombic symmetry were calculated.

Table 5.16 ESR transition field values and spin Hamiltonian parameters for the pseudo-soda alum at room temperature.

ΔM_S	H Z gauss	H Y gauss	H X gauss
$-3/2 \rightarrow -1/2$	1594 ± 1	5448 ± 1	3431 ± 1
$-1/2 \rightarrow 1/2$	3336 ± 1	3329 ± 1	3000 ± 1
$1/2 \rightarrow 3/2$	5455 ± 1	1607 ± 1	3457 ± 1
Microwave frequency = $9.523 \pm .003$ GHz			

g_z	$1.975 \pm .002$
g_y	$1.966 \pm .005$
g_x	$1.980 \pm .003$
D	-1008.0 ± 5 gauss
E	-345.0 ± 5 gauss

The sign of the constant D was found in the same way as for the soda alum. In the present case, however, the crystals did not crack. The spin Hamiltonian of rhombic symmetry was diagonalized for incremental values of magnetic field. The constants in Table 5.16 were used and energy level diagrams for the Z, Y, and X axis were obtained. These are shown in Figure 5.15.

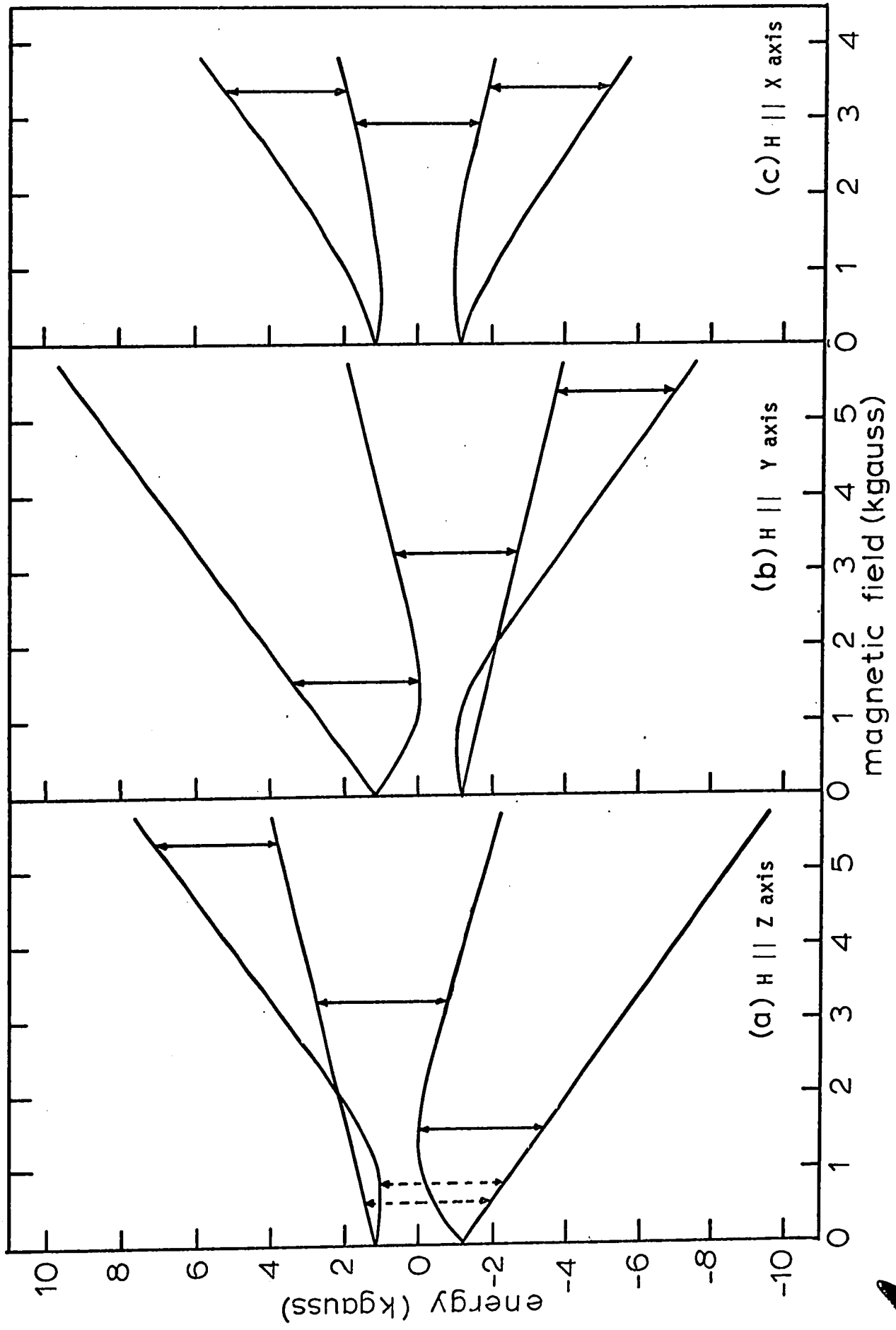


Figure 5.15 Energy level diagram of Cr³⁺ in the pseudo soda alum at room temperature

CHAPTER VI

EXPERIMENTAL PROCEDURE AND RESULTS

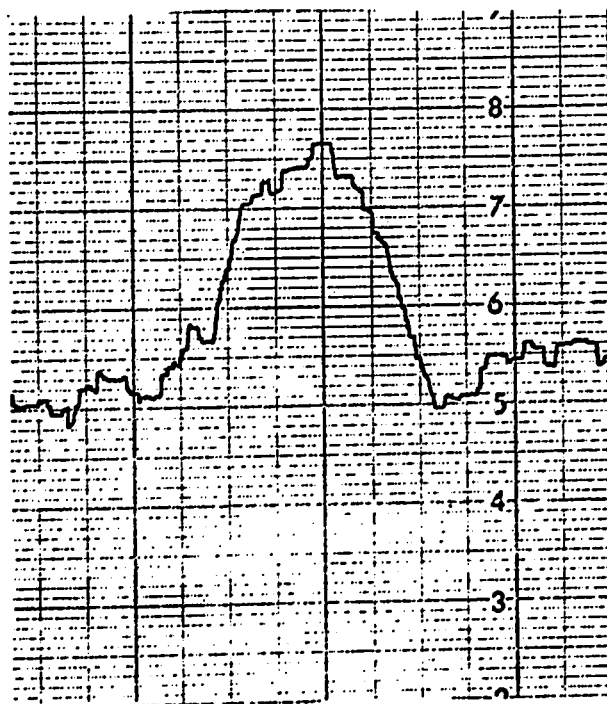
ENDOR OF $^{53}\text{Cr}^{+3}$ IN THE Rb AND Cs ALUMS

I The Rubidium alum

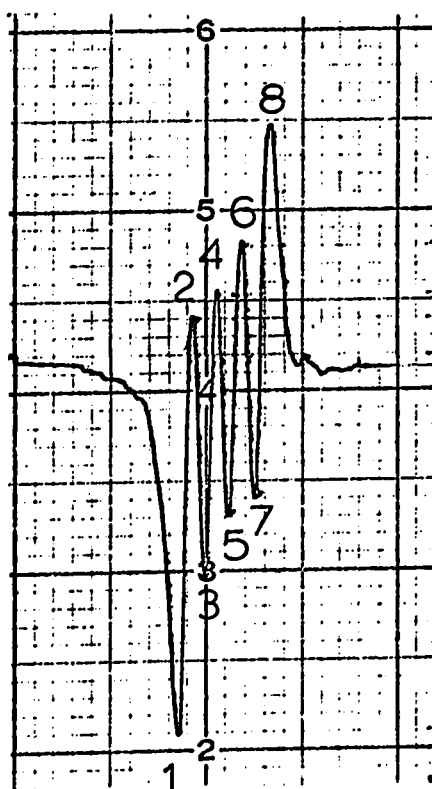
A Crystals grown from solution in ordinary water

The experimental procedure and analysis of data for this crystal will be presented in detail. In the subsequent discussion of the other alums points explicitly not made but which are discussed in this section may be taken to apply there as well.

Initially, the crystals doped with Chromium (53) had unresolved hyperfine structure. This was thought to be due to concentration broadening. After successive dilution with Rb_2SO_4 plus $\text{Ga}_2(\text{SO}_4)_3$ a point was reached where no enhancement in the resolution of the hyperfine structure was obtained. The ENDOR measurements were made on such crystals. Figure 6.1 (a) shows the $\Delta M_s = -3/2 \rightarrow -1/2$ transition at room temperature, (power level in the cavity was - 40 db from 150 mW \approx .015 mW). Part (b) of the figure shows the same line at liquid helium temperature, with the hyperfine structure being nearly resolved. Power level in the cavity was about - 20 db from 15 mW \approx .15 mW). No trace of the even isotope of chromium is evident in this spectrum. The hyperfine structure associated with the $M_s = \pm 3/2 \rightarrow \pm 1/2$ transitions on the z axis were centered on or very close to the field values found for these transitions for the even isotope.



(a) Room temperature



(b) 4.2°K

Figure 6.1 ESR spectrum of $^{53}\text{Cr}^{3+}$ ($\Delta M = -3/2 \rightarrow -1/2$) line in the $\text{Rb}(\text{H}_2\text{O})$ alum

Presented in Table 6.1 are the field values for the points on the spectrum indicated in Figure 6.1(b). An approximate attempt at resolution of the hyperfine spectrum shows the peak-to-peak linewidths to be about 9.5 gauss. To first order, line separation is about $A/g\beta = 18$ gauss. From these values one expects an overlap of several gauss for the hyperfine lines and this is indicated by the spectrum.

The positive sign for the zero field splitting for this alum was confirmed by establishing that the high field set of hyperfine lines was more intense than the low field set. This finding is consistent with the result for the even isotope in the Rb alums. The generally used procedure in obtaining and measuring ENDOR transitions was as follows. The ESR spectrum, such as in Figure 6.1(b) for example, was first obtained. This was done at sufficiently low power so as not to saturate the signal and thereby distort the line shape. The usual power level was 40 db down from 200 mW (~ 0.02 mW). A particular ESR transition, the first line at H_1 say, in Figure 6.1(b) was selected and the magnetic field was adjusted to the centerline position as well as one could estimate it. The microwave power was then turned up to about 2 mW thereby partially saturating the EPR transition. The magnetic field modulation was turned off and a frequency modulated (at 200 Hz), slowly swept signal, was applied to the ENDOR coil. The frequency sweep rate was about 1 MHz per minute and the frequency range swept was from 20 to 30 MHz and from 70 to 80 MHz. The PSD time constant was 1 or 3 seconds. The FM deviation was 25 KHz or 75 KHz. After the ENDOR signal was obtained the magnetic field was adjusted slightly so as to make the signal strongest. This was in effect a fairly sensitive way

Table 6.1 MAGNETIC FIELD VALUES FOR POINTS INDICATED IN
 THE SPECTRUM OF FIGURE 6.1 (b).

Point	field/gauss	diff./gauss
1	4481.1	-- 11.5
2	4492.6	8.3
3	4500.9	9.6
4	4510.5	9.2
5	4519.7	9.7
6	4529.4	9.8
7	4539.2	8.7
8	4547.9	

(to several gauss) of setting the field at H , the centerline of the the ESR line in question. Microwave power level was then varied (± 10 db) so as to optimise the signal once again. Frequency measurements were made by setting the signal generator manually at the center of the ENDOR transition; the FM modulation was turned off and the frequency was read on an HP digital counter to the nearest 100 Hz. In this manner, ENDOR measurements at the centerline position of each hyperfine line, designated H_1 , H_2 , H_3 , and H_4 , were made.

ENDOR spectra with the signal generator sweeping in the 25MHz and 75 MHz range were observed. In the 25 MHz range the frequencies measured were to within the precision of the measurements exactly 1/3 of the ENDOR frequencies measured in the 75 MHz range. The ENDOR transitions observed at 25 MHz, therefore, are not to be associated with transitions between hyperfine levels in the $M_S = \pm 1/2$ multiplets. A probable explanation of these transitions is as follows. It is known that the signal generator used had second and higher order harmonic distortion. The 25MHz sine wave had slight but visually discernible departure from a pure sine wave shape. It is concluded that possibly the wide band amplifiers following the signal generator sufficiently amplified the third harmonic to produce ENDOR transitions at 75 MHz. Experiments were also performed with a signal generator where no distortion of the 25 MHz output from a sine wave was visually evident and where the second and higher harmonics were specified to be 50 db down from the carrier. ENDOR signals at 25 MHz were observed which were also related to the 75 MHz via the third harmonic lines as before.

It, seems therefore, that the frequency modulation employed distorted the signal generator output so as to create 3rd harmonics of sufficient power so that they could, after amplification, promote ENDOR transitions in the 75 MHz range. One of these two possibilities is believed to be the explanation for the coincidence of the third harmonic of the 25 MHz lines with the 75 MHz lines. Neither of these, however, explains why the other "genuine" ENDOR transitions in the 25 MHz range were not observed since there was ample power in the first harmonic of the signal generator. Many attempts were made to detect the "genuine" 25 MHz lines. Experimental conditions such as microwave power level, sweep rate, modulation deviation, were varied. None of these combinations proved successful in obtaining transitions in the 25 MHz range which could not via the third harmonic be related to the transitions obtained at 75 MHz range. This negative result is essentially unexplained. It does not, however, preclude the determination of the spin Hamiltonian constants and their signs. ENDOR measurements in the $M_S = \pm 3/2$ multiplets yield sufficient data for this purpose.

Typical chart recordings of the ENDOR spectra in the 75 MHz range and with the magnetic field set successively on the four hyperfine lines of the $M_S = 3/2$ multiplet are shown in Figure 6.2. The lines comprising the spectra in this figure can be classified in three groups. This is illustrated in Figure 6.3. ENDOR transitions labelled with one subscript, termed direct transitions in this work, are ones between the energy level on which the relevant ESR transition terminates and the next nearest nuclear level that produces the most intense ENDOR transition. The

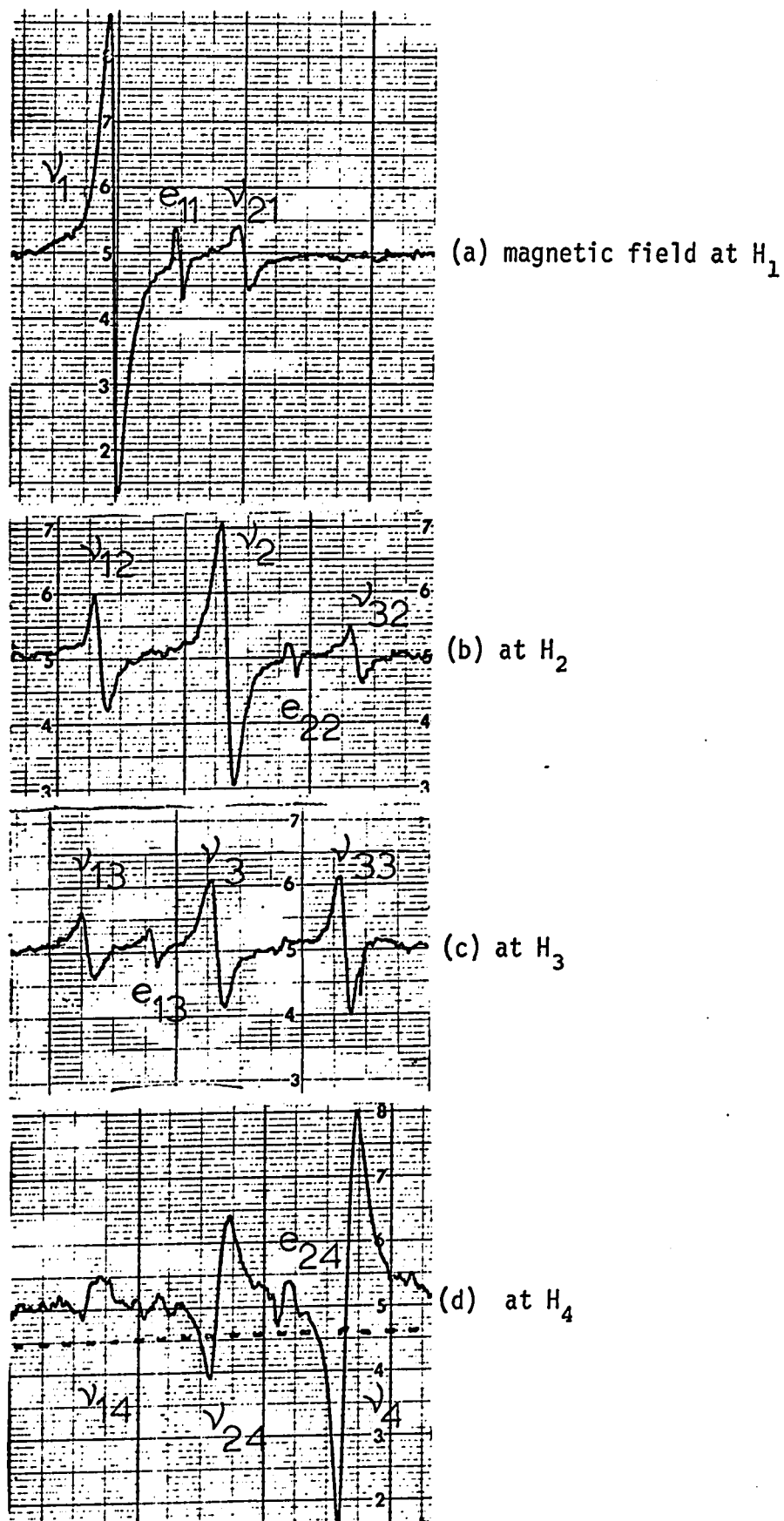


Figure 6.2 ENDOR spectra of $^{53}\text{Cr}^{3+}$ of the $M_s = 3/2$ multiplet in the $\text{Rb}(\text{H}_2\text{O})$ alum at 4.20K

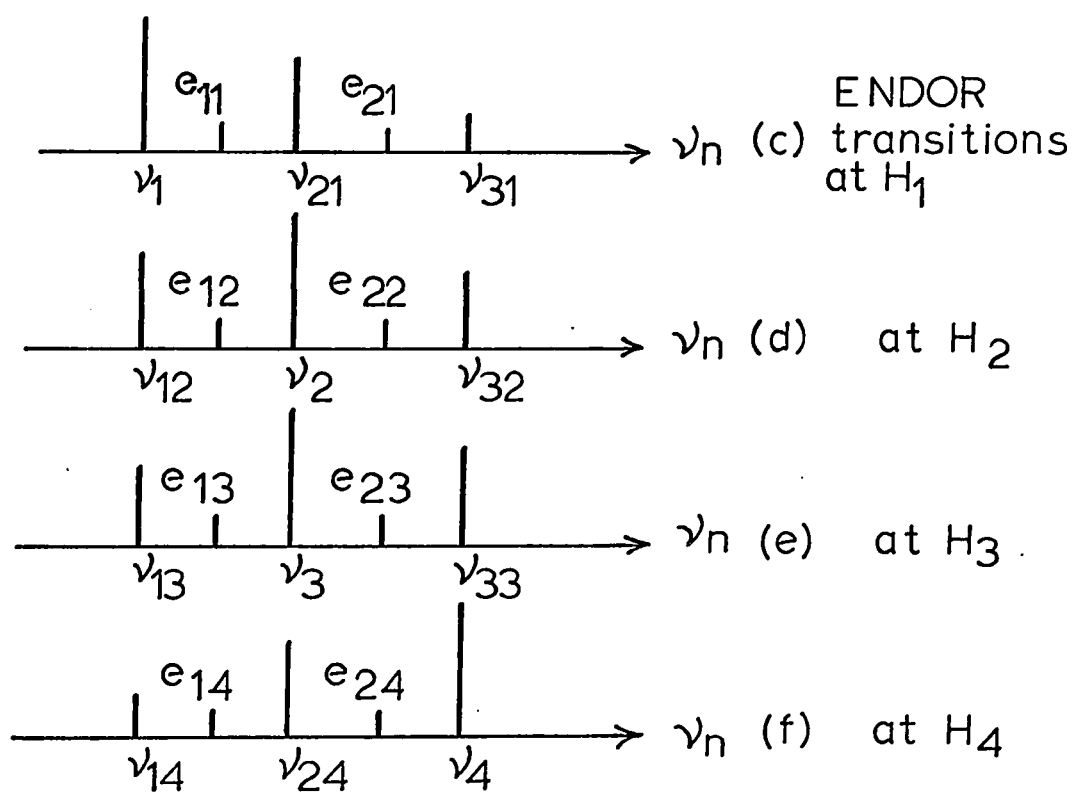
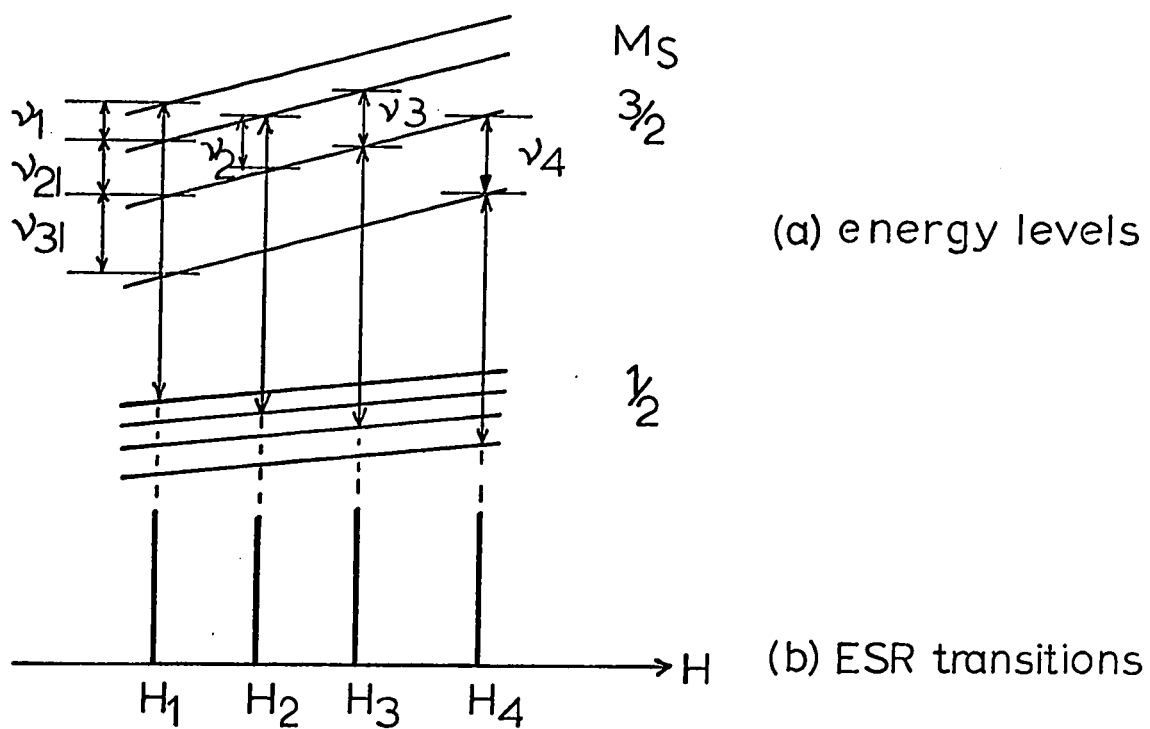


Figure 6.3 Labeling scheme for ENDOR spectra

subscript 1 indicates that the external field is set at H_1 , 2 that the field is set at H_2 and so on. For the field values H_1 and H_4 the choice of the nearest energy level is clear and it is seen with reference to Figure 6.2(a) and (d) that ν_1 and ν_4 are the most intense transitions in each spectrum. In Figure 6.2(b) the ν_2 transition is also the most intense. In Figure 6.2(c) ν_3 and ν_{33} are of approximately the same intensity, nevertheless, ν_3 as labeled is chosen as the direct transition since one would expect symmetrical behaviour as the field is varied from H_1 to H_4 . Also, the spectra of other alums, as that of $Rb(D_2O)$ for example, show that ν_3 transition as labeled is strongest at H_3 .

The second type of ENDOR transitions, termed in this work the indirect transitions, are designated with two subscripts. The first subscript goes from 1 to 3 in our case and refers to energy separations between the hyperfine levels, i.e., $m = 3/2 \rightarrow 1/2$ gives 1, $m = 1/2 \rightarrow -1/2$ gives 2, and $m = -1/2 \rightarrow -3/2$ gives 3. The second subscript plays the same role as the single subscript in the direct transitions. This labelling is used in parts (c) to (f) of Figure 6.3 to designate the transitions and it is specifically illustrated in part (a) of the Figure for the field value H_1 . This type of ENDOR transition differs from the direct type in that it partially desaturates the ESR transition by changing the populations in electronic sublevels not directly related to the ESR transition. As the electronic sublevels get further removed from the level involving the ESR transition the ENDOR signal is progressively weaker. The indirect transitions may occur in another way. They

may result from overlapping hyperfine structure. With the field set at H_1 there may be sufficient intensity of the hyperfine line centered at H_2 to observe its ENDOR frequency. The third type of ENDOR transition appearing in the spectra of Figure 6.2 are the lines designated by letter e. They are seen to be less intense than the other two types but quite discernible. The labelling of the e lines follows the same scheme that is used for the other types of transitions, the first subscript is 1 or 2 and the second subscript going from 1 to 4 specifies the field position in question. Measurements of the frequencies of the e lines indicate that within experimental precision they are exactly the arithmetic mean of the frequencies of the transitions flanking them. For example, the frequency of the e_{11} line in Figure 6.2 is equal to $1/2(\nu_1 + \nu_{21})$. More will be said concerning the e lines later.

The foregoing classification of the ENDOR lines in three types is empirical. Such a classification as far as is known, has not been stated elsewhere and it may well be that it is not pertinent theoretically. Nevertheless, the classification is convenient for the discussion of ENDOR spectra in this work and it does have experimental basis.

Concerning the intensities of the lines in Figure 6.2 it should be said that the spectra shown there were obtained under quite favorable experimental conditions. Most often, the only lines seen would be the direct transitions. Next to appear as the signal to noise ratio improved would be the indirect transitions and the e lines. The most critical condition in obtaining a good signal to noise ratio was found to be the

loaded Q of the sample cavity. This depended on the successful positioning of the ENDOR coil. Changes of the order of several tenths of a millimeter in the position of the coil from its optimum placement at room temperature as the cavity was cooled to liquid helium temperature, would suffice to increase the noise. At times no ENDOR signals could be obtained because of this difficulty.

Accurate measurements of the direct ENDOR transitions were made at the four hyperfine positions in the $M_S = \pm 3/2$ multiplets on the z axis and in the (111) plane. Because of the difficulty in obtaining the same accuracy in the frequency measurements of the indirect and e lines these measurements were not systematically made at all field values. An attempt, however, was made to measure accurately at one field value along with the direct transition the two associated indirect transitions and the e lines. A theoretical fit of these lines would serve as well as the fit of the direct lines in determining the spin Hamiltonian hyperfine parameters.

Table 6.2 presents experimental ENDOR measurements of the direct transitions on the low field and high field lines at the four hyperfine positions on the z axis and in the (111) plane. Presented also are the frequencies of the indirect transitions for one set of magnetic field values on the z axis.

The measured ENDOR frequencies in Table 6.2 were used in equations 3.16 and 3.17 to calculate the spin Hamiltonian hyperfine parameters to second order of perturbation theory. These parameters were then used as starting values, and the 16 X 16 matrix of the spin Hamiltonian for $^{53}\text{Cr}^{+3}$ was

Magnetic field Z Axis		Magnetic field ⊥ Z Axis							
M _S	H:	ENDOR freq. in MHz		M _S	H:	ENDOR freq. in MHz			
	gauss	measured	calculated		difference	gauss	measured	calculated	difference
3/2	H ₁ 2211.1	ν ₁ 77.9660	77.9676	+ .0016	3/2	3917.8	77.6797	77.6845	+ .0048
	H ₂ 2229.0	ν ₂ 78.4919	78.4911	- .0008		3932.9	78.0624	78.0584	- .0044
	H ₃ 2247.7	ν ₃ 78.4957	78.4964	+ .0007		3955.2	78.0779	78.0798	+ .0019
	H ₄ 2267.6	ν ₄ 79.0314	79.0306	- .0008		3972.4	78.4553	78.4564	- .0011
-3/2	H ₁ 4494.0	ν ₁ 76.9799	76.9794	- .0005	-3/2	2784.7	76.2150	76.2155	+ .0005
	H ₂ 4510.0	ν ₂ 77.2974	77.2999	+ .0025		2805.7	76.6945	76.6963	+ .0018
	H ₃ 4530.0	ν ₃ 77.2920	77.2919	- .0001		2822.9	76.6928	76.6936	+ .0008
	H ₄ 4550.9	ν ₄ 77.6161	77.6124	- .0037		2843.1	77.1769	77.1717	- .0052
ENDOR transitions at common field									
3/2	2267.6	ν ₁₄ 77.9909	77.9916	+ .0007	Microwave frequency 9.330 ± .002 Estimated experimental error: magnetic field ± .1 gauss ENDOR frequencies: direct transitions ± 0.002 MHz indirect transitions ± 0.003 MHz				
		ν ₂₄ 78.4993	78.4991	- .0002					
		ν ₄ 79.0314	79.0306	- .0008					
		ν ₁₄ 76.9653	76.9687	+ .0034					
-3/2	4550.9	ν ₂₄ 77.2928	77.2892	- .0036	Microwave frequency 9.347 ± .002 MHz				
		ν ₄ 77.6161	77.6124	- .0037					

Table 6.2 Cr(53) Experimental and calculated ENDOR frequencies in the Rb(H₂O) alum on the Z axis and in the perpendicular direction at 4.20K

diagonalized to obtain theoretical ENDOR transitions. The parameters were varied slightly until the best agreement in the sense of minimum deviation was obtained between measured and calculated frequencies. The ENDOR frequencies calculated in this manner are also presented and compared to the measured frequencies in Table 6.2 .

In Table 6.3 are presented the spin Hamiltonian parameters used in calculating the best ENDOR frequencies.

Table 6.3 Spin Hamiltonian parameters and their absolute signs for the Cr^{+3} ion in $\text{Rb}(\text{H}_2\text{O})$ alum at 4.2°K .

A	= + 52.1167	\pm	0.0020 MHz
B	= + 51.8743	\pm	0.0020 MHz
Q'	= - 0.0493	\pm	0.0010 MHz
g'_n	= - 0.31112	\pm	0.00050
D	= + 0.05342	\pm	0.00050 cm^{-1}
g_{II}	= 1.9751	\pm	0.0050
g_{\perp}	= 1.9734	\pm	0.0050

The absolute signs of the parameters D, A, B and Q' were determined as follows. It was found that the same agreement between experimental and theoretically calculated ENDOR frequencies as that given in Table 6.2 could be obtained for D negative, A negative and Q positive as for the case when all the signs were reversed. The agreement with experiment thus, only establishes

the magnitudes and the relative signs of the constants. The absolute sign of D however was established for the even isotope of chromium as described in Chapter V. This same results was also found for the odd isotope of chromium as stated at the beginning of this chapter. The sign of D was found to be positive for the Rubidium alums. With this additional information the absolute signs of the remaining constants can be established and are A positive and Q' negative. No other choice of signs for A and Q' with D positive will give agreement between experimental and theoretically calculated ENDOR frequencies.

The solution of the second order equations is instructive because in addition to obtaining hyperfine parameters as starting values for the matrix diagonalization, one can see the relative effect of the various hyperfine terms on the multiplets $M = \pm 3/2$. These effects are shown in Figure 6.4 as deviations in MHz from the energy levels as determined by the diagonal hyperfine term AMm . The resultant deviations in MHz are also given. The energy levels in the figure are labelled using the absolute signs of D , A , and Q' .

Correlation of the relative ENDOR line intensities for a given field value of Figure 6.2 with the energy level diagram in Figure 6.3 can be made, keeping in mind the order of accuracy of the EPR transitions, as follows. From Figure 6.2 it can be seen that at H_1 , say, the direct ENDOR transition is of lowest frequency. The remaining two indirect transitions are of progressively higher frequencies. Thus the fact that the intensity of ν_1 > intensity of ν_{21} > intensity ν_{31} is explained in terms of the energy level diagram.

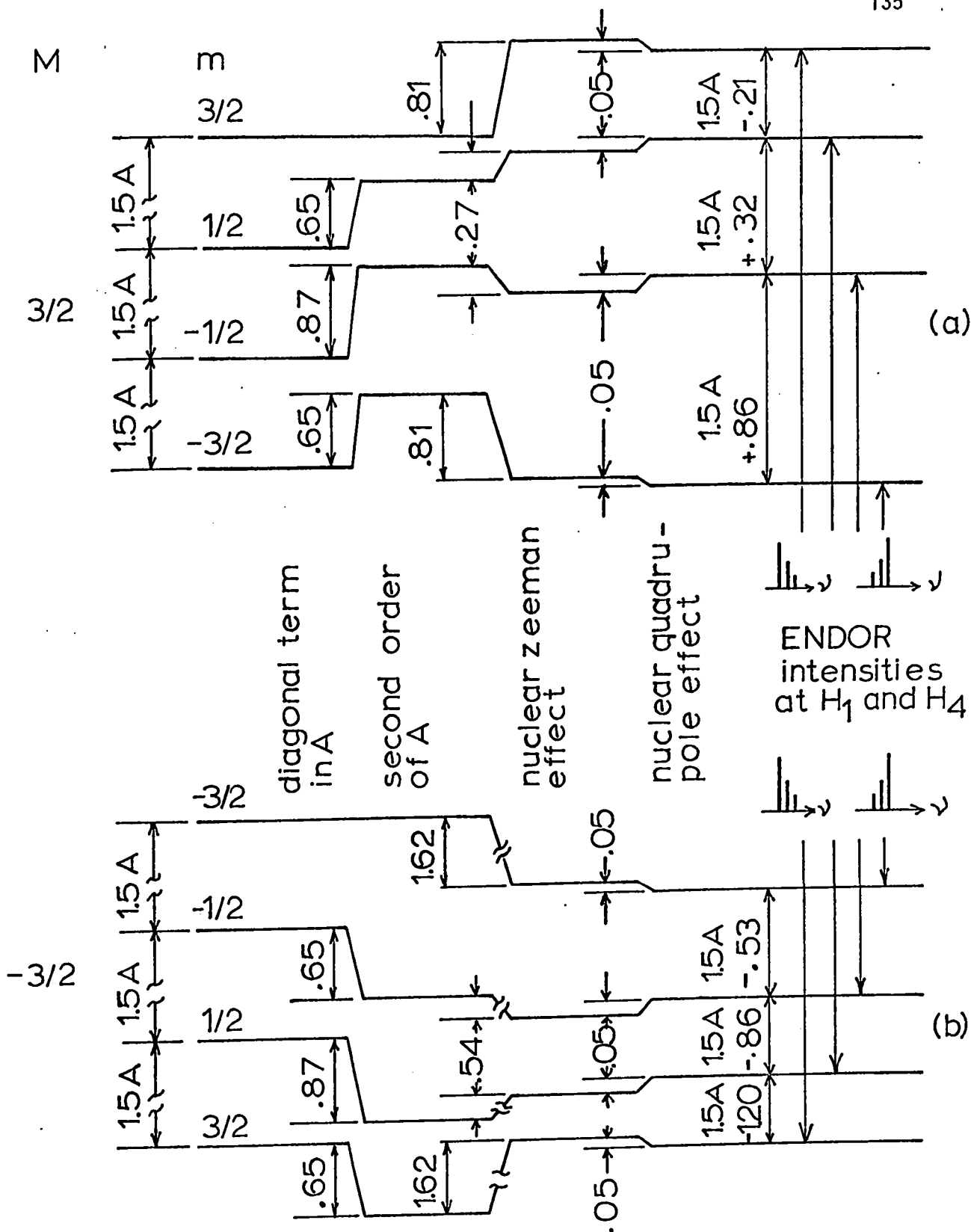


Figure 6.4 Hyperfine interactions of $^{53}\text{Cr}^{3+}$ in $\text{Rb}(\text{H}_2\text{O})$ alum at 4.2°K in MHz, (a) low field line, (b) high field line, $1.5A$ is about 78.2 MHz

B Crystals grown from solution in heavy water

The ESR hyperfine structure was unresolved in all deuterated rubidium crystals at liquid helium temperature. The initial assumption that lack of resolution was due to concentration broadening as was the case for some of the samples grown from solution in ordinary water, proved to be incorrect. This was established by successive addition of Rb_2SO_4 plus $\text{Ga}_2(\text{SO}_4)_3$ to the original solution and growing new crystals. Visually perfect, colorless, crystals grown after successive dilutions were found to have unresolved hyperfine structure. This is in contrast to the alums grown from ordinary water which were found to be of slightly pink colour due to the Chromium (53) but, nevertheless, had resolved hyperfine structure. In place of four closely spaced ESR lines for a given transition of the even isotope a single unresolved line was obtained. A typical Z axis spectrum at liquid helium temperature is shown in Figure 6.5. The lines associated with the $M_S = \pm 3/2 \rightarrow \pm 1/2$ transitions on the Z axis were within about 10 gauss of the field values found for these transitions for the even isotope. The positive sign of the zero field splitting parameter D was confirmed for these crystals by noting that the relative intensity of the high field line was greater than the intensity of the low field line. This feature is clearly evident in the spectrum of Figure 6.5.

Using the method described in part A of this Chapter, ENDOR measurements on the $M_S = \pm 3/2 \rightarrow \pm 1/2$ multiplets were made. In this instance it was impossible to say a priori where the hyperfine positions H_1 , H_2 , H_3 , and H_4 are. It was found, however, that ENDOR transitions could be obtained for all field values within the peak-to-peak range of the field values of the

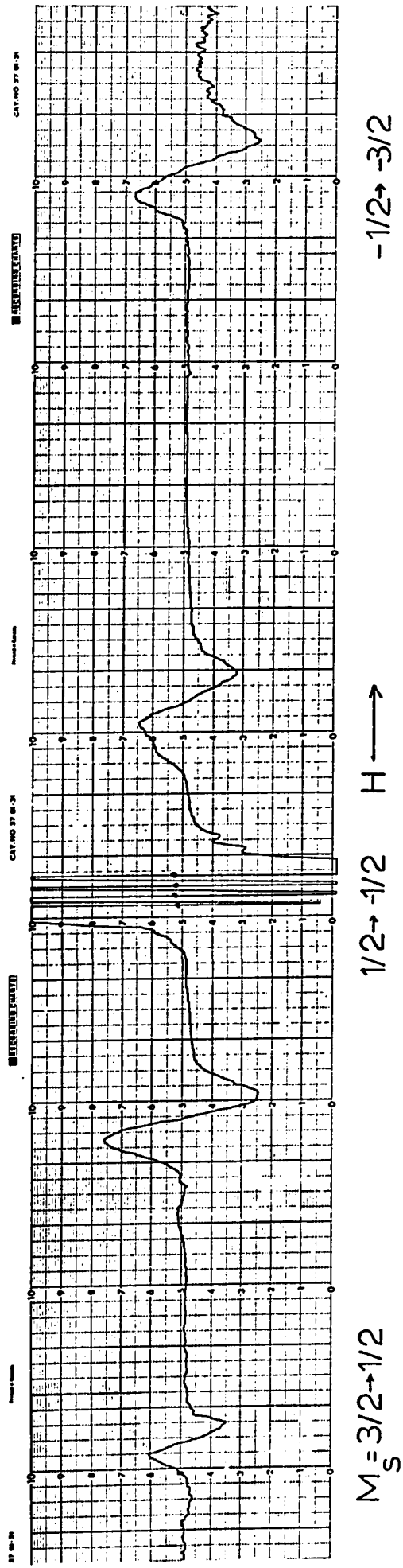


Figure 6.5 $^{53}\text{Cr}^{3+}$ Z axis in $\text{Rb}(\text{D}_2\text{O})$ at 4.2°K , magnetic field is along crystal $[111]$ direction.

ESR transitions $M_S = \pm 3/2 \rightarrow \pm 1/2$. ENDOR spectra were recorded as function of magnetic field within the two ESR transitions. It soon became evident that the ENDOR transitions maximized in intensity at characteristic magnetic field values. In analogy to results obtained in part A of this Chapter it was concluded that the maximum intensity lines are the direct transitions and that the field values associated with them are the centers H_1, H_2, H_3 and H_4 of the unresolved hyperfine lines.

Figure 6.6 shows the ENDOR spectra obtained for the $M_S = + 3/2 \rightarrow + 1/2$ multiplet. The analogy with the spectra in Figure 6.2 is almost complete. Figure 6.7 shows the ENDOR spectrum taken on the $M_S = -3/2 \rightarrow -1/2$ multiplet. ENDOR frequency measurements for the direct transitions at H_1, H_2, H_3 and H_4 along with indirect transitions at common magnetic field on the Z axis and direct transitions in the (111) plane are presented in Table 6.4. The method described in IA of this Chapter was used to calculate ENDOR frequencies. These are compared with the measured values. An energy level diagram, analogous to Figure 6.4 applies to the deuterated alum.

Angular variation of ENDOR frequencies in the (111) plane was studied for a range of 50° for the $M_S = \pm 3/2 \rightarrow \pm 1/2$ transitions. The procedure used was the following. The magnetic field was set at the center of the unresolved hyperfine lines of the above ESR transitions. The ENDOR frequencies ν_a, ν_b and ν_c associated with the transitions $\Delta m = 3/2 \rightarrow 1/2$, $1/2 \rightarrow -1/2$ and $-1/2 \rightarrow -3/2$, respectively, were measured. The magnet base was then rotated in steps of 5° until the range of 50° was covered. In each orientation the frequencies ν_a, ν_b , and ν_c were measured. Angular variation over a greater range was not done because beyond $\pm 25^\circ$ on either side of the

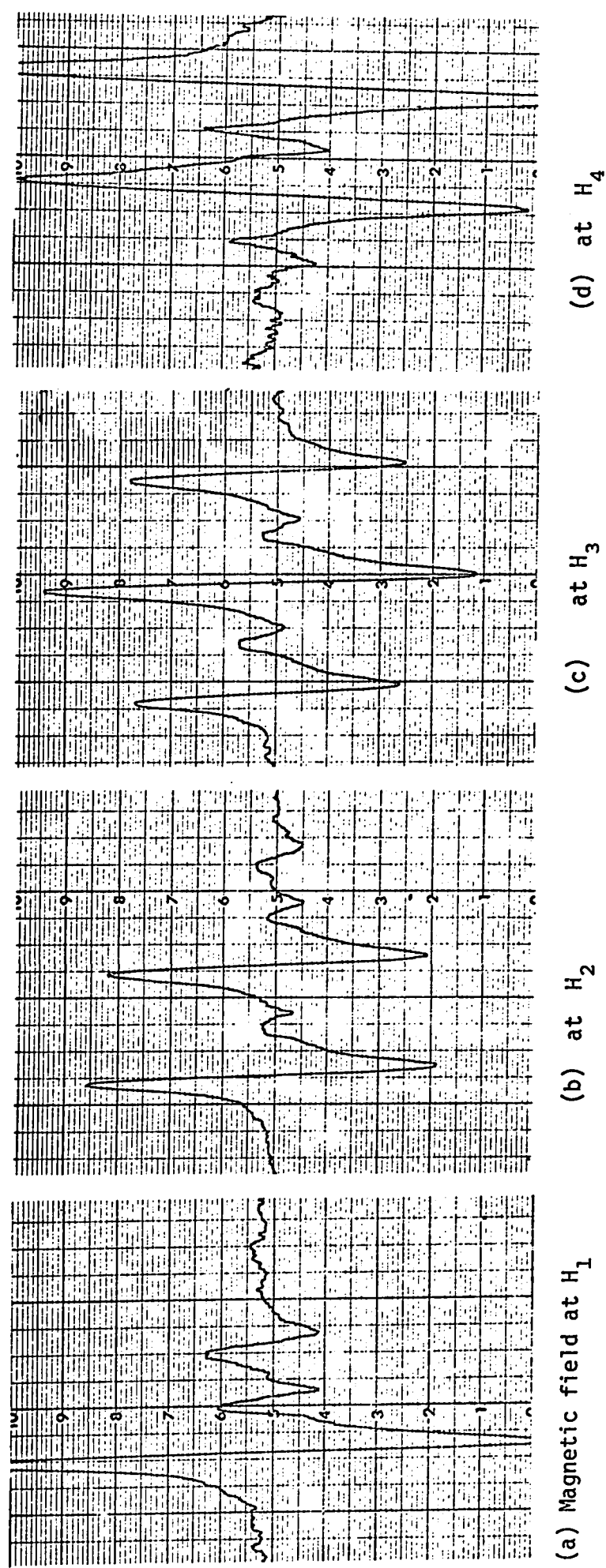


Figure 6.6 ENDOR spectra of $^{53}\text{Cr}^{3+}$ of the $M_g = 3/2$ multiplet in the $\text{Rb}(\text{D}_2\text{O})$ alum at 4.2°K . Identification of the lines is same as in Figure 6.2

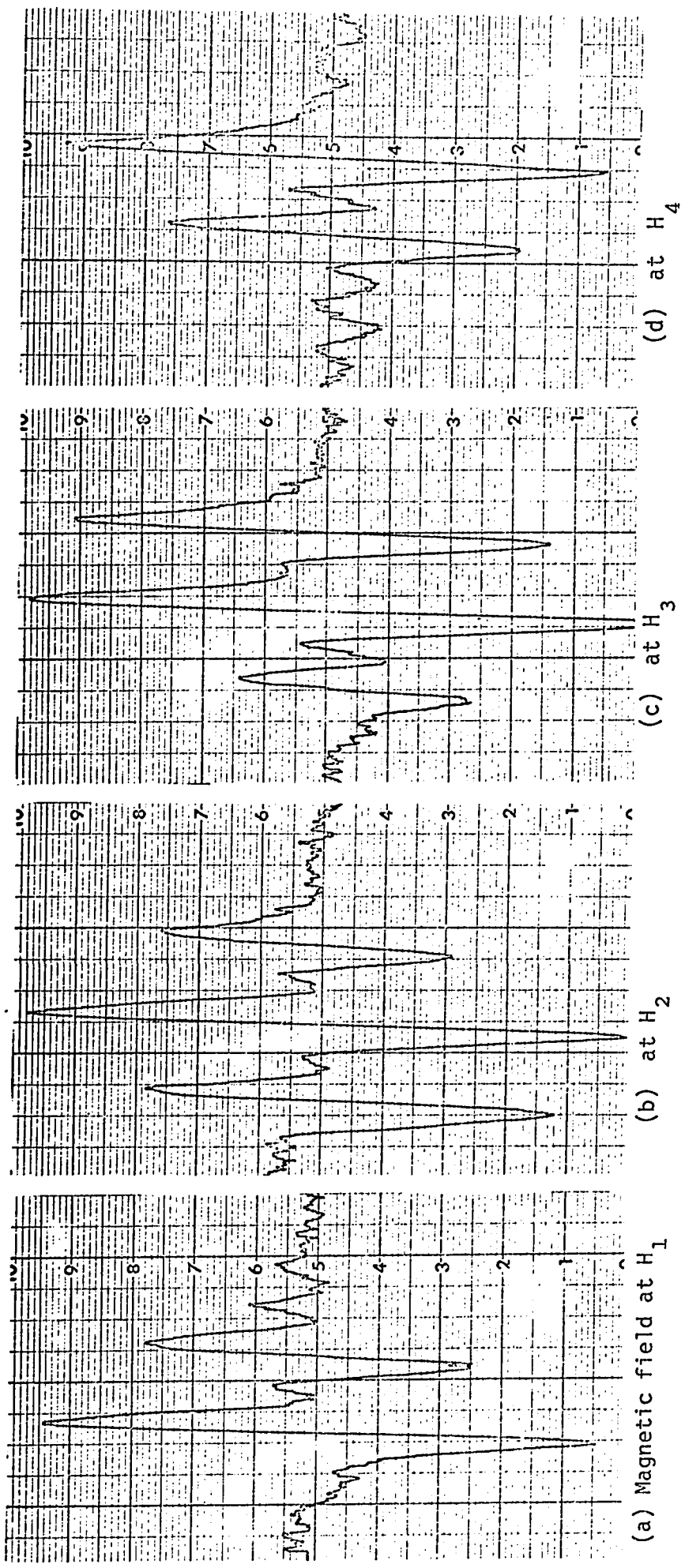


Figure 6.7 ENDOR spectra of $^{53}\text{Cr}^{3+}$ of the $M_S = -3/2$ multiplet in the $\text{Rb}(\text{D}_2\text{O})$ alum at 4.2°K . Identification of the lines is same as in Figure 6.2

Magnetic field Z axis				Magnetic field ⊥ Z axis					
M	H _i		ENDOR freq. in MHz		M _S	ENDOR freq. in MHz			
	gauss	measured	calculated	difference		gauss	measured	calculated	
3/2	H ₁	2219.4	77.9890	77.9916	+ .0026	3909.3	77.7173	77.7139	- .0034
	H ₂	2236.0	78.5156	78.5151	- .0005	3926.1	78.1020	78.1038	+ .0018
	H ₃	2252.7	78.5200	78.5205	+ .0005	3941.0	78.1158	78.1172	+ .0014
	H ₄	2269.4	79.0551	79.0520	- .0031	3961.1	78.4885	78.4911	+ .0026
-3/2	H ₁	4486.0	76.9986	77.0008	+ .0022	2797.0	76.2540	76.2609	+ .0069
	H ₂	4499.1	77.3250	77.3266	+ .0016	2815.7	76.7285	76.7363	+ .0078
	H ₃	4512.2	77.3230	77.3213	- .0017	2834.5	76.7304	76.7337	+ .0033
	H ₄	4525.4	77.6490	77.6471	- .0019	2853.3	77.2234	77.2144	- .0090
ENDOR frequencies at common field								Microwave frequency 9.350 ± .002 GHz	
3/2	ν ₁₃	2251.7	77.9962	78.0023	+ .0051	Estimated experimental error: Magnetic field ± 0.1 gauss ENDOR frequencies: direct transitions ± 0.002 MHz indirect transitions ± 0.003 MHz			
	ν ₃		78.5180	78.5205	+ .0025				
	ν ₃₃		79.0553	79.0493	- .0060				
-3/2		4505.9	76.9890	76.9954	+ .0064				
			77.3222	77.3239	+ .0017				
Microwave frequency 9.347 ± .002 GHz								Microwave frequency 9.350 ± .002 GHz	

Table 6.4 Cr(53) Measured and calculated ENDOR frequencies in the Rb(D₂O) alum on Z axis and in the perpendicular direction at 4.20K.

starting position the $M_S = \pm 3/2 \rightarrow \pm 1/2$ lines begin to cross with lines due to the other chromium complexes. The magnetic field value was constant for all readings taken for each ESR transition, this is a consequence of the fact that the ESR transitions $M_S = \pm 3/2 \rightarrow \pm 1/2$ have no angular variation in the (111) plane. The study of the angular variation of the ENDOR frequencies was carried out with the intention of establishing whether or not the hyperfine interactions were of axial symmetry. No experimental evidence for angular variation in the (111) plane was observed since the ENDOR transitions ν_a, ν_b and ν_c show no systematic angular trend in the 50° range investigated. This can be seen from data presented in Tables 6.5 and 6.6. Deviations from the average value in each group of frequencies are also given; these are attributed to experimental error. The fact that ENDOR transitions could be obtained for a common magnetic field value for a range of 50° in the (111) plane is taken as a very sensitive measure of the axial symmetry of the crystal field interaction. The fact that the ENDOR frequencies also show no angular variation in this plane is taken to mean that the hyperfine interactions are of axial symmetry and that the symmetry axis is parallel to the Z axis. The method described in IA of this Chapter was used to determine the hyperfine spin Hamiltonian parameters. The calculated ENDOR frequencies in Table 6.4 are obtained using these parameters; the parameters themselves are presented in Table 6.7.

An attempt was made to measure the effective nuclear g value by direct measurement of the divergence of two hyperfine levels in the $M_S + 3/2$ multiplet. The motivation for this effort came from noting the slight difference in the frequencies of the ν_2 and ν_3 ENDOR lines.

Table 6.5 Angular variation of ENDOR frequencies in the high field ESR line of the $\text{Rb}(\text{D}_2\text{O})$ alum in the (111) plane at 4.2°K .

Angle	$M_s = 3/2 \rightarrow 1/2$ H = $3935.9 \pm .1$ gauss Microwave frequency $9.347 \pm .002$ GHz					
Degree	ν_a m $3/2 \rightarrow 1/2$	Dev. from average	ν_b m $1/2 \rightarrow -1/2$	Dev. from average	ν_c m $-1/2 \rightarrow -3/2$	Dev. from average
-25	77.7405	- .0077	78.0929	- .0030	78.4930	+ .0100
-20	77.7596	+ .0114	78.1069	+ .0110	78.4901	+ .0071
-15	77.7503	+ .0021	78.1002	+ .0043	78.4885	+ .0055
-10	77.7513	+ .0031	78.0952	- .0007	78.4786	- .0044
- 5	77.7501	+ .0019	79.0931	- .0028	78.4834	+ .0004
0	77.7494	+ .0012	78.0948	- .0011	78.4793	- .0037
+ 5	77.7498	+ .0016	78.0926	- .0033	78.4722	- .0108
+10	77.7484	+ .0002	78.0974	+ .0015	78.4814	- .0016
+15	77.7416	- .0066	78.0943	- .0016	78.4821	- .0009
+20	77.7439	- .0043	78.0921	- .0038	78.4715	- .0115
+25	77.7458	- .0024	78.0956	- .0003	78.4938	+ .0108
Average	77.7482		78.0959		78.4830	

Note: ENDOR frequencies are in MHz, estimated error in measurement is ± 0.003 MHz

Table 6.6 Angular variation of the ENDOR frequencies in the low field ESR line of the Rb(D₂O)₂ alum in the (111) plane at 4.2°K.

Angle	M _S = - 3/2 → -1/2 H = 2825.1 ± .1 gauss Microwave frequency 9.347 ± .002 GHz					
Degree	ν_a m 3/2 → 1/2	Dev. from average	ν_b m 1/2 → -1/2	Dev. from average	ν_c m -1/2 → -3/2	Dev. from average
-25	76.2386	- .0016	76.7285	+ .0006	77.2531	+ .0018
-20	76.2361	- .0041	76.7274	- .0005	77.2603	+ .0090
-15	76.2398	- .0004	76.7357	+ .0078	77.2498	- .0015
-10	76.2428	+ .0026	76.7238	- .0041	77.2488	- .0025
- 5	76.2423	+ .0021	76.7246	- .0033	77.2473	- .0040
0	76.2385	- .0017	76.7242	- .0037	77.2462	- .0051
+ 5	76.2409	+ .0007	76.7261	- .0018	77.2507	- .0006
+10	76.2438	+ .0036	76.7251	- .0028	77.2492	- .0021
+15	76.2376	- .0026	76.7274	- .0005	77.2546	+ .0033
+20	76.2433	+ .0031	76.7283	+ .0004	77.2483	- .0030
+25	76.2395	- .0007	76.7358	+ .0079	77.2563	+ .0050
Average	76.2402		76.7279		77.2513	

Note: ENDOR frequencies are in MHz, estimated error in measurement is ± 0.003 MHz

Table 6.7 Spin Hamiltonian parameters and their absolute signs for the Cr^{+3} ion in $\text{Rb}(\text{D}_2\text{O})$ alum at 4.2°K .

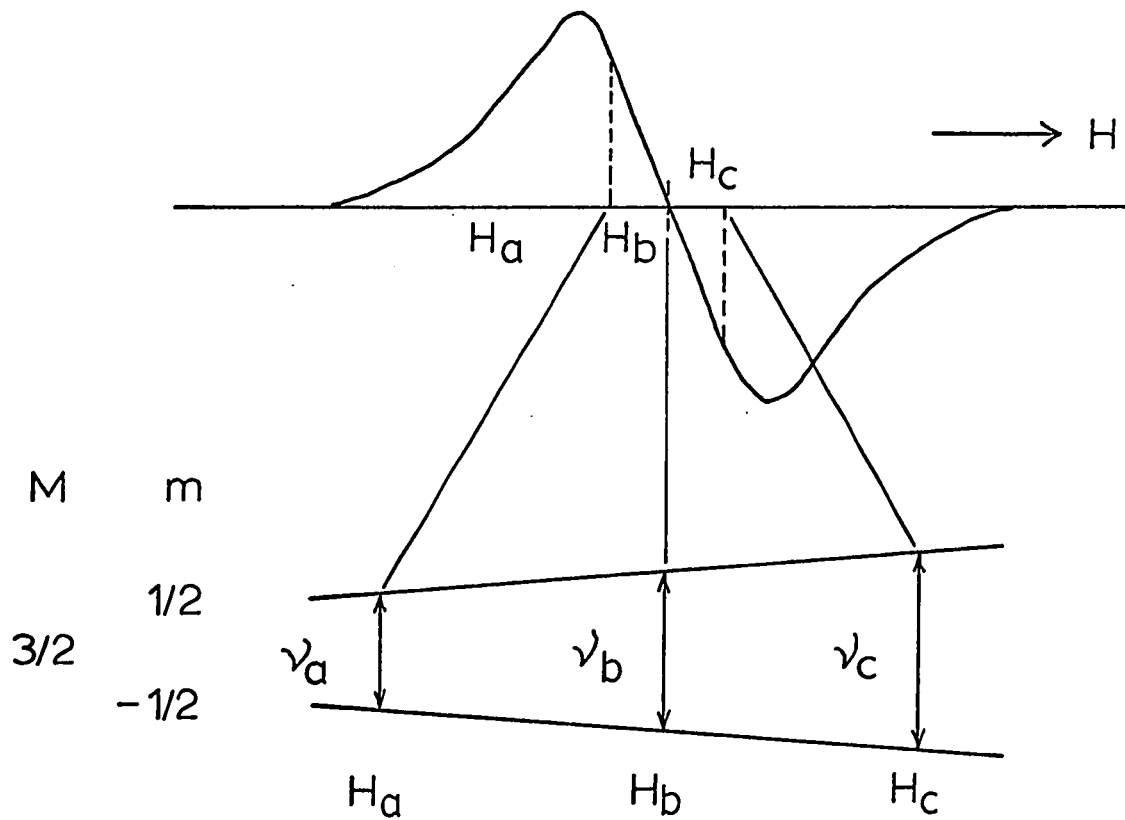
A	=	+ 52.1317	±	0.0020	MHz
B	=	+ 51.8908	±	0.0020	MHz
Q'	=	- 0.0494	±	0.0010	MHz
g'_n	=	- 0.31119	±	0.00050	
D	=	+ 0.05267	±	0.00050	cm^{-1}
g_{II}	=	1.9799	±	0.0050	
g_{I}	=	1.9688	±	0.0050	

For the $M_S = +3/2$ set one has 77.5156 and 78.5200 MHz respectively for these frequencies. These transitions are between the levels $m = +1/2 \rightarrow -1/2$ and differ in the magnetic field at which they are measured i.e. H_2 and H_3 respectively. The frequency difference is attributed to the difference in the Nuclear Zeeman terms, i.e. $g'_n \beta_n H_3 - g'_n \beta_n H_2$. The observed frequency difference .0044 MHz is of the order of the experimental error. Careful measurements, however, revealed a constant average difference of this magnitude. The same effect was observed in the ν_2 and ν_3 frequencies of the $M_S = -3/2$ set. There, however, the hyperfine levels tend to converge due to the nuclear Zeeman effect.

In order to maximize the frequency difference in the ν_2 and ν_3 lines these transitions were measured as indirect transitions. That is measurements were made at as low and at as high magnetic field values where these lines could be observed. The magnetic field values and ENDOR frequencies are

presented diagrammatically in Figure 6.8 along with tabulation of the magnetic field values, associated ENDOR frequencies, and the calculated effective g value. The calculation of the effective g value is based only on the nuclear Zeeman term. It is recognized that the more exact calculation should take into account the off-diagonal terms in the matrix of the spin Hamiltonian. This effect, however, is approximately the same for all the transitions ν_a , ν_b and ν_c , differing only because of a small magnetic field dependence. In calculating $g'_n (= \Delta\nu/\beta_n \Delta H)$ the effect of the off-diagonal terms cancels out but for this field dependence. Thus calculated g'_n values are within about 6% of the value given in Table 6.7. The experimental error in such a determination of g'_n is high because small differences of large numbers (i.e. $\Delta\nu$) are involved in the calculation. Considering this and the above mentioned magnetic field dependence of the contribution due to off-diagonal elements to the ENDOR transitions ν_a , ν_b and ν_c it is easy to see that the discrepancy of 6% could result.

The purpose of presenting this approximate means of determining the effective nuclear g value is to demonstrate the nuclear Zeeman effect via the ENDOR technique in a very direct manner. This is as opposed to the determination of g'_n which involves fitting the experimental data by varying the parameters A , B , Q' and g'_n . This method, is considerably more accurate since it involves fitting of a large number of ENDOR lines which are well separated in the magnetic field, (e.g. ΔH for $M_S = +3/2$ and $M_S = -3/2$ is about 2300 gauss).



	H gauss	ν Mhz	$ g'_n $
a	2239.2	78.5108	$a \leftrightarrow b$.33738
b	2266.8	78.5179	$b \leftrightarrow c$.33292
c	2292.8	78.5245	$a \leftrightarrow c$.33522

Figure 6.8 Observation of nuclear Zeeman effect by the ENDOR technique

II The Cesium Alums, crystals grown from solution in ordinary water and heavy water

The experimental procedure used in studying these two crystals and the results obtained are quite similar. For this reason the subsequent, discussion refers to both the hydrated and the deuterated crystals.

The z axis ESR spectrum at 4.2°K for the Cs(H₂O) crystal is shown in Figure 6.9; the alignment is to within about 1°. An entirely similar spectrum was obtained for the deuterated crystal. As can be seen, the hyperfine structure is nearly resolved. The low field set of lines is more intense than the high field set. This means that the sign of D is negative; a result also obtained for the even isotope of chromium. The apparent increased separation of the hyperfine lines at high field with respect to the ones at low field is due to slight non-linearity in the magnetic field sweep. A small forbidden set of lines designated by the letter f in the figure is also visible. The set of lines flanking the $M_S = 1/2 \rightarrow -1/2$ transitions, which are due to the remaining three complexes of chromium (53) contain 3X 4 ESR transitions. They are slightly misaligned due to imperfect orientation of the crystal. A deviation of the Z axis from the external field by about 1° would produce the observed effect.

ENDOR in the 75 MHz range was obtained for the ESR transitions $M_S = \pm 3/2 \rightarrow \pm 1/2$. The procedure was the same as used in the measurements on the Rb(H₂O) crystals. Typical spectra for these lines in the deuterated alum at the fields H_1, H_2, H_3 and H_4 are presented in Figures 6.10 and 6.11. Figure 6.10 pertains to the $M_S = -3/2 \rightarrow -1/2$ ESR transitions and Figure 6.11 to the $M_S +3/2 \rightarrow +1/2$

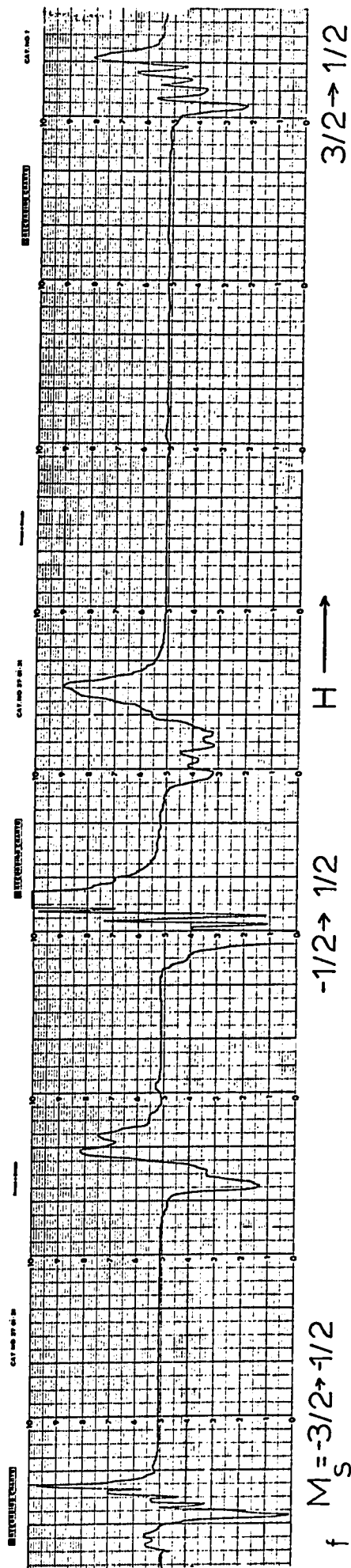


Figure 6.9 $^{53}\text{Cr}^{3+}$ Z axis in $\text{Cs}(\text{H}_2\text{O})$ at 4.2°K , magnetic field is along crystal $[111]$ direction

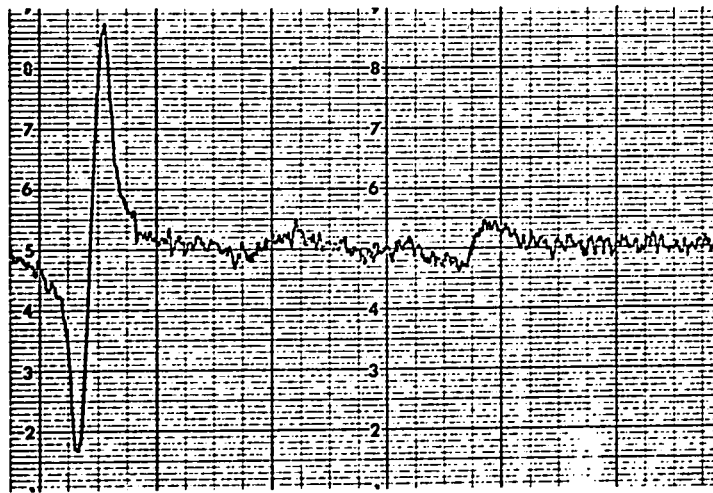
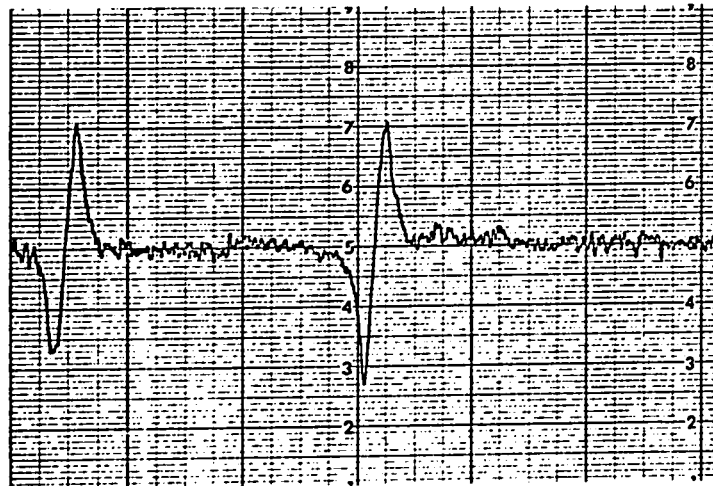
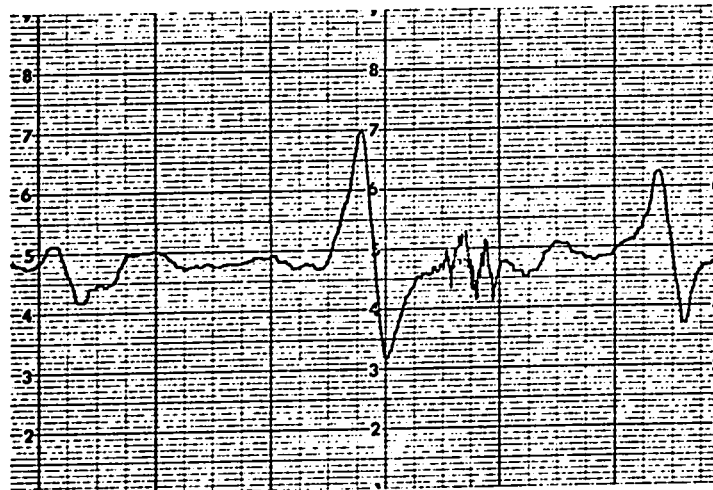
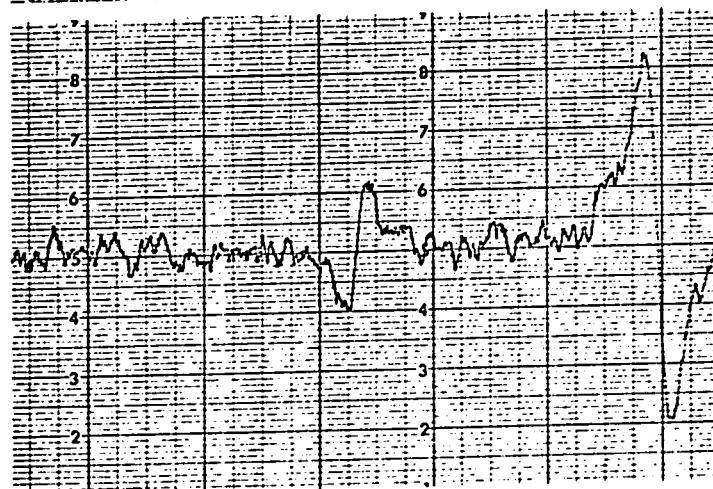
(a) Magnetic field at H_1 (b) at H_2 (c) at H_3 (d) at H_4

Figure 6.10 ENDOR spectra
of $^{53}\text{Cr}^{3+}$ of $M_S = -3/2$
set in $\text{Cs}(\text{D}_2\text{O})$ alum
at 4.2°K

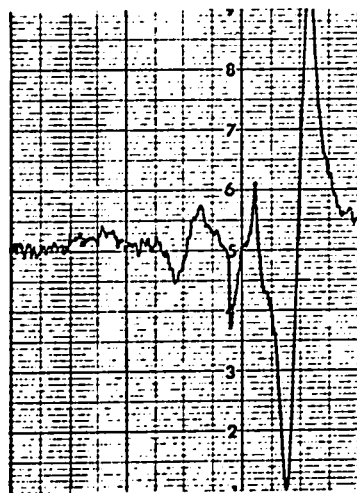
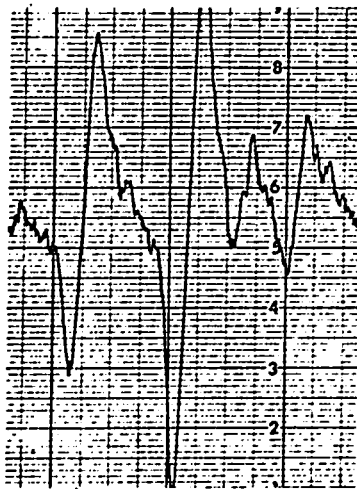
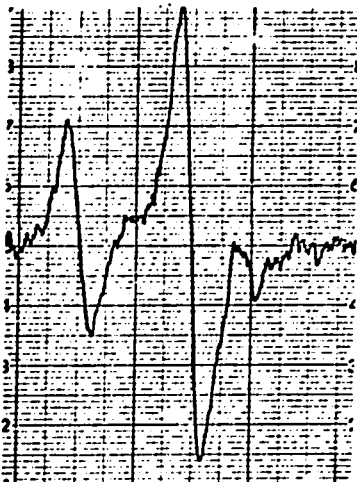
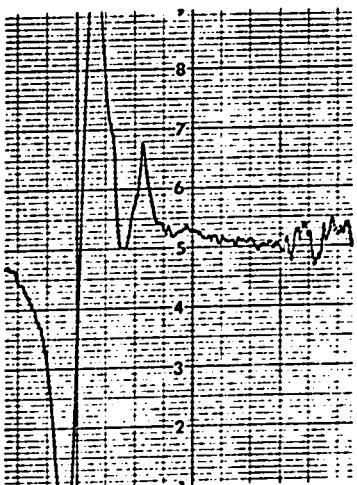
(a) Magnetic field at H_1 (b) at H_2 (c) at H_3 (d) at H_4

Figure 6.11 ENDOR spectra of $^{53}\text{Cr}^{3+}$ of $M_S = 3/2$ set in $\text{Cs}(\text{D}_2\text{O})$ alum at 4.2°K .

transitions. Both are presented in order to show the characteristic reversal of the intensity pattern from the high field set to the low field set.

In the rubidium alums the same intensity pattern was obtained as one goes from H_1 to H_4 at both the high field and low field. Measurements on the Z axis and in the (111) plane for the above transitions are presented in Table 6.8 and 6.9 for the crystals grown from ordinary water and heavy water, respectively.

Partial angular variation of ENDOR for the deuterated crystals was studied. Measurements in the $M_S = +3/2 \rightarrow +1/2$ multiplet were made for a range of about 40° in the (111) plane. The experimental results are presented in Table 6.10. In this instance since the hyperfine structure is resolved, the direct ENDOR transitions, ν_1 , ν_2 , ν_3 and ν_4 were measured. The frequency deviations from the mean value are within the experimental error. Thus, to this accuracy, there is no systematic angular variation of the ENDOR frequencies in the (111) plane. This means that the hyperfine interactions are of axial symmetry and that the symmetry axis is parallel to the z axis.

Also, all sets of readings were made at common magnetic field values. This observation, as was the case for the rubidium alum, implies no angular variation for the ESR line in question. This finding very accurately confirms the purely axial symmetry of the crystal field interaction. The measured ENDOR frequencies presented in Tables 6.8 and 6.9 were used to solve the second order equations 3.16 & 3.17 to obtain the hyperfine interaction parameters A, B, Q' and g'. These were used as starting values for the diagonalization of the 16 X 16 matrix of the spin Hamiltonian.

Magnetic field Z axis				Magnetic field ⊥ Z axis					
M _s	H:		ENDOR freq. in MHz		M _s	ENDOR freq. in MHz			
	gauss	measured	calculated	difference		gauss	measured	calculated	
3/2	H ₁	5785.3	78.8684	78.8730	+ .0046	2653.4	77.1106	77.1129	+ .0023
	H ₂	4803.9	78.3858	78.3816	- .0042	2672.3	78.0115	78.0050	- .0065
	H ₃	4823.6	78.3916	78.3869	- .0047	2697.7	78.0278	78.0264	- .0014
	H ₄	4841.9	77.9143	77.9062	- .0081	2717.2	78.9150	78.9158	+ .0008
-3/2	H ₁	1934.5	75.8446	75.8470	+ .0024	4055.3	77.1933	77.1957	+ .0024
	H ₂	1953.0	77.1926	77.2011	+ .0085	4082.8	77.1582	77.1530	- .0052
	H ₃	1972.5	77.1944	77.1877	- .0067	4097.2	77.1407	77.1477	+ .0070
	H ₄	1992.4	78.5495	78.5445	- .0050	4114.8	77.1163	77.1076	- .0087
ENDOR frequencies at common field								Microwave frequency 9.350 ± .002 MHz	
3/2	H ₄	4841.9	77.9143	77.9062	- .0081	Estimated experimental error; magnetic field + 0.1 gauss ENDOR frequencies; direct transitions ± 0.002 MHz indirect transitions ± 0.003 MHz			
			78.4009	78.3923	- .0086				
			78.8957	78.9024	+ .0067				
-3/2	H ₃	1972.5	75.8278	75.8363	+ .0085				
			77.1944	77.1877	- .0067				
			78.5519	78.5525	+ .0006				
Microwave frequency 9.352 ± .002 MHz									

Table 6.8 Cr(53) Measured and calculated ENDOR frequencies in Cs(H₂O) alum on Z axis and in the perpendicular direction at 4.20K

Magnetic field Z axis				Magnetic field ⊥ Z axis						
M _S	H _i		ENDOR frequency in MHz		M _S	H _i		ENDOR frequency in MHz		
	gauss	measured	calculated	difference		gauss	measured	calculated	difference	
3/2	H ₁	4839.7	78.9242	78.9238	- .0004	2624.3	77.0842	77.0782	- .0060	
	H ₂	4865.1	78.4388	78.4350	- .0038	2643.4	77.9643	77.9649	+ .0006	
	H ₃	4882.1	78.4418	78.4377	- .0041	2654.9	77.9755	77.9783	+ .0028	
	H ₄	4893.6	77.9503	77.9543	+ .0040	2684.5	78.8857	78.8864	+ .0007	
-3/2	H ₁	1859.3	75.8910	75.8950	+ .0040	4086.4	77.2002	77.2064	+ .0062	
	H ₂	1875.7	77.2467	77.2518	+ .0051	4104.5	77.1643	77.1610	- .0033	
	H ₃	1891.7	77.2436	77.2465	+ .0029	4120.4	77.1645	77.1583	- .0062	
	H ₄	1911.6	78.6084	78.6033	- .0051	4140.2	77.1214	77.1263	+ .0049	
ENDOR frequencies at common field										
3/2	H ₂		4865.1	78.9360	78.9318	- .0042	Microwave frequency 9.351 ± .002 GHz			
	H ₂		4865.1	78.4388	78.4350	- .0038	Estimated experimental error:			
	H ₂		4865.1	77.9432	77.9489	+ .0057	magnetic field ± 0.1 gauss			
-3/2	H ₃		1891.7	75.8821	75.8870	+ .0049	ENDOR frequencies:			
	H ₃		1891.7	77.2436	77.2465	+ .0029	direct transitions ± 0.002 MHz			
	H ₃		1891.7	78.6164	78.6113	- .0051	indirect transitions ± 0.003 MHz			
Microwave frequency 9.352 ± .002 GHz										

Table 6.9Cr(53) Measured and calculated ENDOR frequencies in Cs(D₂O) alum on Z axis and in the perpendicular direction at 4.2°K

Table 6.10 Angular variation or ENDOR frequencies in the low field ESR line of the $\text{Cs}(\text{D}_2\text{O})$ alum in the (111) plane at 4.2°K .

$M_S = 3/2 \rightarrow 1/2$	H_1 2624.3 gauss ν_1 MHz	Dev. from average MHz	H_2 2647.5 gauss ν_2 MHz	Dev. from average MHz	H_3 2666.7 gauss ν_3 MHz	Dev. from average MHz	H_4 2685.9 gauss ν_4 MHz	Dev. from average MHz
-20	77.0633	+ .0029	77.9634	- .0030	77.9834	+ .0010	78.8820	- .0018
-15	77.0579	- .0025	77.9672	+ .0008	77.9837	+ .0013	78.8784	- .0054
-10	77.0610	+ .0006	77.9641	- .0023	77.9795	- .0029	78.8825	- .0013
- 5	77.0554	- .0050	77.9673	+ .0009	77.9810	- .0014	78.8818	- .0020
+ 5	77.0606	+ .0002	77.9682	+ .0018	77.9824	.0000	78.8869	+ .0031
+10	77.0625	+ .0021	77.9684	+ .0020	77.9864	+ .0040	78.8861	+ .0023
+15	77.0623	+ .0019	77.9662	- .0002	77.9834	+ .0010	78.8856	+ .0018
+20	77.0610	+ .0016	77.9650	- .0014	77.9821	- .0003	78.8845	+ .0007
Average	77.0604		77.9664		77.9824		78.8838	

Estimated experimental error:
magnetic field values ± 0.1 gauss
ENDOR frequencies ± 0.002 MHz

The parameters were varied slightly until the best agreement between experimental and calculated ENDOR frequencies was obtained. Thus calculated hyperfine parameters of the Cs alums are presented in Table 6.11

Table 6.11 Spin Hamiltonian parameters and their absolute signs for the Cr^{+3} ion in the $\text{Cs}(\text{H}_2\text{O})$ and $\text{Cs}(\text{D}_2\text{O})$ alums at 4.2°K

Parameter	$\text{Cs}(\text{H}_2\text{O})$ alum	$\text{Cs}(\text{D}_2\text{O})$ alum	
A	$+ 51.6358 \pm 0.0020$	$+ 51.6596 \pm 0.0020$	MHz
B	$+ 52.4263 \pm 0.0020$	$+ 52.4755 \pm 0.0020$	MHz
Q'	$+ 0.4639 \pm 0.0010$	$+ 0.4630 \pm 0.0010$	MHz
g'_n	$- 0.31114 \pm 0.00050$	$- 0.31116 \pm 0.00050$	--
D	$- 0.06701 \pm 0.00050$	$- 0.06984 \pm 0.00050$	cm^{-1}
g_{II}	1.9718 ± 0.0050	1.9747 ± 0.0050	--
g_{I}	1.9722 ± 0.0050	1.9696 ± 0.0050	--

As for the case of the Rb alums, agreement between experimental and calculated frequencies could be obtained if the signs of the parameters D , A and Q' were reversed. The establishment of the absolute sign of D , as previously described, determines the sign of the remaining parameters.

The energy level diagram of Figure 6.12 pertaining to the deuterated alum, and based on the second order equations 3.16 and 3.17, shows the effect of the hyperfine interactions on the energy levels as determined by the diagonal term AM_n . The labeling of the energy levels is consistent with the absolute signs of the spin Hamiltonian parameters. The reversal of the ENDOR intensity patterns at high and low magnetic field evident in Figures 6.10 and 6.11 can be explained on the basis of the energy levels in Figure 6.12. It is seen with reference to Figure 6.12 that at low field, the direct ENDOR transition at H_1 , hence the most intense, is the lowest frequency line whereas at H_4 the direct transition, hence the most intense line, is the highest frequency line. At high field the reverse is seen to be the case as reference to part (b) of the figure will show. The reversals of the intensity patterns in Figures 6.10 and 6.11 are thus explained.

III The "e" ENDOR transitions

The presence of these transitions, under moderately favorable experimental conditions, was fairly clear in the Rb alums both on the Z axis and in the perpendicular direction. In the Cs alums some traces of e lines were apparent in the high field ESR line on the Z axis. At no time were the e lines observed in the low field ESR line. Data on the z axis of the Rb alums is presented in Table 6.12. The table shows the comparison of twice a given e line frequency with the sum of the ENDOR frequencies flanking it. It is seen that this association can be made since the differences found can be accounted for by experimental error. The e lines were observed for other orientations of the magnetic field. They were seen in the (111) plane and other positions of the Z axis. The intensity of the lines did not seem to depend on the orientation of the magnetic field.

An explanation of the e lines that readily comes to mind is that the $\Delta m_{\pm} = \pm 2$ ENDOR transitions are being observed via the second harmonic content in the RF signal applied to the ENDOR coil. Via this effect direct and indirect ENDOR transitions were often observed. For example it was possible to detect the 75 MHz lines by sweeping the RF generator at one half this frequency. In analogy to this situation, the e lines may be transitions in the 150 MHz range. There is however, one serious draw back to this explanation. When the Rf field is swept in the 150 MHz range one would expect to observe the e lines via the first harmonic power content, as was the case for the direct and indirect ENDOR transitions in the 75 MHz range.

Table 6.12 Direct, indirect and "e" ENDOR transitions on the Z axis of the Rb alums at 4.2⁰k.

		Rb(H ₂ O) alum		(Z axis)	
Field H ₄ 2267.6 (M _S 3/2)	v ₁₄	77.9665	v ₁₄ + v ₂₄	= 156.4658	
	e ₁₄	78.2363	2(e ₁₄)	= 156.4726	Δ = 0.0068 MHz
	v ₂₄	78.4993			
	e ₂₄	78.7660	v ₂₄ + v ₄	= 157.5307	
	v ₄	79.0314	2(e ₂₄)	= 157.5320	Δ = 0.0013 MHz
Field H ₃ 4550.9 (M _S -3/2)	v ₁₄	76.9573	v ₁₄ + v ₂₄	= 154.2501	
	e ₁₄	77.1337	2(e ₁₄)	= 154.2674	Δ = 0.0173 MHz
	v ₂₄	77.2928			
	e ₂₄	77.4493	v ₂₄ + v ₄	= 154.9089	
	v ₄	77.6161	2(e ₂₄)	= 154.8986	Δ = 0.0103 MHz
		Rb(D ₂ O) alum		(Z axis)	
Field H ₃ 2251.7 (M _S 3/2)	v ₁₃	77.9962	v ₁₃ + v ₃	= 156.5162	
	e ₁₃	78.2538	2(e ₁₃)	= 156.5076	Δ = 0.0086 MHz
	v ₃	78.5200	v	v	
	e ₂₃	78.7869	v ₃ + v ₃₃	= 157.5753	
	v ₃₃	79.0553	2(e ₂₃)	= 157.5738	Δ = 0.0015 MHz
Field ~H ₂ 4505.9 (M _S -3/2)	~v ₁₂	76.9890	v ₁₂ + v ₂	= 154.3110	
	~e ₁₂	77.1563	2(e ₁₂)	= 154.3126	Δ = 0.0016 MHz
	~v ₂	77.3222			
	~e ₂₂	77.4950	v ₂ + v ₃₂	= 154.9776	
	~v ₃₂	77.6554	2(e ₂₂)	= 154.9900	Δ = 0.0124 MHz

Estimated error: direct transitions ± 0.001 MHz
indirect transitions ± 0.003 MHz ---- "e" transitions ± 0.005 MHz.

Transitions in the 150 MHz frequency range were observed, however, they coincided exactly with two times the direct and indirect transitions in the 75 MHz range. That is the 75 MHz transitions were being detected via the first subharmonic of the 150 MHz frequency. No transitions in the 150 MHz range were found that could be related to the e line frequencies. It is possible, therefore, that the second harmonic of the 75 MHz frequency range plays no part in the e line transitions.

Another possibility is that ENDOR transitions at e line frequencies are actually being observed. If this is the case one has to find a mechanism whereby the transition ν corresponding to $\Delta m_I = \pm 2$ is being made via the e line frequency which is $1/2$ of ν . Double photon absorption is one possibility. The probability of this occurring is small. No example of double photon absorption detected via ENDOR is known to the author. Another possible explanation is based on the fact that e lines were observed only in cases where there was some overlap of the direct and indirect ENDOR transitions. Consider the first entry in Table 6.12, as the ENDOR frequency is swept past the centerline ν_{14} and into the wing of this line some transitions $\Delta m_I = 3/2 \rightarrow 1/2$ are still being made at the frequency e_{14} . At this frequency, the wing of the transition ν_{24} begins to contribute to the transitions $\Delta m_I = 1/2 \rightarrow -1/2$. Thus at the frequency e_{14} both the $\Delta m_I = 3/2 \rightarrow 1/2$ and $\Delta m_I = 1/2 \rightarrow -1/2$ transitions are being made. Now, possibly, if the Chromium (53) spin lattice relaxation time is sufficiently slow the resultant transition $\Delta m_I = 3/2 \rightarrow -1/2 = \nu$ may be made at the frequency $e_{14} = 1/2 \nu$. In effect, then, the overlap of the ENDOR transitions $\Delta m_I = 3/2 \rightarrow 1/2$ and $\Delta m_I = 1/2 \rightarrow -1/2$ acts as a bridge for the resultant transition $\Delta m_I = 3/2 \rightarrow -1/2$

CHAPTER VII
DISCUSSION AND CONCLUSIONS

A. ESR of Cr^{3+} in the alums

From the results presented in Chapter V it is clear that the Rb and Cs alums belonging to the α and β types, respectively, exhibit many common features. In both crystals four differently oriented but otherwise equivalent complexes of $^{52}\text{Cr}^{3+}$ were observed. The Z axis of these complexes pointed along the $\langle 111 \rangle$ crystal directions. This was true at room temperature and at 4.2°K . At both temperatures the fine structure spin Hamiltonian of axial symmetry adequately described the $^{52}\text{Cr}^{3+}$ spectrum. It was observed that the trigonal component of the crystal field in the Rb alums decreased from the room temperature value by about 40% at 4.2°K . and by about 8% in the Cs alum. This observation is similar to that of Bleaney's for the Rb, Cs and NH_3CH_3 chrome alums. The sign of the D parameter was found to be positive for the Rb alum and negative for the Cs alum. The changes in the D parameter are attributed to slight movement of the water molecules about the Cr^{3+} ion which at 4.2°K are closer to octahedral arrangement than at room temperature. It is tempting to speculate that the reversal of the signs of the D parameter in the two alums is associated with a trigonal compressional and trigonal extensional distortion of the water molecules about the Cr^{3+} ion.

It was hoped that because of relatively low concentration of chromium it would be possible to observe the hyperfine structure due to the odd isotope.

This was not found to be the case. Deuterated form of the alum also did not show hyperfine structure. It is concluded that inhomogeneous broadening of the even isotope line obscured the four fine structure lines. The inhomogeneous broadening is probably due in part to random crystal fields and in part to a distribution of magnetic fields set up at the chromium ion by neighbours possessing nuclear spin. The hope that deuteration of the alums would lead to narrower line widths was not realized. The deuterated crystals did serve a useful function in this work, however, by providing a duplicate set of measurements in both the ESR and the ENDOR study. This duplication has lent strong support to all measurements.

The soda alum, the only known member of the γ type, behaved identically to the Rb and Cs alums as observed by ESR at room temperature. The measured D value was different from Rb and Cs alums. The behaviour of the Na alum at low temperature was not studied because of the crystals tendency to break into small crystallites. The sign of the D parameter was established, however, as described in chapter V. Though experimentally difficult it would be of interest to attempt to study this crystal at low temperature because of its unique nature in the alum family. With regard to the pseudo soda alum the following may be pointed out. The chromium sites in pseudo soda alum show a large rhombic distortion, with the magnitude of the E parameter of the spin Hamiltonian being approximately 1/3 that of the D parameter. Such a case as this is rarely found in the literature. It could mean that the atoms in a unit cell are tightly packed. Since the cell volume of "pseudo soda alum" is smaller than that of soda alum it probably indicates that the former is a lower hydrate of the latter. A guess based on volumes would indicate 9 waters of hydration.

The ESR study of the even isotope of chromium has shown that little additional information about the alums is likely to be obtained using this technique. It is impossible to distinguish between the alum type via ESR, and the inability to observe the hyperfine structure precludes the study of any finer effects. For this reason, enriching the alums with Cr(53) and studying them via the ENDOR technique was necessary. This part of the work has been most fruitful and results obtained by the ENDOR technique are now discussed.

B Nuclear Zeeman Interaction

The nuclear Zeeman interaction was found to be isotropic, that is, $g'_{n\parallel} = g'_{n\perp}$. The interaction caused a splitting of about 0.5 MHz and 1.0 MHz in the two alums at low and high field ESR lines, respectively. Such a large effect is readily measured by ENDOR. Any anisotropy greater than say 0.01 MHz in the nuclear Zeeman interaction would readily have been detected. This is evident from consideration of the effect of the other hyperfine interactions in Figures 6.4 and 6.12. It may be seen there that the nuclear Zeeman effect is not masked by any other interaction. For example, the effect at low field is approximately one half that at high field since the magnetic fields for the two ESR sets of transitions are also related in this way. It is also noted that the effect is opposite for the low and high field ESR lines. In the Rb alums the nuclear Zeeman effect tends to diverge the hyperfine energy levels in the low field ESR line and converge the levels in the high field ESR line. The reverse is true for the Cs alum. This opposite action on the two sets of hyperfine levels for a given crystal has resulted in a fairly accurate determination of the effective nuclear g value. The reason for this is that a deviation from the best g'_n value in the spin Hamiltonian will produce a constant positive difference between the calculated and measured ENDOR frequencies for one set of hyperfine levels and a constant negative difference for the other set. Also the difference for the high field set will be twice the magnitude of the difference for the low field set.

The effective nuclear g value is constant to within experimental error for

the two Rb and Cs alums; its value is $g'_n = -0.3111 \pm 0.0005$. If one assumes that this is the true nuclear g value, one obtains for the magnetic moment of Cr(53) a value of -0.4666 ± 0.0005 nuclear magnetons (nm). The handbook value of -0.4735 nm was obtained by NMR of Cr(53) in solution.⁴² Ramsey⁴³ has obtained a value of -0.4743 nm by the atomic beam method. The difference between the measured value in this work and above measurements is outside experimental error. ENDOR measurements on Cr(53) by Woonton and Dyer¹⁷ and Terhune et al¹⁵ have obtained magnetic moments that are essentially in agreement with the handbook value. Using equation (3.6) to account for paramagnetic shielding leads to a value of -0.4642 nm. This correction leads to an increase in the difference from other values, the increase, however, is small. The constancy of g'_n in the Rb and Cs alums leads one to consider some sort of constant experimental error in the g'_n value or alternately conclude that g'_n as measured, is correct.

With regard to a constant error it is very difficult to postulate a reasonable explanation. If the measured g'_n value is taken as correct, on the other hand, one must conclude that the chromium (53) nucleus sees a reduced magnetic field in the alums. In attempting to reconcile the difference between this work and the ENDOR studies of Woonton and Dyer¹⁷ and Terhune et al¹⁵ it should be noted that their measurements were made at essentially a constant magnetic field value whereas in this work ENDOR transitions in fields differing by about 2000 gauss have been fitted. It is quite possible that in fitting ENDOR transitions at one field value more freedom in the g'_n parameter is obtained than was found in this work.

It is possible to obtain the published value of g_n by sacrificing

the quality of the fit between measured and calculated ENDOR frequencies. If this is done the agreement is $\pm .020$ MHz instead of $\pm .005$ MHz or better; such a change though, expeditious, seems unwarranted. It is this worker's opinion that the measured g'_n value in the Rb and Cs alums is correct; however, it must be admitted that the difference from published values is essentially unexplained. It is also felt that the disparity in the measured and reported nuclear magnetic moment of chromium (53) does not reflect unfavorably on the determination of the hyperfine parameters A, B and Q' since these pertain to field independent interactions in the spin Hamiltonian.

C The Nuclear Quadrupole and Crystal Field Interactions

The nuclear quadrupole moment of Chromium (53) has been calculated using the relationship between the nuclear quadrupole (Q') and crystal field (D) interactions for the chromium ion in the alums. The former is proportional to the electric field gradient at the nucleus, and this at least in part is produced by the distortion from cubic symmetry of the ligand electrons. The latter is a measure of the axial component of the ligand crystal field hence its magnitude is expected to be proportional to the electric field gradient at the center of the octahedral sites. O'Reilly and Tsang⁴⁴ give the relation between the trigonal component of the crystal field and the electric field gradient in the alums to be

$$D = \frac{3}{7} \left(\frac{\lambda}{\Delta E} \right)^2 \langle r^2 \rangle V_{zz} \quad (7.1)$$

where λ is the spin-orbit coupling parameter of the chromium ion and ΔE is the splitting between the ground state singlet and the nearest triplet of the F state chromium ion, by the cubic component of the crystal field. This relation can in principle be used to calculate the quadrupole moment of chromium (53) in the Rb and Cs alums from the measured D and Q' values at 4.2⁰K. In order to do this values of λ , ΔE and $\langle r^2 \rangle$ at this temperature are required. When one attempts to calculate the quadrupole moment of chromium (53) via equation (7.1) using room temperature values of λ

and ΔE^* and $\langle r^2 \rangle$ one obtains for the Rb(H₂O) and Cs(H₂O) alums

$$Q(\text{Rb}) = -.0047 \quad \text{barns}$$

$$Q(\text{Cs}) = -.0361 \quad \text{barns}$$

Since the quadrupole moment is a property of the nucleus the two values should agree. The value obtained for the Cs alum compares well with -.03 barn obtained by Terhune et al¹⁵ which to date is the only available experimental value for the quadrupole moment of chromium (53). It is to be noted that the above values differ by a factor of about 10 which is also the difference between the quadrupole splittings in the two alums. The conclusion is drawn that the correct value of V_{zz} was not obtained for the Rb alum using equation (7.1). This fact is not surprising considering that there is a large change in the D parameter between room temperature and 4.2⁰K and that the room temperature value of ΔE was used in the calculation. It is also significant that the correct value was obtained in the Cs alum where the D value changes little from room temperature to 4.2⁰K. In order to circumvent this problem and obtain a common value for Q in the two alums it is necessary to attempt to extrapolate the measured values of Q' at 4.2⁰K to room temperature. The reasoning which leads to the room temperature values is now outlined.

* The measurements of ΔE on Rb and Cs alums grown in this laboratory were made by B. Kiggins and are part of an unpublished report on absorption spectroscopy in Rb and Cs alums.

Segleken and Torrey⁴⁵ have measured by nuclear magnetic resonance (NMR) the ratio of the quadrupolar splitting of Al(27) in the NH_4Al and KAl alums at room temperature to be $1.12 \pm .03$. Bagguley and Griffiths⁷ obtain by ESR a ratio of $1.12 \pm .07$ for the ground state splitting in the corresponding chrome alums. It therefore appears that, at room temperature the relation

$$\frac{Q'(K)}{Q'(\text{NH}_4)} = \frac{D(K)}{D(\text{NH}_4)} = 1.12 \pm .07 \quad (7.2)$$

is valid for these salts. In the present work $D(\text{Rb})/D(\text{Cs}) = -1.18 \pm .05$ at room temperature. In analogy to the result obtained for the K and NH_4 alums it is thought that the relation

$$D(\text{Rb})/D(\text{Cs}) = Q'(\text{Rb})/Q'(\text{Cs}) \quad (7.3)$$

is also valid at this temperature. The quadrupolar splitting of Cr(53) was measured, however, at 4.2°K . At this temperature the equality (7.3) does not hold. Anomalous ESR results for the K and the NH_4 chrome alums at low temperature have been repeated by Bleaney⁸. Baker⁹ showed that at 160°K the trigonal component of the crystal field of the chromic methylamine alum changed to rhombic symmetry. In this work it is noted that the ratio of the D parameters in the Rb and Cs alums is close to unity at room temperature and 4.2°K whereas the ratio of the quadrupolar splittings is about 10 at 4.2°K , also the zero field splitting in the Rb alums changes by about 40% as the temperature is lowered to 4.2°K ; the corresponding change in the Cs alum being about 8%. In view of these facts it is concluded that considerably more of a change in the crystal field at the chromium is taking place in the Rb than the Cs alum as the temperature is lowered. A consequence of this fact

would be that the equality in eq. (7.3) does not hold at 4.2⁰K. The assumption being made that it does hold at room temperature is all the more reasonable considering that $D(R)/D(Cs) \approx D(K)/D(NH_4) = 1.12$.

In order to proceed with the calculation of Q' at room temperature it is necessary to postulate that D changes linearly with Q' in the two alums over the temperature range 4.2⁰K to 298⁰K (room temperature) and that the proportionality constant is the same for both. Burns⁴⁶ has shown this to be true in $C(NH_2)_3Al(SO_4)_2 \cdot 6H_2O$ and $C(NH_2)_3Ga(SeO_4)_2 \cdot 6H_2O$ down to 77⁰K. He obtained the D parameter from ESR of Cr³⁺ substituting for Al³⁺ and Ga³⁺ and the Q' parameter via NMR of Al(27) and Ga(71). The D versus Q' curve in each case is a straight line of equal slope. Burns⁴⁷ also reports on the linear relation between Q' and temperature for the K and NH₄ alums.

Using equation (7.3) and the above postulate the quadrupole interaction of Chromium (53) in the Rb and Cs alums at room temperature has been calculated from the measured D and Q' parameters at 4.2⁰K and the D parameters at room temperature. Thus calculated values are shown in Table 7.1 along with the measured values at 4.2⁰K (which are presented for comparison purposes). Equation (7.1) with $\lambda = 87 \text{ cm}^{-1}$ ⁴⁸, $\langle r^2 \rangle = 1.447 \text{ a.u.}$ ⁴⁹ $\Delta E = 17800 \text{ cm}^{-1}$ and 17700 cm^{-1} for the Rb and Cs alums respectively and the measured D values at room temperature was solved to calculate the electric field gradient for each entry in Table 7.1. Thus calculated values of V_{zz} and the room temperature values of Q' were used in eq. (7.4) to calculate the quadrupole moments of Cr(53) in the four alum crystals.

These values also appear in Table 7.1.

$$Q' = \frac{3 V_{zz} eQ}{4I(2I-1)} (1 - \gamma_{\infty}) \quad (7.4)$$

where Q' is the nuclear quadrupole interaction constant
 eQ is the nuclear quadrupole moment of chromium (53)
 $(1-\gamma_{\infty})$ is the Sternheimer antishielding factor (10.8 for Cr^{3+})

Table 7.1 Nuclear quadrupole interactions, electric field gradients and nuclear quadrupole moment of Cr(53) in Rb and Cs alums

	$Q' \text{ (cm}^{-1}\text{)} \times 10^{-4}$		V_{zz}	Q
	4.2°K	298°K	MHz/barn	barn
Rb(H_2O)	$-0.0164 \pm .0001$	- 0.229	+ 6.247	- 0.0408
Rb(D_2O)	$-0.0165 \pm .0001$	- 0.214	+ 6.280	- 0.0379
Cs(H_2O)	$+ 0.1547 \pm .0001$	+ 0.194	- 5.231	- 0.0413
Cs(D_2O)	$+ 0.1544 \pm .0001$	+ 0.186	- 5.384	- 0.0384

V_{zz} and Q for deuterated alums was calculated on basis of ΔE measured in the hydrated alums

These values also appear in Table 7.1.

$$Q' = \frac{3 V_{zz} eQ}{4I(2I-1)} (1 - \gamma_{\infty}) \quad (7.4)$$

where Q' is the nuclear quadrupole interaction constant

eQ is the nuclear quadrupole moment of chromium (53)

$(1-\gamma_{\infty})$ is the Sternheimer antishielding factor (10.8 for Cr^{3+})

Table 7.1 Nuclear quadrupole interactions, electric field gradients and nuclear quadrupole moment of Cr(53) in Rb and Cs alums

	$Q' \text{ (cm}^{-1}\text{)} \times 10^{-4}$		V_{zz}	Q
	4.2°K	298°K	MHz/barn	barn
Rb(H ₂ O)	-0.0164 ± .0001	- 0.229	+ 6.247	- 0.0408
Rb(D ₂ O)	-0.0165 ± .0001	- 0.214	+ 6.280	- 0.0379
Cs(H ₂ O)	+ 0.1547 ± .0001	+ 0.194	- 5.231	- 0.0413
Cs(D ₂ O)	+ 0.1544 ± .0001	+ 0.186	- 5.384	- 0.0384

V_{zz} and Q for deuterated alums was calculated on basis of ΔE measured in the hydrated alums

It is seen that the extrapolation of measured Q' values at 4.2°K to those at room temperature by the method outlined above has resulted in essentially a single value for the quadrupole moment of $\text{Cr}(53)$. Also, this value is in close agreement to $-.03$ barns obtained by Terhune et al.¹⁵ The difference may in part be explained by the fact that $\langle r^2 \rangle$ value used was for a free ion, and that the λ value is only slightly reduced from its free ion value of 91 cm^{-1} . The calculated values of Q would decrease toward $-.03$ barns if a reduced value of $\langle r^2 \rangle$ were used. However, the amount $\langle r^2 \rangle$ is reduced in the alums is not known. If it is 25% then a value of $-.03$ barns would be obtained.

Lawrence and Lambe⁵⁰ have criticized the value of $-.03$ barns obtained by Terhune et al.¹⁵ Also they say that even the negative sign of the quadrupole moment may be wrong since Terhune et al.¹⁵ have obtained the sign on basis of Bersohn's⁵¹ calculations of V_{zz} in Al_2O_3 . In our work the sign has been established to be negative by measurement. As far as is known to the author this is the first measurement of the sign of quadrupole moment of $\text{Cr}(53)$.^{*} With regards to the magnitude of $.03$ for the quadrupole moment obtained by considering V_{zz} to be the same for the Cr^{3+} and Al^{3+} ions in the aluminum oxide lattice it appears that the above calculations of Q substantiate this assumption.

The basis for the criticism by Lawrence and Lambe of the results obtained by Terhune et al.¹⁵ is their comparison of the behaviour of the isoelectronic series V^{2+} , Cr^{3+} , Mn^{4+} and NMR determination of $\text{Al}(27)$ quadrupole moment in Al_2O_3 . They observe that the hyperfine field of the three paramagnetic ions is about 200 kg and is constant to about 2%. In analogy to this observation they also conclude that after accounting for the antishielding of the electric field gradient these four ions

* See post oral discussion p. 181.

should see the same V_{zz} in the aluminum oxide lattice. The values of V_{zz} for $^{51}\text{V}^{2+}$, $^{53}\text{Cr}^{3+}$, $^{55}\text{Mn}^{4+}$ and $^{27}\text{Al}^{3+}$ are - 0.1, 2.7, 0.5 and 4.4 MHz/b respectively. It is seen that the large disparity between V^{2+} and Cr^{3+} does not exist between Cr^{3+} and Al^{3+} . It seems that the isoelectronic nature of the ions is not the only consideration but that also the charge of the ion must be considered. Also a small change in the quantity $(1 - \gamma_{\infty})$ for the Cr^{3+} or the Al^{3+} can bring the V_{zz} values for the two ions into relatively close agreement. In view of these considerations it is very likely that the assumption made by Terhune et al that V_{zz} is the same for both chromium and aluminum ions in the aluminum oxide lattice is justified.

Having in this way obtained agreement for the quadrupole moment of $\text{Cr}(53)$ in the various alums and in effect lent strong support for the only previously available value of the quadrupole moment it is tempting to go back to eq. (7.1) and use it to infer why the incorrect value of Q was calculated in Rb alum at 4.2°K . One explanation that immediately comes to mind is that in the Cs alum where there is a small change in D from 298°K to 4.2°K , the correct V_{zz} value was calculated because of the correspondingly small change in ΔE , λ and $\langle r^2 \rangle$, with the first of these expected to be of relatively largest significance. In the Rb alum, on the other hand, the change in D is large over the same temperature range and a corresponding change in ΔE would preclude a correct calculation of V_{zz} and hence the quadrupole moment. It seems quite possible that in the Rb alum, as the temperature is lowered, the cubic component of the crystal field is increased considerably more than in the Cs alum. This is

consistent with the observation that the trigonal component D decreases as the temperature is lowered. This prediction is amenable to direct experimental verification. An increase in the ΔE value should be related to an increase in the spin-lattice relaxation time⁵² hence linewidths in the Rb alum should decrease more than in the Cs alum as temperature is lowered to 4.2°K. No spin-lattice relaxation time measurements in this work have been made. However peak-to-peak linewidths on the z axis have been made. Comparison of the linewidths for the hydrated alums shows that in general agreement with above consideration the linewidths in Rb alum at 4.2°K are about one half of the value at room temperature. For the Cs alum no change in linewidth is observed to within experimental error. In the deuterated alums no clear change in linewidths is noted over this temperature range. This is interpreted as being probably due to random crystal fields in the deuterated alums which inhomogeneously broaden the absorption lines beyond linewidths expected on basis of spin lattice relaxation time alone.

D. Hyperfine Interaction

The first unambiguous observation of the hyperfine structure of Cr(53) was that of Bleaney and Bowers¹⁰. They studied a mixed crystal of $\text{KCr}(\text{SeO}_4)_2 \cdot 12\text{D}_2\text{O}$ alum diluted with the corresponding aluminum alum. The chromium (53) isotope was enriched to about 97%. The observed hyperfine structure was sufficiently resolved to determine the nuclear spin of Cr(53) as 3/2. The hyperfine structure was not sufficiently resolved to detect any anisotropy and the hyperfine term in the spin Hamiltonian was simply written as $A\vec{I} \cdot \vec{S}$. The hyperfine parameter was found to be $A = 18 \pm 1 \times 10^{-4} \text{ cm}^{-1}$. Increased resolution in the ESR studies of hyperfine structure of Cr(53) was obtained by Manenkov and Prokhorov⁵³ in Al_2O_3 doped with Cr(53). The hyperfine structure was isotropic with $A = 17.5 \pm 0.5 \times 10^{-4} \text{ cm}^{-1}$. In the ENDOR work of Terhune et al¹⁵ on Cr(53) in Al_2O_3 , where the hyperfine interaction was measured with much greater precision than possible by ESR, best fit of experimental data was obtained with $A = B = 16.17 \pm 0.02 \times 10^{-4} \text{ cm}^{-1}$. Lawrence and Lambe⁵⁰ in their work on V^{2+} and Mn^{4+} in Al_2O_3 , where they found the hyperfine structure to be anisotropic, point out that Cr(53) in the same lattice is probably also anisotropic considering that the three ions form an isoelectronic series.

McGarvey⁵² has studied the ESR of Cr^{3+} in single crystals of Cobalt acetylacetonate ($\text{Co}(\text{C}_5\text{H}_7\text{O}_2)_3$) and aluminum acetylacetonate ($\text{Al}(\text{C}_5\text{H}_7\text{O}_2)_3$) and observed anisotropic hyperfine structure. The result obtained was $A = 16.2 \pm .1 \times 10^{-4} \text{ cm}^{-1}$ and $B = 16.9 \pm .1 \times 10^{-4} \text{ cm}^{-1}$. In these crystals Cr^{3+} substituting for Co^{3+} and Al^{3+} is surrounded by six oxygen ions in

near octahedral coordination. Using molecular orbital theory he has related a geometrical parameter "a" to the parameters A and B in the spin Hamiltonian,

$$A = p \left\{ \frac{4}{21} [2 - 3 a^2] - K \right\}$$

$$B = p \left\{ -\frac{2}{21} [2 - 3 a^2] - K \right\}$$

where $p = 2.0023 g_n \beta_n \beta \langle 1/r^3 \rangle_{av.} = -39.7 \times 10^{-4} \text{ cm}^{-1}$ ⁵⁵

K is the isotropic term resulting from the contact interaction and $a^2 = 2/3$, if the oxygen ions are arranged in octahedral symmetry. On this model the oxygens about the chromium ion are distorted from an octahedral configuration by compression along the trigonal axis if $a^2 < 2/3$. Molecular orbital calculations⁵⁶ for the D parameter show that the condition $a^2 < 2/3$ implies a negative value for the trigonal component of the crystal field. Piper and Carling⁵⁷ in their study of the optical spectrum of chromium acetylacetonate have also assumed a trigonal compression of the oxygens about the chromium to explain the observed sign of the trigonal component of the crystal field. The measurements of the parameters D, A and B and their relative magnitudes and their signs are in complete agreement with the above model. For the Cs alums the following was obtained: $A < B$, $a^2 < 2/3$, $D < 0$, whereas for the Rb alum, $A > B$, $a^2 > 2/3$, $D > 0$ applies. It is therefore concluded that the waters about the chromium ion in the Cs alum are compressed along the trigonal axis (the Z axis for the paramagnetic complex) from the octahedral arrangement and in the Rb alum the waters are extended along the trigonal axis from the octahedral arrangement. It is tempting at this stage to associate this compression or extension

with the type of the alum. Since the Cs alum is a β type and the Rb alum is an α type one might conclude that it may generally apply that β type alums have a compressional trigonal distortion of the water molecules around the chromium ion while in the α type alums the water molecules are extended trigonally. Since the Rb and Cs alums are the only members of this large family of salts that have been studied by ENDOR it is impossible to say whether above considerations are generally valid.

McGarvey⁵⁴ has explained the observed hyperfine anisotropy of Cr^{3+} as the basis of a trigonal compression of the oxygen atoms about the ion. His measurements of A and B parameters lead to $a^2 = 0.65$, and he has estimated that an angle of 55.3° between the trigonal axis and the chromium oxygen bond would lead to this value. For octahedral symmetry this angle is 54.7° . Thus a change in this angle of about $1/2$ degree would account for anisotropy in the hyperfine structure. The measured values of the A and B parameters in this work lead to $a^2 = 0.658$ and $a^2 = 669$ for the Cs and Rb alums respectively. In so far as the above model applies to the alums, it seems that distortion from octahedral symmetry is less in the alums than in a chromium acetylacetonate complex.

It is interesting to compare the isotropic part of the hyperfine interaction of chromium in coordination with oxygen atoms and water molecules. In case of anisotropic interaction the isotropic part is given by $1/3 (A + 2B)$. The comparison is made in Table 7.2 where the first four entries are from this work.

Table 7.2 Comparison of the isotropic part of the hyperfine interaction of $^{53}\text{Cr}^{3+}$ in two environments.

Crystal	nearest neighbours to chromium	isotropic hyperfine interaction $\times 10^4 \text{cm}^{-1}$
$\text{RbGa}(\text{SO}_4)_2 \cdot 12\text{H}_2\text{O}$	water molecules	17.330 ± 0.001 (ENDOR)
$\text{RbGa}(\text{SO}_4)_2 \cdot 12\text{D}_2\text{O}$	heavy water mol.	17.335 ± 0.001 "
$\text{CsGa}(\text{SO}_4)_2 \cdot 12\text{H}_2\text{O}$	water molecules	17.399 ± 0.001 "
$\text{CsGa}(\text{SO}_4)_2 \cdot 12\text{D}_2\text{O}$	heavy water mol.	17.414 ± 0.001 "
$\text{K}(\text{CrAl})(\text{SeO}_4)_2 \cdot 12\text{D}_2\text{O}$	heavy water mol.	18 ± 1 (ESR) ¹⁰
$\text{KAl}(\text{SO}_4)_2 \cdot 12\text{H}_2\text{O}$	water molecules	16.0 ± 0.5 " 58
$\text{AlCl}_3 \cdot 6\text{H}_2\text{O}$	water molecules	17.0 ± 0.1 " 59
$\text{AlCl}_3 \cdot 6\text{D}_2\text{O}$	heavy water mol.	17.2 ± 0.1 " 59
$\text{Co}(\text{C}_5\text{H}_7\text{O}_2)_3$	oxygen	16.7 ± 0.1 " 54
Al_2O_3	oxygen	17.5 ± 0.5 " 53
Al_2O_3	oxygen	16.17 ± 0.02 (ENDOR) ¹⁵
MgO	oxygen	16.4540 ± 0.0002 " 17
CaO	oxygen	17.0 ± 0.1 (ESR) ⁶⁰

It appears that the hyperfine interaction of Cr(53) is stronger when the chromium ion is in water coordination than where it is in coordination with oxygen atoms. Two entries in the Table, however, need to be commented on, in order to establish this unambiguously. In the first entry for Al_2O_3 the experimental error can just bring the hyperfine interaction below all values for water coordination except one. It is felt that this work should probably have a larger experimental error assigned to it since the chromium spectrum obtained is only slightly resolved. With regard to the result for KAl alum it is also felt that the experimental error quoted is too optimistic. Cr(53) spectrum was barely observable because of the large linewidth of the even isotope. With these reservations in mind it is concluded that the larger hyperfine interaction of chromium in water coordination than in oxygen coordination is generally valid. This conclusion is in agreement with results obtained for Mn^{2+} hyperfine interaction. For this ion it has been observed by Kiggins and Manoogian⁶¹ that the hyperfine parameter A is larger when the Mn^{2+} ion is in water coordination than when it is in oxygen coordination. These workers have also found that the A parameter for Mn^{2+} surrounded by four water molecules and two oxygens is between values reported for water and oxygen coordination. A conclusion that can be made for the chromium ion is that in water coordination the stronger hyperfine interaction implies less covalency in bonding to the water molecules than there is in bonding to the oxygen ions.

E. Post Oral Discussion

In the oral discussion of the thesis it was pointed out that Artman and Murphy⁶² estimate the quadrupole moment of chromium (53) to be positive and between 0.02 and 0,05 barn. . This is in contrast to the previously proposed value of - 0.03 barn reported by Terhune et al¹⁵ and the value of - 0.039 barn reported in this study. The purpose of this note is to state the reasoning and assumptions used by Artman and Murphy in making their estimate.

These workers have noted that the ionic radii of chromium and aluminum differ (0.63 A and 0.51 A respectively). They have postulated that when the former substitutes for the latter in the corundum lattice the immediate neighbourhood is slightly distorted. Assuming a distortion of the six oxygens about the chromium impurity they have calculated using the method of lattice sums the electrostatic potential and the electric field gradient at the chromium site. Their calculation produces a negative electric field gradient at the chromium site. From this calculation and the measured negative quadrupolar interaction in Al_2O_3 ¹⁵ they conclude that the quadrupole moment of chromium (53) is positive. The authors go on to say that the assumption of negative electric field gradient for Cr^{3+} substituting for Al^{3+} (the Al^{3+} ion sees a positive electric field gradient in the corundum lattice) is in agreement with most, but not all, optical absorption data in $Al_2O_3(Cr^{3+})$.

The estimate by Artman and Murphy that the electric field gradient about Cr^{3+} in Al_2O_3 is negative is considered doubtful for the following

two reasons. Firstly, McClure⁶³ has obtained good agreement with experimental values of $10Dq$ and the trigonal field parameter v by translating the Cr^{3+} ion about 0.1 Å along the c axis in Al_2O_3 lattice. Also on this model the electric field gradient at the Cr^{3+} site is positive. McClure's model however does not agree as well as that of Artman and Murphy with experimental parameters τ and β (Artman and Murphy notation). The former measures the enhancement of the aluminum quadrupolar interaction due to nearest chromium ion and the latter refers to an angle relating the electric effect tensor R to the paramagnetic resonance spin Hamiltonian. Secondly, Artman and Murphy point out themselves that X-ray studies of Cr^{3+} position in highly doped ruby (4% chromium) indicate that the chromium site is shifted 0.06 Å in the opposite sense to the model used by the authors. They state that the relation of these X-ray results to the conclusions of their paper is not clear.

In attempting to relate the value of -0.039 barn obtained for the quadrupole moment of $Cr(53)$ in this study to the value of $+0.02$ to $+0.05$ barn proposed by Artman and Murphy the following may be noted. First, the magnitudes are in good agreement considering the relative weakness of the quadrupolar interaction. Additional support for this order of magnitude comes from NMR measurements of the quadrupolar interaction of $Cr(53)$ in powdered Cr_2O_3 made by Rubinstein *et al.*⁶⁴ From the quadrupolar interaction of $\pm 0.525 \pm 0.020$ MHz these workers deduce the quadrupole moment to be ± 0.022 barn. In the absolute sense the magnitude of 0.039 barn

obtained in this study is believed to be more accurate than the value of 0.022 barn because the accuracy of the measurement of the quadrupolar interaction in this work is ± 0.001 MHz whereas Rubinstein *et al*⁶⁴ quote ± 0.020 MHz. With regard to the upper limit of 0.05 barn postulated by Artman and Murphy this is an estimate meant to account for effects of covalent bonding on the electric field gradient. As far as the sign of the quadrupole moment of Cr(53) is concerned, it is to be noted that in the alums investigated in this study chromium substitutes for gallium (ionic radii are 0.63 Å and 0.62 Å respectively). Therefore, any distortion such as postulated by Artman and Murphy in the Al_2O_3 lattice should be negligible in the alum lattice. Consequently, the electric field gradient seen by Cr^{3+} and Ga^{3+} in the alums should be the same. In so far as the relation between the D parameter and the electric field gradient as given in eq. (7.1) is valid, one can conclude that the sign of the electric field gradient follows from the sign of the D parameter. From the experimentally determined sign of D and Q' parameters and the relation (7.1) the sign of the quadrupole moment of Cr(53) has been determined to be negative. It is in this sense that the negative sign has been "measured".

It has also been pointed out in the oral discussion of the thesis that errors can result in numerically computed eigenvalues obtained by computer diagonalization. It can readily be demonstrated that such errors are negligible in this work. This is accomplished by noting that the off-diagonal elements in the 16 X 16 matrix for Cr(53) (see Tables 3.2 and 3.3), are almost three orders of magnitude smaller than the diagonal

elements. In such a case second order equations 3.16 and 3.17 should reasonably well describe the ENDOR spectrum. This is seen to be the case from the following comparison of frequencies in MHz.

	measured	second order	computer diagonalization
ν_1	76.9799	76.9650(- 0.0031)	76.9794 (- 0.0005)
ν_2	77.2974	77.3006(+ 0.0032)	77.2999 (+ 0.0025)
ν_3	77.2920	77.2950(+ 0.0030)	77.2919 (- 0.0001)
ν_4	77.6161	77.6305(+ 0.0144)	77.6124 (- 0.0037)

The data presented pertains to the $\text{Rb}(\text{H}_2\text{O})\text{alum}$ when the magnetic field is along the Z axis and the M_s multiplet in question is $-3/2$. The numbers in parenthesis are deviations from the measured ENDOR frequencies. It can be seen that computer diagonalization does not introduce errors but on the contrary leads to a better fit. The above comparison shows that higher than second order corrections have profitably been applied by using computer diagonalization.

APPENDIX

LIST OF REFERENCES

1. Lipson, H., Beavers, C.A., Proc. Roy. Soc. (Lond.) A14B, 664 (1935)
2. Lipson, H., Proc. Roy. Soc. (Lond.), A15, 347 (1935)
3. Ledsham, A.H.C., Steeple, H., Acta. Cryst., B24, 1287 (1968)
4. Manoogian, A., MacKinnon, J.A., Can. J. Phys., 45, 2769 (1967)
5. Weiss, P.R., Whitmer, C.A., Torey, H.C., Jean-Sen Hsiang, Phys. Rev. 72, 975 (1947)
6. Whitmer, C.A., Weidner, R.T., Weiss, P.R., Phys. Rev. 73, 1468 (1948)
7. Bagguley, D.M.S., Griffiths, J.H.I., Proc. Roy. Soc. (Lond.), A204, 188 (1950)
8. Bleaney, B., Proc. Roy. Soc. (Lond.) A204, 203 (1950)
9. Baker, J.M., Proc. Phys. Soc. (Lond.) B69, 633 (1956)
10. Bleaney, B., Bowers, K.D., Ingram, D.J.E., Proc. Phys. Soc. A64, 758 (1951)
11. Bleaney, B., Bowers, K.D., Proc. Phys. Soc. A65, 1135 (1951)
12. Feher, G., Phys. Rev. 103, 500 (1956)
13. Feher, G., Gere, E.A., Phys. Rev. 103, 834 (1956)
14. Terhune, R.W., Lambe, J., Makhov., Cross, L.G., Phys. Rev. Letters, 4, 234 (1960)
15. Terhune, R.W., Lambe, J., Kikuchi, C., Baker, J., Phys. Rev., 123, 1265 (1961)
16. Lawrence, N., Lambe, J., Phys. Rev. 132, 1026 (1953)

17. Woonton, G.A., Dyer, G.L., Can. Jour. Phys. 45, 2265 (1967)
18. McGarvey, B.R., Jour. Chem. Phys. 40, 809 (1964)
19. Larson, A.C., Cromer, D.T., Acta. Crystallogr. 22, 793 (1967)
20. Cromer, D.T., Kay, M.I., Larson, A.C., Acta Crystallogr., 21, 383 (1966)
21. Cromer, D.T., Kay, M.I., Larson, A.C., Acta. Crystallogr., 22, 182 (1967)
22. Wykoff, R.W.G., Crystal structures (Interscience, New York), (1960)
23. Ayscough, P.B., Electron Spin Resonance in Chemistry, p. 31, (Methuen and Co., London) (1967)
24. Bethe, H., Ann. Physik 3, 133 (1929)
25. Wigner, E., Nachr. Akad. Wiss. Gottingen, Math-Physik Kl.II a, 546 (1932)
26. Van Vleck, J.H., J. Chem. Phys., 7, 61 (1939)
27. Abragam, A., Bleaney, B., Electron Paramagnetic Resonance of Transition Metal Ions, p. 690, (Oxford University Press) (1970).
28. Watson, R.E., Freeman, A.J., Hyperfine Interactions p. 53, (Academic Press N. Y. (1967)
29. Moser, C.M., Hyperfine Interactions, p. 95, (Academic Press N.Y.) (1967)
30. Baker, J.M., Bleaney, B., Proc. Roy. Soc. A245, 156 (1958)
31. Geschwind, S., Hyperfine Interactions, p. 225, (Academic Press N.Y.) (1967)
32. Pryce, M.H.L., Proc. Roy. Soc., A63, 25 (1950)
33. Abragam, A., Pryce, M.H.L., Proc. Roy. Soc., (Lond.), A205, 135 (1951)

34. Reference 27 p. 166
35. Varian Workshop Lectures, Varian Associates, Analytical Instrument Division, Palo Alto, Calif.
36. Van Vleck, J.H., Phys. Rev., 57, 426 (1940)
37. Llewellyn, P.M., Whittlestone, P.E., Williams, J.M., J. Sci. Instr., 39, 586 (1962)
38. Brown, G., Mason, D.R., Thorp, J.A., J. Sci. Instr. 42, 648 (1965)
39. Buckmaster, H.A., Dering, J.C., J. Sci. Instr., 43, 404 (1966)
40. Buckmaster, H.A., Dering, J.C., Can. J. Phys., 45, 107 (1967)
41. Slichter, C.P., Phys. Rev., 99, 479 (1955)
42. Jeffries, C.D., Sogo, P.B., Phys. Rev., 91, 1286 (1953)
43. Ramsey, N.F., (Molecular Beams, Oxford) (1956)
44. O'Reilly, D.E., Tsang, Tung, Phys. Rev. 157, 417 (1967)
45. Segleken, W.G., Torrey, H.C., Phys. Rev. 98, 1537 (1955)
46. Burns, G., Phys. Rev. 123, 1634 (1961)
47. Burns, G., J. Chem. Phys., 32, 1585 (1960)
48. Gordy, W., Microwave spectroscopy (John Wiley, N.Y.) (1953) p. 230.
49. Reference 27 p. 399
50. Lawrence, N., Lambe, J., Phys. Rev. 132, 1029 (1963)
51. Bersohn, R., J. Chem. Phys. 29, 326 (1958)
52. Reference 23 , p. 119
53. Manenkov, A.A., Prokhorov, A.M., Soviet Phys. JETP, 4, 288 (1957)
54. McGarvey, B.R., J. Chem. Phys., 40, 809 (1964)

55. McGarvey, B.R., J. Phys. Chem., 71, 51 (1967)
56. McGarvey, B.R., J. Phys. Chem., 41, 3743 (1964)
57. Piper, T.S., Carling, R.L., J. Chem. Phys., 36, 3330 (1962)
58. Bendt, P.J. Phys. Rev., 2, 4366 (1970)
59. Wong, E. I., J. Chem. Phys., 32, 598 (1960)
60. Low, W., Rubins, R.J., Phys. Let. (Neth) 1, 316 (1962)
61. Kiggins, B., Manoogian A., ESR of Mn^{2+} impurities in Blodite.
(to be published).
62. Artman, J.O., Murphy, J.C., Phys. Rev. 135, A1622 (1964)
63. McClure, D.S., J. Chem. Phys., 36, 2757 (1962)
64. Rubinstein, M., Strauss, G.H., Krebs, J.J., Phys. Letters.,
12, 302 (1964).

VITA AUCTORIS

NAME Alexander G. Danilov

BORN Yugoslavia, 1939

EDUCATION

Primary Belgrade, Yugoslavia, 1946-1951

Secondary Bicester, England, Grammar School, 1951-1953

Bathurst, N.B., Canada, High School, 1954-1957

Universities Sir George Williams University, 1959-1963, B.Sc.

University of Ottawa, 1967-1968, M.Sc.

University of Ottawa, 1968 to present.